UAB
Universitat Autònoma de Barcelona

UAB
Universitat Autònoma
de Barcelona

Simplifying Complexity: Harnessing Coarse-Grained Models to Study Intricate Systems

by

Rosa Suarez Lopez

Ph.D. Thesis

Ph.D. program in Chemistry

Supervised by: Tutor:

Prof. Carlos Jaime   Prof. Carlos Jaime

Departament de Química

Facultat de Ciències

2023

A thesis submitted in partial fulfillment for the degree of Doctor of Phylosophy in Chemistry by:

Rosa Suarez Lopez

Checked and accepted:

Prof. Carlos Jaime

Bellaterra, July 2023

To my beloved family, especially to
Avi Pepito i Àvia Heve

Abstract

The use of Coarse-Grained (CG) models has emerged as a valuable tool in scientific research, offering distinct advantages for elucidating complex systems that are challenging to comprehend solely through experimental techniques, given their inherent limitations. Among the plethora of computational techniques available, CG models bridge the gap between all-atom and mesoscopic levels, allowing us to gain insights into larger-scale phenomena without losing essential properties.

In the present thesis, we have employed two methods, Dissipative Particle Dynamics (DPD) and the Martini force field, which implement CG models. Our research was split into three distinct studies. The initial investigation is focused on assessing the applicability of DPD for studying the synthesis of gold nanoparticles (Au NPs) using various surfactants. This proved to be a challenging task due to the inherent complexity of defining the metallic behavior within Force Fields (FF). The second investigation examines the possibility of achieving spherical Janus distributions onto Au NPs surface using two different immunoglobulins G (IgG). For this, a detailed examination of the amino acids (AAs) sequences for both IgGs was conducted. The final part of our research explores the dynamics of a specific G-quadruplex (G4) and its interaction with two different ligands using Martini Force Field.

Resum

L'ús de models Coarse-Grained (CG) ha emergit com una eina valuosa en la recerca científica, oferint diversos avantatges per l'estudi de sistemes complexos que són difícils de comprendre a través de tècniques experimentals, donades les seves limitacions. D'entre la multitud de tècniques computacionals disponibles, els models CG s'han establert com l'intermedi entre els nivells atomístics i macroscòpics, oferint una visió més clara dels fenòmens que succeeixen a gran escala sense perdre les seves propietats essencials.

En aquesta tesi, hem emprat dos mètodes, la Dinàmica de Partícules Dissipatives (DPD) i el camp de forces Martini, que ambdós implementen models CG per realitzar tres estudis. El primer, es centra en avaluar l'aplicabilitat del mètode DPD en l'estudi de la síntesis de nanopartícules d'or (Au NPs) emprant diversos tensioactius. Donada la complexitat inherent de definir el comportament metàl·lic en els camps de forces, aquesta va resultar una tasca desafiant.

El segon estudi es basa en examinar la possibilitat d'obtenir distribucions Janus esfèriques sobre la superfície de les Au NPs mitjançant dues immunoglobulines G (IgG). Per fer-ho, es va estudiar detalladament la seqüència d'aminoàcids d'ambdós IgGs.

El darrer estudi explora la dinàmica d'un G-quadruplex (G4) i la seva interacció amb dos lligands diferent substituïts utilitzant el camp de fores Martini.

Resumen

El uso de modelos coarse-grained (CG) ha surgido como una herramienta valiosa en la investigación científica, ofreciendo ventajas únicas para estudiar sistemas complejos que son difíciles de entender a través de técnicas experimentales, dadas sus limitaciones inherenes. Entre la multitud de técnicas computacionales disponibles, los modelos CG se situan como intermediarios entre los modelos atomísticos y mesoscópicos, permitiéndonos obtener una visión más detallada de los fenómenos a gran escala sin perder sus propiedades esenciales.

En esta tesis, hemos utilizado dos métodos que implementan modelos CG, la Dinámica de Partículas Disipativas (DPD) y el campo de fuerzas Martini para realizar tres estudios distintos. El primero se centra en evaluar la aplicabilidad de DPD para estudiar la síntesis de nanopartículas de oro (Au NPs) utilizando varios tensioactivos. Debido a la complejidad inherente de definir el comportamiento metálico centro de los campos de fuerza, esto resultaba un desafío.

En el segundo se examina la posibilidad de obtener distribuciones Janus esféricas sobre la superficie de las Au NPs utilizando dos tipos de inmunoglobulinas G (IgG). Para ello, se realizó un examen detallado de las secuencias de aminoácidos (AAs) para ambas IgGs.

Finalmente, en el último estudio se explora la dinámica de un G-quadruplex (G4) específico y su interacción con dos ligandos distintos utilizando el campo de fuerzas Martini.

Acronyms and "Abbreviations"

AAs   Amino acids

Ag NPs   Silver Nanoparticles

Au NPs   Gold Nanoparticles

CG   Coarse Grained

Cit.   Citrate

c.o.m.   Center of masses

CTAB   Cetyltrimethylammonium bromide

DPD   Dissipative Particle Dynamics

FF   Force Field

G4   G-quadruplex

g(r)   Radial Distribution Function

GROMACS   GROninguen Machine for Chemical Simulations

HI   Hydropathy Index

HSAB   Hard and Soft Acids and Bases

IgG   Immunoglobulin G

LJ   Lennard-Jones

LPC   Lysophosphatidylcholine

MC   Monte Carlo

MD   Molecular Dynamics

MPA   3-mercaptopropionic acid

MUA   11-mercaptoundecanoic acid

NP   Nanoparticle

Ole.   Oleylamine

PAHs   Polycyclic Aromatic Hydrocarbons

PBC   Periodic Boundary Conditions

PDB   Protein Data Bank

PG   Phosphatidylglycerol

pI   Isoelectric point

QM   Quantum Mechanics

R   Side chain

Rg   Radius of gyration

RMSD	Root Mean Square Deviation
RMSF	Root Mean Square Fluctuation
SAMs	Self-assembly Monolayers
SC	Sodium Citrate
SO	Short Overview
SRP	Soft Repulsive Parameters
TCD	Trinity College Dublin
UCG	Ultra Coarse Grained
VMD	Visual Molecular Dynamics

Table of contents

"Begin at the beginning", the King said gravely,
"and go on till you come to the end: then stop"
Lewis Carroll - Alice in Wonderland

Short Overview

This Short Overview (SO) provides an overall context of the research topic for this PhD thesis and outlines its organization.

The scientific community has always focused on complex systems as they play a crucial role in advancing new materials and designing functional devices[1]. Their fusion with biological compounds offers exceptional applications in life sciences including drug delivery, biosensing, antibacterial activity, molecular imaging and more[2,3].

Despite the availability of sophisticated experimental techniques, determining the physicochemical properties of complex systems remains challenging. Although non-invasive experimental techniques can provide valuable insights into dynamic processes, they are limited in their ability to achieve high resolutions in time, typically in the range of milliseconds or microseconds, and they can be expensive. To overcome these limitations, molecular modeling presents a promising solution since it can predict a wide range of properties and generate realistic molecular images for studying these processes. Even though computers cannot completely replace experiments, they are regarded as more cost-effective, faster, and environmentally safer[4].

Molecular modeling investigations typically involve the following main steps:

1) <u>Model Selection.</u> A model is chosen to describe the intra- and intermolecular interactions in the system. The most common include Quantum Mechanics (QM) and classical mechanics. These models allow us to determine how the energy systems varies as the positions of the atoms and molecules change. It is noteworthy to say that the choice often depends on the specific research question, the level of detail needed and the computational resources available.

2) <u>Computation.</u> Once the model is chosen, the next step is the computational process. Depending on the model and the system, this could involve energy minimization, Molecular Dynamics (MD), Monte Carlo (MC) simulations, or a conformational search.

3) <u>Analysis.</u> After computation, the results must be analyzed. This involves identifying trends and interpreting the results in the context of the original research question. This step often generates new hypotheses or provides insights into the system's behavior.

4) <u>Validation.</u> The final step typically entails comparing the predictions of the model with experimental results or other established data. If the model's predictions are in line with these results, it increases our confidence in the model. If they are not, it may indicate that the model needs to be adjusted.

There are various models available, each serving different purposes. **Figure SO1** provides a convenient and straightforward classification of computer models based on their resolutions.
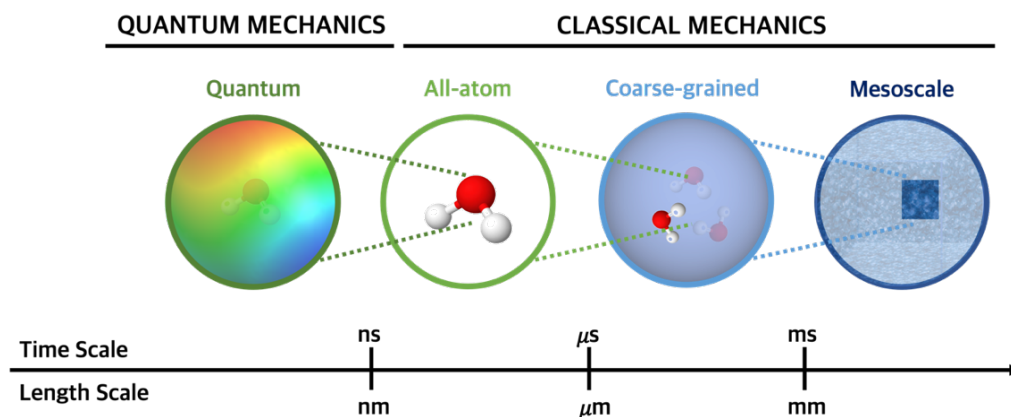
Figure SO1: Classification of computational models at different time and length scales.

As previously mentioned, the choice of a suitable model depends mainly on the research question, the complexity of the system, and the available computational resources. QM describes processes involving electrons such as bond formation and cleavage while classical mechanics employs Newton's equation of motion to describe the motion of larger systems. QM is especially effective in studying small molecules with high accuracy and capturing quantum effects. In contrast, classical mechanics provide valuable insights for studying larger systems and phenomena that do not require the level of detail offered by QM. Despite QM offers more accurate molecular descriptions, its computational cost makes them less suitable for studying complex systems. Consequently, classical mechanics can shed light on features that QM are unable to access.

In classical mechanics, each atom is represented by a single *particle* with an assigned radius, polarizability, and constant net charge, while bonds are viewed as *springs*. The set of equations governing interactions, both bonded and non-bonded, is referred to as a force field (FF), and it is used to determine the potential energy between systems. **All-atom** simulations have been used to conduct several studies in biomolecular systems however, numerous processes occurring in aqueous media exceed the capabilities of atomic-level simulations. On the other hand, **mesoscale models** offer a valuable tool for comprehending biological and interfacial systems due to their ability to manipulate materials functionalities[5] but, the intricate chemistry of a system is lost.

Given the gap in scale, typically by two or three orders of magnitude, between all-atom and mesoscopic levels, a new approach is required to bridge them. One alternative is the utilization of Coarse-Grained (CG) models, in which complex systems are simplified by grouping several atoms into a single entity referred to as a *"bead"*. This process effectively reduces the degrees of freedom, speeding up simulations[6]. Furthermore, the simplification results in a less complicated potential energy, facilitating more rapid equilibrations relative to atomistic scales. Despite the revolutionary progress of CG models in computer simulations, the development of reliable and robust CG models that can preserve the full atomistic resolution continues to be difficult.

The main challenge arising in this context is to establish a direct link to connect experimental results with computational methods. By designing CG models that mirror the structure of all compounds and detailing its interactions, simulations should ideally be able to predict the experimental results that would otherwise be difficult or expensive to be conducted.

SO.1 Thesis outline

This thesis is structured as follows. **Chapter 1** presents the overall objectives of the thesis.

Chapter 2 describes the theoretical background relevant for this work. It begins with an overview of the CG models in which the concept of *"bead"* is introduced. The properties of these *"beads"* are defined by the main computational methods employed in this work: Dissipative Particle Dynamics (DPD) –a hybrid of MD and MC algorithm- and the Martini force field. The formalism necessary to understand the foundations of such methods is also explained.

The practical application of these techniques to gold nanoparticles (Au NPs) is demonstrated in **Chapters 3, 4 and 5**. These materials have attracted special interest due to their physical and chemical properties such as their large surface area and its small size that differ from bulk materials[7]. Specifically, **Chapter 3** introduces a novel approach to define the metallic behavior. To know how accurate the metal definition is, the nucleation and growth steps of Au NPs formation using different surfactants were studied. The results are then compared with experimental studies focusing on CTAB-Gold nanorod mechanisms of growth.

Chapter 4 investigates the feasibility of obtaining Janus distributions onto Au NPs surface using two immunoglobulins G (IgG). IgG are defined using two distinct CG models: a simpler model represented by a single bead and, a more complex one depicted by four CG beads, mirroring its Y-shaped like structure. The interactions between beads are reproduced by the Soft Repulsive Parameters (SRP), which are crucial for defining the chemical nature of the system when working with DPD, using various approaches. To determine these SRP values for each bead, an in-depth examination of the amino acid (AA) sequences is conducted. **Chapter 5**, which is the continuation of **Chapter 4**, investigates the impact of pH variations on the determination of SRP values.

In **Chapter 6**, we delve into the dynamics of a G-quadruplex (G4) and its interaction with two diaromatic guanidinium-porphyrin conjugates presenting *meta-meta* and *para-para* substitutions using Martini force field. Initially, the CG models for the compounds using two methods are stablished. Notably, the CG for the G4 is based on Martini force field develop by DNA[8], while the CG for both ligands is manually built. Following this, the structural stability, and the conformation dynamics of G4 over the time is examined. Finally, the interactions between the G4 and both ligands are investigated.

Chapter 7 provides an overarching summary of the primary findings and discussions from each chapter of this thesis and suggests several plausible directions for the future research.

Finally, **Chapter 8** collects the simulation details used in each chapter.

Supplementary details are presented at the end of the thesis by several Appendixes.

SO.2 References

(1)   Ross, J.; Arkin, A. P. Complex Systems: From Chemistry to Systems Biology. *Proc. Natl. Acad. Sci.* **2009**, *106* (16), 6433–6434.

(2)   McNamara, K.; Tofail, S. A. M. Nanoparticles in Biomedical Applications. *Advances in Physics: X* **2016**, *2* (1), 54–88.

(3)   Bharathala, S.; Sharma, P. Biomedical Applications of Nanoparticles. In *Nanotechnology in Modern Animal Biotechnology: Concepts and Applications*; Maurya, P. K.; Singh, S., Eds; Elsevier, 2019, 113–132.

(4)   Gubbins, K. E.; Moore, J. D. Molecular Modeling of Matter: Impact and Prospects in Engineering. *Ind Eng Chem Res* **2010**, *49* (7), 3026–3046.

(5)   Kumar, A.; Abbott, N. L.; Kim, E.; Biebwck, H. A.; Whitesides, G. M. Patterned Self-Assembled Monolayers and Meso-Scale Phenomena. *Acc. Chem. Res.* **1995**, *28* (5), 219-226.

(6)   Ingólfsson, H. I.; Lopez, C. A.; Uusitalo, J. J.; de Jong, D. H.; Gopal, S. M.; Periole, X.; Marrink, S. J. The Power of Coarse Graining in Biomolecular Simulations. *Wiley Interdiscip. Rev. Comput. Mol. Sci.* **2014**, *4* (3), 225–248.

(7)   Bajpai, M.; Shafi, H.; Kumari, S. Nanoparticles: Importance and Need for Regulations. In *Nanoformulations in Human Health*; Talegaonkar, S.; Rai, M., Eds.; Springer: Cham, 2020, 93–107.

(8)   Uusitalo, J. J.; Ingólfsson, H. I.; Akhshi, P.; Tieleman, D. P.; Marrink, S. J. Martini Coarse-Grained Force Field: Extension to DNA. *J. Chem. Theory Comput.* **2015**, *11* (8), 3992-3945.

"Write it down. Written goals have a way to transforming wishes into wants;
cant's into cans; dreams into plans; and plans into reality.
Don't just think it − ink it!"
Michael Korda

Chapter 1

Objectives

This chapter establishes the main objectives of the present thesis, which seek to explore the application of CG models in analyzing complex systems.

As mentioned in the **SO**, remarkable advances in terms of more accuracy and efficiency of force fields and algorithms and of course the increase in computational power have been made in recent years. The use of CG models is needed to explore phenomena of complex systems at longer time and length scales that QM approaches find challenging to tackle. Thus, the main goal of this thesis is to design CG models and define the interactions between these *"CG beads"* (building blocks), with the purpose of clarifying aspects that are difficult to determine through experimental procedures.

According to the three different topics defined in the **SO**, the objectives of each study are listed below:

- OBJECTIVE 1: to implement a reliable approach for determining the SRP values for metal beads, in **Chapter 3**.

- OBJECTIVE 2: to explore the possibility of achieving spherical Janus distributions onto Au NPs surface with two IgG, using several approaches to determine the SRP values, in **Chapter 4**, and to analyze the influence of pH changes on these SRP values, in **Chapter 5**.

- OBJECTIVE 3: to build a proper CG model to study the dynamics of G4 and its interaction with two diaromatic-porphyrin conjugates, in **Chapter 6**.

"One of the principal objects of theoretical research in any department of knowledge, is to find the point of view from which the subject appears in its greatest simplicity."
J. Williard Gibbs (1881)

Chapter 2

Molecular model and simulation methods

This chapter gives a brief introduction into the theoretical concepts used in this work. Due to the broad range of aspects that are related to the topic it is not possible to cover all of them exhaustively. However, an overview of the foundations of CG, DPD and Martini force field are required.

2.1. Getting more with less

As outlined in the **SO** of this thesis, CG models are useful to reproduce macroscopic experimental properties which are considered to be the bottleneck in atomistic models. Philosophically, this corresponds to extracting the essential key results from a system to reproduce its physical behavior with less computing overhead by employing lower-resolution models. This can be achieved when matter is made up of entities known as *"CG sites or beads"*, each of which is composed of more than a single atom.

The process of grouping atoms into beads can occur across a broad range of scales; indeed, a bead can include few atoms, several functional groups or an entire protein. **Figure 2.1** draws a suitable illustration of the application of CG at different levels.

All atom	United atom	Functional groups CG	Amino Acids CG
24 Atoms	13 Beads, 5 types	7 Beads, 4 types	3 Beads, 1 type
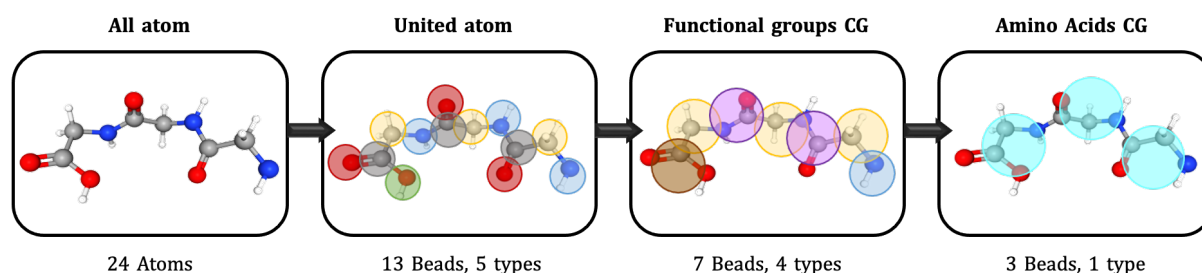
Figure 2.1: Example of triglycine showing the difference between all atom structure and different CG levels.

The level of CG adopted can significantly affect the complexity, speed, and scale of the simulation. United atom is considered an intermediate approach between all atom and CG models. In this case, heavy atoms are grouped with their bonded hydrogen atoms to create new atom types, while the others retain their original entities [1,2]. Although it considerably reduces the number of atoms that need to be simulated, it still retains a high level of detail making the simulation computationally intensive.

As the number of beads decreases, such as in functional groups CG and even further in amino acids CG (**Figure 2.1**), simulations become faster, and the systems that can be modeled become larger. As a result, researchers can gain insights into the behavior of complex systems. Some studies have taken this concept further with "*ultra coarse-grained*" (UCG), where each bead represents tens or even hundreds of heavy atoms [3].

The development of a new CG model is not without effort, as it requires proper mapping (between atoms and CG beads), definition of the interacting potentials and testing for legitimate validation. The choice of CG mapping is the first decision which must be made and is one of the most important features of the model. Although the removal of degrees of freedom can significantly speed up simulations, it is crucial to preserve enough chemical information. Therefore, the mapping requires a detailed knowledge of the system being studied. On the other hand, the parameterization of CG models to accurately represent the chemistry of the system is not straightforward. Even though, there are several methods for systematically constructing the potentials, no single method has been found to consistently produce good results for all systems.

2.1.1 Which are the benefits and limitations of using CG models?

CG models have been extensively used to develop newer and more accurate models to capture the essential details without the computational labor and cost of brute force atomistic simulations. Computationally, these models offer enticing features:

1) They can link atomistic and continuum scales. CG models bridge the gap by allowing for the simulation of larger length and time scales while still retaining some essential features of the system.

2) The number of degrees of freedom is reduced providing a considerable degree of mathematical simplicity. The strategy is to retain only the degrees of freedom important to the phenomena of interest.

3) Because the fewer degrees of freedom, the number of particles that must be computed are smaller. And thus, they exhibit an increase of computational speed up.

4) The interaction potentials are simplified and smoothed for molecules to reflect the fact that interactions between CG beads are averaged over the interactions between the individual atoms or molecules.

5) The data obtain is much easier to analyze in comparison to the detailed information from atomistic simulations.

Yet, on the other side, not all systems benefit from CG representations since they present certain limitations:

1) The oversimplification of the system causes a loss of chemical detail. So, the trade-off is that the observation of atomistic details is impossible.

2) The reduction of degrees of freedom also affects the dynamics of the system. Indeed, CG models are often faster than real dynamics which leads to a poorly replication of real dynamics.

3) Considering that CG are tailored for specific features of phenomena of interest, they present a lack of transferability with respect to other systems. That is to mean that atoms should be modelled with different parameter sets when using different environments.

4) Another subtle problem is the inability of optimized CG parameters to accurately predict thermodynamic properties such as compressibility and pressure. This is known as the "representability problem".

To retain the essential aspects of the system of interest, an effective interaction between CG beads needs to be parametrized. Briefly, there are three ways to devise such interactions in CG models: bottom-up, top-down and hybrid approaches[4]. The idea behind bottom-up approaches is the use of atomistic models to get the properties of the system and design an effective coarse-grained potential. An obvious advantage is that the information of atomistic models itself is required since the interactions at CG levels come from the collective interactions at atomistic levels. However, the macroscopic thermodynamic properties are poorly described. Contrary to bottom-up approaches, top-down take essentially the parameters from experimental data to come up with an effective coarse-grained forcefield to reproduce the macroscopic thermodynamic properties. Although this approach is not capable of capturing fine details of the interactions, it can provide potentials that are easily transferable. Finally, hybrid approaches combine the advantages of both bottom-up and top-down approaches. Ideally, bonded interactions are based on structural properties whilst non bonded interactions are modelled to replicate macroscopic phenomena.

Over the last decades, hybrid models have been demonstrated as a powerful approach to model complex systems and their interactions. However, an improvement of either bottom-up and top-down approaches is required for increasing both their accuracy and applicability range to wider, larger and complex assemblies.

In the present thesis, we have chosen Dissipative Particle Dynamics (DPD) and Martini force field methods to represent the behavior at mesoscopic level while still preserving important features of atomistic topologies and interaction. In both methods the system is simplified applying CG models to reduce the computational cost and to increase the simulation times. Additionally, they both incorporate elements of other modeling approaches to improve the accuracy and efficiency of their simulations. A detailed explanation for each method is explained in the following **sections** (**2.2** and **2.3**).

2.2. Dissipative Particle Dynamics

The origin of DPD can be identified as a paper by Hoogerbrugge and Koelman in the early 90s who presented a novel particle-based scheme for simulating the dynamics of isothermal fluids[5]. DPD is a mesoscopic method like MD in which the motion of particles is governed by Newton's equations. Different from the classical MD, two additional forces terms (dissipative and random forces) are defined in the governing equation of the total fore (F_i) acting on each bead:

$$F_{i=} \sum_{j \neq i} \left[f^C(r_{ij}) + f^D(r_{ij}, v_{ij}) + f^R(r_{ij}) \right] \qquad (2.1)$$

where f^C, f^D and f^R represent the conservative, dissipative and random forces between particles i and j, in that order. The first one determines the thermodynamics of the DPD system and is defined by a purely repulsive soft-core potential.

$$f^C(r_{ij}) = f^c(r_{ij}) \hat{r}_{ij} \qquad (2.2)$$

f^c represents the non-negative (repulsive) scalar function determining the form of conservative functions, r_{ij} is the distance between particles j and i and $\hat{r}_{ij}$ is the unit vector connecting particle j and i. Extended information will be found in **section 2.2.2**.

The f^D attemps to reduce the relative velocities of neighboring particles and represents the viscosity in the fluid. And the random force (f^R) models the influence of the atomistic degrees of freedom that have been eliminated from the description during the CG process.

$$f^D(r_{ij}, v_{ij}) = -\gamma \omega^D(r_{ij})(v_{ij} \cdot \hat{r}_{ij}) \, \hat{r}_{ij} \qquad (2.3)$$

$$f^R(r_{ij}) = \sigma \omega^R(r_{ij}) \xi_{ij} \hat{r}_{ij} \qquad (2.4)$$

Where:

- γ and σ are parameters determining the strength of dissipative and stochastic interactions.

- ω^D and ω^R are non-negative functions describing the variations of the friction coefficient and the random force with distance, respectively.

- v_{ij} is the velocity difference between particles j and i.

- ξ_{ij} is a random variable with Gaussian distribution independent for each pair of particles. The momentum conservation is obtained by enforcing $\xi_{ij}=\xi_{ji}$.

As dictated by Español and Warren, f^D and f^R must be related by the Fluctuaction-Dissipation Theorem[6] with the condition:

$$\omega^D = [\omega^R]^2 \tag{2.5}$$

ω^D and ω^R cannot be chosen independently. If Eq. (2.5) is satisfied, the equilibrium temperature is defined as:

$$k_B T = \frac{\sigma^2}{2\gamma} \tag{2.6}$$

in which k_B is the Boltzmann's constant and T is the temperature. For simplicity the weight functions are usually chosen to be similar to the form of the conservative force so:

$$\omega^D = [\omega^R]^2 = \begin{cases} \left(1 - \frac{r_{ij}}{r_c}\right) & (r_{ij} < r_c) \\ 0 & (r_{ij} \geq r_c) \end{cases} \tag{2.7}$$

Note that all the forces are pairwise additive and satisfy Newton's Third Law thus conserving linear and angular momentum. A schematic illustration of the acting forces is depicted in **Figure 2.2.**
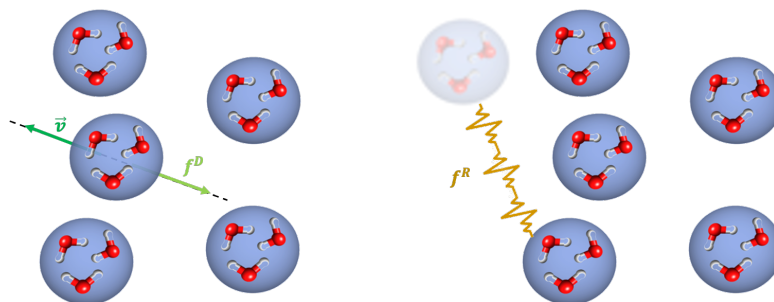
Figure 2.2: Schematic illustration of the dissipative (on the left) and random (on the right) forces.

The numerical values in the DPD equations are at the order of magnitude of one. This practice relies on the "*reduced units*" measurement system, where the mass of a single DPD bead, the cut-off radius, and the thermal energy are typically employed as basic units in DPD.

2.2.1 Why DPD use reduced units?

The use of reduced units in DPD method is beneficial for three main reasons:

1) To avoid extreme values in our calculations. The fact of scaling all the values to unity ensures that the values involved in the calculations are typically within a reasonable range, neither too large nor too small.

2) To make it easier to spot errors in the simulation since extreme values are unlikely to occur. For instance, if we suddenly find a very large (or very small) number in our simulations (say, 10^{42}), there is proof hereof that an error has occurred somewhere.

3) To easily understand the fundamental relationships between variables. By varying one variable while keeping others constant one can examine how changes in that specific variable influence the behavior of the system.

While simulation results acquired in reduced units can always be converted back to real units, this process is not straightforward in CG models. The inherent challenge lies in the imprecise correlation between CG beads and their corresponding atomistic components. However, the basic units can be converted as follows:

- **Mass.** A standard bead is defined to represent 3 water molecules (N_m). Therefore, using eq. 2.8, the real mass can be calculated as:

$$m = N_m \cdot m_{H_2O} \tag{2.8}$$

- **Length:** the basic length unit of length (d_0) is defined as the cutoff diameter (r_c), which can be computed using eq. 2.9 as:

$$r_c = \sqrt[3]{\rho N_m V^w} \tag{2.9}$$

A cube of unit volume 1 d_0^3, is represented by the density, ρ (set to 3 in our simulations), the number of molecules N_m (also 3 as mentioned above), and the approximate volume occupied by a single water molecule (approximately 30 Å^3).

- **Energy:** the unit of energy is defined by the thermostat temperature of the system multiplied by the Boltzmann constant, expressed as:

$$\epsilon_0 = 1 K_B T \tag{2.10}$$

- **Time:** DPD loses track of the real time because CG. The straight-forward approach to determine the time would be based on its inherit relationship with the other units of the system. Meaning:

$$\tau = r_c \sqrt{\frac{m}{\epsilon_0}} \tag{2.11}$$

This choice is particularly useful for investigating equilibrium states, although other options could be also employed. Essentially, there is complete freedom in choosing the time scale. Moreover, it is also important to consider that the time scale is further influenced by the selected time step (Δ_t) and the number of simulation cycles.

- **Temperature:** there are different methods to derive the mapping of reduced temperature to physical units' scale. As we interested in providing qualitative descriptions of several studies, we assume a linear relation between the reduced temperature (T^*) and the physical one, T.

$$T = aT^* + b \tag{2.12}$$

The values of the coefficients a and b can be derived by the linear equations obtained by substituting in this relation the reduced and physical values of temperatures for each simulation.

An example for the conversion of reduced units to physical ones at 30^0C of temperature are collected in **Table 2.1**.

Table 2.1: Conversion of reduced units to international system of units at 303K.

Unit Symbol	Unit Name	Value (DPD units)	Value (Physical units)
m	Mass	1	$9E^{-26}$ kg
d_0	Length	1	$6.46E^{-10}$ m
ϵ_0	Energy	1	$5.15E^{-21}$ J
τ	Time	1	$\sim2.73E^{-12}$ s$\sim$2.73 ps

As said, all the DPD simulation parameters and outputs are usually expressed in reduce (dimensionless) units. So, keep in mind that all the values will be given in reduced units from now on.

2.2.2 Which is the crucial parameter for DPD?

One of the major selling points of DPD is the intuitiveness and ease with which simple models for various complex fluids can be constructed by modifying the conservative interactions with particles. As aforementioned, the conservative force (f^c) is a soft repulsive force given by:

$$f^c = \begin{cases} a_{ij}\left(1 - \dfrac{r_{ij}}{r_c}\right)\hat{r}_{ij} & (r_{ij} < r_c) \\ 0 & (r_{ij} \geq r_c) \end{cases} \qquad (2.13)$$

where a_{ij} is a parameter determining the maximum repulsion between particles. These parameters are usually defined as "Soft Repulsive Interacting Parameters" and that is why **we are going to refer them as SRP in the entire manuscript**. A simple illustration of how the SRP values act along the distance between the centers of the beads is depicted in **Figure 2.3.**
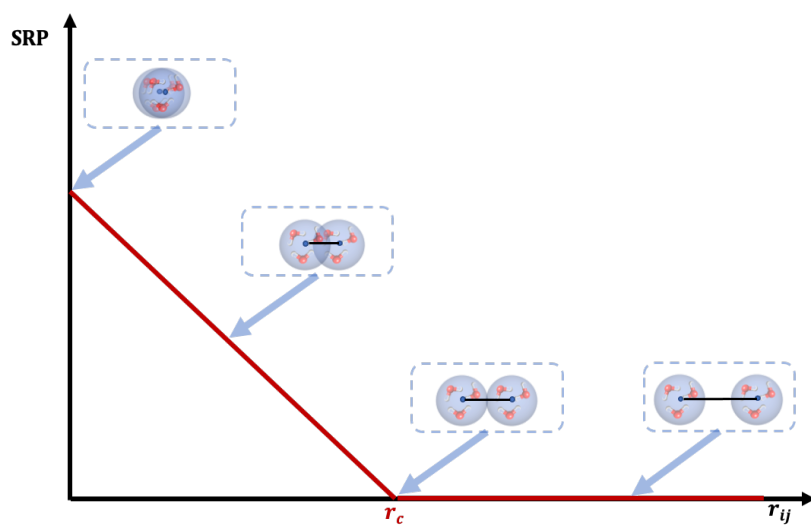
Figure 2.3: Spatial dependence of SRP strength along the distance between two water CG beads.

As one can see, all the SRP values start at their maximum value, thay is to say, when the centers between two beads overlap. As the distance between these centers increases, the SRP values lose momentum. Once the distance reaches or exceeds the r_c, the SRP values become null, meaning that no interaction between such beads will exist. As previously mentioned, the choice of SRP values plays a crucial role in defining what is being represented by a particle.

Since DPD parameters are dimensionless, this choice is arbitrary and not inspired by the physical characteristics of matter unless a mapping is defined and there is a relationship between the simulation and the real parameters established. In this case, the SRP values can be correlated to the one of real matter by matching its surface tension properties.

Groot and Warren[7] proposed a method to match different DPD terms to physical space and time parameters. They introduced the typical value for the self-repulsion between two identical water beads. By reproducing the radial distribution function and the isothermal compressibility of water they derived the following formula:

$$\frac{a_{ii}\, r_c}{K_B T} = \frac{75}{\rho\, r_c^3} \tag{2.14}$$

in which they showed that $\rho\, r_c^3 = 3$ is a good value for the number density meaning that the usual choice for W/W is equal to 25.

To obtain the SRP for a multicomponent system, one might use other ways to derive it. For cases where the simulations are intended to accurately replicate the properties of specific systems and there are no theoretical models to define such potentials, the SRP values are constructed so that they recreate the structural properties of the system of interest. The same authors proposed a simple scaling relation between SRP and the Flory-Huggins χ-parameters that represent the free energy of mixing polymer solutions on a regular lattice[7–9]. This enabled the simulation of various chemical structures because it opened a way to bridge the gap from atomistic simulations where solubility parameters can be calculated to mesoscopic simulations where complex studies can be studied. This route to derive SRP for mixed DPD systems has been applied by several authors. However, the SRP values have been tuned to reproduce either the ionic nature of molecules or to study the self-assembly processes of amphiphilic surfactants into spherical micelles. Venturoli *et al.*[10] parameterized the values to reproduce quantities such as the area per lipid of a DMPC bilayer. Kranenburg and co-workers[11] showed that the phase behavior of different kind of lipids can be obtained by changing the relative interactions between lipid heads and solvent CG beads.

While there are distinct differences to consider, it is important to clarify the correlation between SRP values and their resulting interactions. Higher SRP values lead to more repulsive interactions, while lower values result in more attractive ones. Despite the previous approximations, determining SRP values for metals presents a challenge. To overcome this, we have introduced a new approach to define their metallic nature, which is detailed below:

A) Since the definition of the SRP values for metals is considered a bottleneck, we decided to relate to SRP values of our program with QM calculations. For doing so, we firstly calculated the binding energies ($\Delta E_{binding}$) between the two interacting beads (A and B):

$$\Delta E_{binding} = E_{AB} - (E_A + E_B) \tag{2.15}$$

Accordingly, the individual structures for components A and B as well as for AB were optimized to find the minimum energy. To do so, we used M06-2X[12,13] function with LanL2DZ[14,15] basis set which has become more popular in computations on transition-metal-containing systems. To simulate the effect of solvent (water), we used a polarizable continuum model of water using the integration formalism SMD[16].

These $\Delta E_{binding}$ were related with SRP by the eq. 2.16:

$$SRP = f\left(\Delta E_{binding}\right) \tag{2.16}$$

It is important to highlight that this relationship was considered either exponential (**Chapter 3**) or linear (**Chapters 4** and **5**) depending on the study of interest.

In Case of **Chapter 3**, we used the expression of the formation constant:

$$K = e^{\frac{-\Delta G}{RT}} \tag{2.17}$$

in which K is the formation constant, ΔG is the Gibbs free energy, R is the gas constant and T is the temperature. We assumed that K correlates to the SRP values and ΔG to the $\Delta E_{binding}$.

In contrast, in **Chapters 4** and **5** the relationship was linear since we related them with Flory-Huggins theory[7,17]. Several studies have demonstrated the power of this approach to resolve the differences in the side chains (-*R*) interaction contributions[18,19].

B) The second was adapted from the work Prof. Berend Smit and co-workers[20]. In their study, they introduced an SRP matrix to effectively simulate the effect of cholesterol on protein-protein interactions, aligning with experimental observations. To achieve this, they implemented a parameterization strategy based on the hydrophilic and hydrophobic properties of the beads, as depicted in **Figure 2.4.**
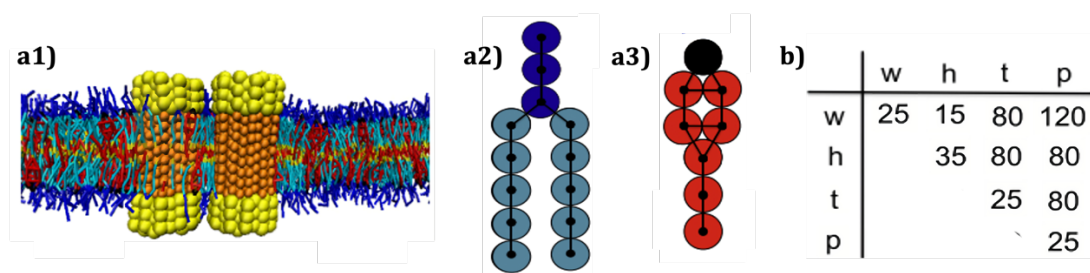
Figure 2.4: CG models for **a1)** bilayer composed of phospholipids and cholesterol, with two embedded proteins; **a2)** phospholipid model and **a3)** cholesterol model. **b)** SRP matrix for water beads (w), which are removed for sake of clarity. Hydrophilic (h) beads depicted in yellow for proteins, and dark blue and black for phospholipids and cholesterol heads, respectively. The hydrophobic tails (t) in light blue for phospholipids and red for cholesterol. Additionally, the most hydrophobic bead (p) corresponds to the internal beads of embedded proteins (depicted in orange). Adapted from reference 20.

As it stands in **Figure 2.4.b)** they used smaller values of SRP for those interactions that were more attractive than W/W such as W/h. In case of hydrophobic beads (t and p) their interactions with the solvent were more repulsive. Furthermore, the value of W/p was increased in comparison to W/t to ensure that the protein core remained within the membrane. With this SRP matrix they were able to simulate the self-assembly of lipids into a bilayer and to reproduce the response of the bilayer and the protein in case of hydrophobic mismatch[21].

In the present thesis we adjusted the hydrophilic and the hydrophobic character of the different beads to derive the SRP values for **Chapters 4** and **5**. Detailed information will be found in the chapters aforesaid.

2.2.3 Bonded Interactions

Bonded interactions were applied to maintain the structure and the topology of the modeled molecules. Such interactions are elastic in nature and can control the strength and the flexibility of a given bond. The equations used are found below:

$$V_{bond} = \frac{1}{2} K_r (r_{ij} - r_{eq})^2 \tag{2.18}$$

$$V_{angle} = \frac{1}{2} K_\theta (\theta_{ijk} - \theta_{eq})^2 \tag{2.19}$$

where V_{bond} and V_{angle} describe the harmonic potential controlling the distance between consecutive beads *i, j* and the angle between beads *i, j, k,* respectively. The values used for each system are described in more detail in **Chapter 8**. Please note that all these parameters are provided in reduced units as described in **section 2.2.1**.

Another fundamental concept for DPD method is the use of Periodic Boundary Conditions (PBC). The description of the concept and discussion about it verses in the following section.

2.2.4 Periodic Boundary Conditions

Nowadays, MD simulations comprises a huge number of atoms ranging from thousands to millions. In such conditions, many atoms would belong to the boundaries of the simulation box experiencing quite different forces from those in bulk. An alternative to overcome the artificial surface effects was to implement what is known as PBC[22]. The essential idea behind this method is to create an infinite system by simply considering multiple repetitions of our initial finite system (bulk effect). For that, a virtual image of our initial finite system (simulated system) is required (**Figure 2.5**).
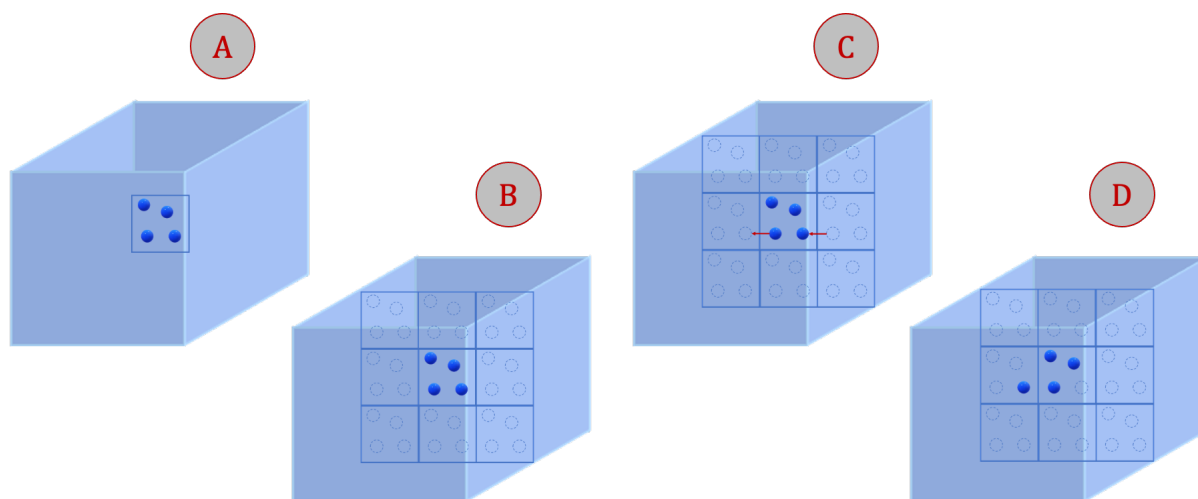

Figure 2.5: Schematic illustration of PBC concept. **A)** Initial box. **B)** Initial box replicated in x, y and z directions. As soon as the blue bead goes out the box (**C)**), its replica replaces it (**D)**).

Figure 2.5 puts forward an overview of PBC concept. The initial box that contains the beads that we want to simulate (**Figure 2.5.A**). Then, the box is replicated in every direction (x, y and z) forming an infinite lattice. In this case, the replica beads are represented in dash circles **(**Figure 2.5.**B**). In the course of the simulation, as a bead moves in the initial box, its periodic image in each of the neighboring boxes moves exactly in the same way **(**Figure 2.5.**C**). Thus, as a bead goes out of the initial box, one of its images will enter through the opposite face (**Figure 2.5.D**).

The application of PBC not only enable beads to experience forces as if they were in bulk solution, but also can dramatically reduce the computational cost needed to simulate large systems. In addition, the total mass and motion of the simulated beads is conserved, so any material or movement is gain or lose. Despite these remarks and because of the repeating pattern, it can create artificial interactions between beads that might not exist in the real system. And therefore, care is still needed when setting up PBC; the unit cell must be large enough that a molecule cannot interact with its periodic images.

2.2.5 Monte Carlo approach

The Monte Carlo (MC) method is a statistical approach for finding approximate solutions to problems by means of random sampling. It is widely applied in many fields such as physics[23,24], chemistry[25,26], biology[27,28], etc. Although earlier examples of MC techniques exist[28] the invention of MC is associated with the newly-discovered neutron in 1930 by Enrico Fermi[29]. Its development was further performed by some physicists who worked in the nuclear weapons program at Los Alamos National Laboratory[30]. Considering the use of randomness and repetitive nature of the sampling process, the technique received this name in reference to the famous casino in Monaco.

The main goal of MC approach is to generate an ensemble of representative configurations under specific conditions for complex systems by applying random perturbations to the system[31]. Our software combines the dynamical advantages of DPD with the ability of MC to equilibrate the system in the right ensemble using a DPD-MC hybrid approach in which the simulation alternates between MC and MD steps.

In this case, MC is used to enhance the sampling of the phase space in DPD simulations by introducing trial moves to the simulation. This trial moves can change the position of velocities of the particles. The acceptance of rejection of these trial moves is determined using a Metropolis acceptance criterion, which ensures that the simulation samples from the correct probability distribution[32].

It is important to note that the simulation steps in the MC technique are steps in configuration space and there is no notion of "time". However, the combination of MC in MD can help to overcome the difficulty of MD in exploring the full conformational space of the system and consequently, can accelerate MD simulations.

2.3. Martini force field

The Martini force field is one of the most widely used CG models implemented in GROMACS[33] software. It was initially developed by Marrink *et al*[34,35] for modelling the properties of lipid bilayers[36]. Over the years, it has been expanded to study biological[37,38] and nonbiological molecules including polymers[39] and nanomaterials[40].

It is based on assigning the main emphasis to simplicity and transferability. The ideology is similar to that of the toy models, since the aim is a wider range of applications rather than focusing on a precise reproduction of structural details. Despite this minimalistic approach, one can use this force field to *"semi-quantitatively"* reproduce a number of structural, dynamical and thermodynamic properties of several systems. Nowadays, Martini offers parameters for a wide variety of lipid molecules[35], cholesterol[41], proteins[37], DNA[42], carbohydrates[38], fullerenes[43], and more.

Different from DPD, the Martini CG model is generally based on a four-to-one mapping of non-hydrogen atoms, *i. e.* four heavy atoms and their corresponding hydrogen atoms are represented by a single interaction center known as CG bead. Consequently, one CG water bead corresponds to four water molecules. Thus, the mass of all standard beads is set to 72 amu for computational efficiency. Although the four-to-one mapping is optimal to represent the chemical properties with computational efficiency, it is considered inadequate to preserve the geometry of small compounds. Therefore, ions are represented by a single CG bead and ring-like fragments are mapped with higher resolution of up to two non-hydrogen atoms to one bead.

The chemical nature of the modeled systems is reproduced using four main classes of CG beads: apolar (C), nonpolar (N), Polar (P) and Charged (Q). Within each class, different subtypes are divided according to the hydrogen-bonding capabilities whether if they are donor (d), acceptor (a), both (da) or none of them (0) or by numbers indicating the degree of polarity from 1 (low polarity) to 5 (high polarity). All these types represent the Martini building blocks[44,45].

To implement the nonbonded and bonded interactions between these building blocks, Martini employs the common potential energy functions as in classical force fields.

2.3.1 Nonbonded Interactions

All particle pairs i and j at distance r_{ij} interact via a Lennard-Jones (LJ) potential:

$$V_{LJ} = \sum_{i,j} 4\varepsilon_{ij} \left[\left(\frac{\sigma}{r_{ij}} \right)^{12} - \left(\frac{\sigma}{r_{ij}} \right)^{6} \right] \tag{2.20}$$

where ε_{ij} and σ denote the characteristic interaction energy and distance respectively for beads i and j. The LJ potential (**Figure 2.6**) has two exponents; the 12-potential increases the energy as the atoms get closer (preventing the collapse of atoms) while 6-potential decreases the energy and models an attractive force that exists between any neutral atoms. In other words, is the short-range repulsion due to the Pauli exclusion principle.
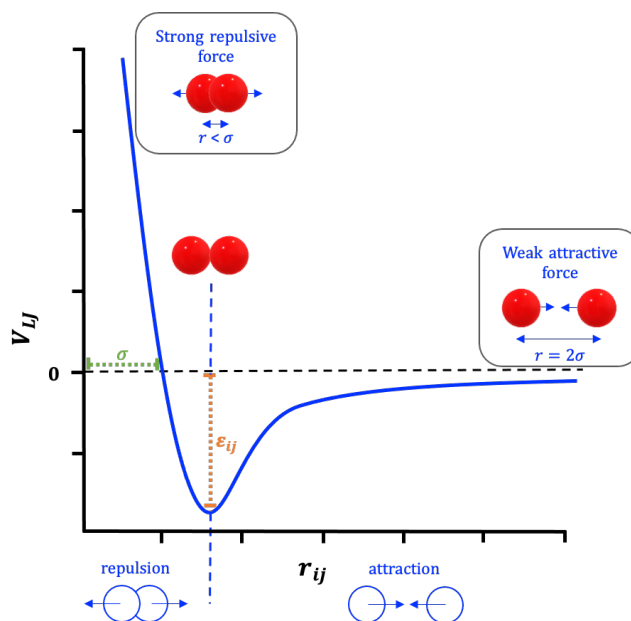
Figure 2.6: Schematic illustration of Lennard-Jones potential form.

The values for ε_{ij} in Martini, depend on the level of interaction and is ranged from 5.6 kJ·mol^{-1} (strongly polar interactions as in bulk water) to 2.0 kJ·mol^{-1} (used to mimic various degrees of hydrophobic repulsion between polar and non-polar phases). On the other hand, the effective size of beads is σ=0.47 nm for all normal beads, σ=0.43 nm for small beads (ring-like molecules) and σ =0.32 nm for tiny beads (nucleobases in the double-stranded DNA helix). Together, these LJ parameters determine how the building blocks interact with each other, giving rise to the heart of Martini, the interaction matrix (**Appendix C2-A**: Interaction matrix for Martini force field[41]).

In addition to LJ interactions, charged groups (Q) bearing a charge q interact via Coulombic energy function:

$$V_C = \frac{q_i q_j}{4\pi\varepsilon_0\varepsilon_{rel}r_{ij}} \tag{2.21}$$

where q_i and q_j are the charges of two particles, ε_0 and ε_{rel} the permittivity of vacuum and the dielectric constant of the solvent, respectively. In this case, ε_{rel}=15 for explicit screening. Note that the Coulomb interaction is computed with a fixed dielectric constant and a cutoff with a reaction field mimicking the effect of homogeneous dielectric environment beyond the cutoff radius, including the effect of ionic strength[46,47].

These values were parametrized based on thermodynamic data describing the different affinities of chemical groups towards different solvent phases, namely, free energies of transfer between water and a number of organic solvents in a top-down approach.

2.3.2 Bonded Interactions

As previously said, bonded interactions are described by a standard set of potential energy functions common in classical force fields. The values are parametrized from the underlying atomistic geometry, usually comparing to experimental data or atomistic simulations in a bottom-up approach.

Like DPD method, the potential energy functions are described including harmonic bond and angle potentials, and multimodal dihedral potentials. However, Martini considers that the chain stiffness is achieved through a weak harmonic potential for the angles:

$$V_\theta = \frac{1}{2} K_\theta[\cos(\theta) - \cos(\theta_0)]^2 \tag{2.22}$$

where θ_0 is the angle at equilibrium. The angular force constant differs for aliphatic chains, and cis/trans unsaturated bonds. In case of aliphatic chains, the angular force constant is 25 KJ·mol^{-1} with a corresponding equilibrium angle of 180°. For cis-unsaturated bonds, the same study showed that the force constant was slightly too weak to reproduce the mapped angle distribution obtained from atomistic simulation. In turn, the angular force constant for *cis* and *trans* unsaturated bonds is 45 KJ·mol^{-1}, while the equilibrium angles are 120° and 180° (**Figure 2.7**), respectively. The different values allow a better fit with atomistic models.
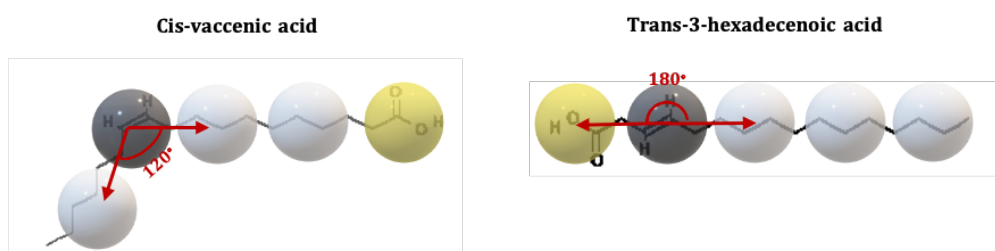
Figure 2.7: Angle between cis (*cis*-vaccenic acid)[48] and *trans* (*trans*-3-hexadecenoic acid)[49] lipid fragments used in Martini force field.

In **Figure 2.7**, both fragments adhere to the standard Martini 2.0 lipids definition. The first fragment corresponds to a segment of lysophosphatidylcholine (LPC), while the second corresponds to phosphatidylglycerol (PG). Both fragments are key components in lipid bilayers. Comprehensive details about their parameterization and respective roles in lipids systems can be found on the Martini website under the names VPC and JFPC, respectively.

It is also worth mentioning that proper dihedrals can be also integrated into the model, when necessary. Their role is to impose secondary structure on peptide backbone. Moreover, improper dihedrals are mainly used to prevent out-of-plane distortions of planar groups. The choice of particle types and interaction potentials for any given systems are chosen based on the thermodynamics properties of the system, or in comparison with atomistic simulations.

2.3.3 Why we decided to use Martini?

One clear advantage of Martini force field is its ease of use compared to other CG methods. Since all of the bead types and their interactions are predefined, one only has to select the appropriate bead type for each CG site. However, this clearly limits the flexibility of the method, and means that cannot always be fine-tuned for every system.

Because of this ease of use, Martini has been extended straightforward manner to construct new molecular species while retaining its internal consistency and compatibility[50]. Although it is advised to try sticking to the use of center of mass (*c.o.m.*) of atom groups in the mapping, in cases of complex molecules it might be more convenient to use specific atoms instead. This will allow a better representation of the mechanistic of the molecule. On the other hand, it has given some useful qualitative and semi-quantitative results relating to the structure and dynamics of many system types including proteins[37,51], carbohydrates[38], polymers[39], DNA[42] which would not have been accessible at the atomistic level.

Herein we employed Martini force field to understand the dynamics of G-quadruplexes (G4s) which are problematic to be simulated in **all-atom** simulations. This study was performed for Prof. Isabel Rozas during my three months stay in Trinity College Dublin (TCD). Although all the simulations have been performed with Martini version 2 is important to mention that further CG beads classes and subtypes have been implemented in the latest Martini version (Martini 3)[52]. However, the latest version does not include the DNA parameters by the moment.

2.4. Analysis of results

Another essential aspect of the present thesis involves the use of tools for visualizing and analyzing the obtained results. In this section, we are going to introduce them.

- **Visualizer**: we employed Visual Molecular Dynamics (VMD)[53] program for its ability to display, animate, and analyze large systems using 3D graphics and integrated scripting capabilities. This tool brings several significant benefits. Firstly, VMD demonstrates versatility with a diverse range of file formats, accommodating not only for ".pdb" but also for ".gro" files produced by Gromacs[47]. Secondly, it provides comprehensive tools for data analysis, thus facilitating result interpretation. Lastly, VMD uses the freely Tcl scripting language, enabling used to develop and implement custom scripts. These scripts can help in determining properties such as the *c.o.m.* for sets of compounds and conducted specialized analyses.

- **Radial Distribution Function (g(r))**: describes how the density of surrounding particles varies as a function of the distance from a reference particle. It Is straightforward to measure it with VMD: you simply select the atoms of interest, specify the maximum distance (r_{max}) for consideration, and define the increments (Δr) for shorter distances intervals. **Figure 2.8** draws a schematic illustration of how these parameters are used in the calculation of the **g(r)**.
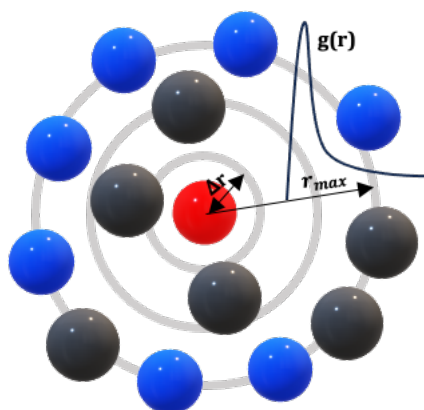
Figure 2.8: Schematic plot of a typical g(r). **Red** particle is the reference particle, and **blue** particles are those which are within the circular shell.

- **Root Mean Square Deviation** (RMSD): provides a quantitative measure of the dissimilarity between two structures. It is an essential tool for measuring structural variations over time, particularly in MD. The RMSD Trajectory Tool in VMD was used for this purpose and it is defined as follows:

$$RMSD = \sqrt{\frac{\sum_{i=1}^{N_{atoms}}(r_i(t_1)-r_i(t_2))^2}{N_{atoms}}} \tag{2.23}$$

where N_{atoms} is the number of atoms whose positions are being compared, and $r_i(t)$ is the position of atom *i* at time *t*.

- **Root Mean Square Fluctuation** (RMSF): is another important metric parameter which measures the displacement of a particular atom, or group of atoms, relative to the reference structure throughout a simulation. It is typically used to identify regions of proteins that are particularly flexible or rigid. In this measure, each atom is assigned an index, and the RMSF measures the average positional fluctuation of each atom index over the course of a simulation[54].

$$RMSF = \sqrt{(x_i - \langle x_i \rangle)^2} \qquad (2.24)$$

where x_i is the coordinates of particle *i*, and $\langle x_i \rangle$ is the ensemble average position of *i*.

- **Radius of gyration** (Rg): estimates the size of a molecule of any shape. The IUPAC gives the next definition:

$$R_g = \sqrt{\frac{\sum_i m_i r_i^2}{\sum_i m_i}} \qquad (2.25)$$

for a rigid particle consisting of mass elements of mass m_i, each located at a distance r_i from the *c.o.m.*, the R_g is defined as the root of the mass-average of r_i^2 for all the mass elements.

- **Density Profile**: provides a spatial distribution of atoms within a system. It represents the number of atoms present in a defined slice or layer when the system box is divided into equal layers. This helps visualize the concentration of atoms in their arrangement in a system.
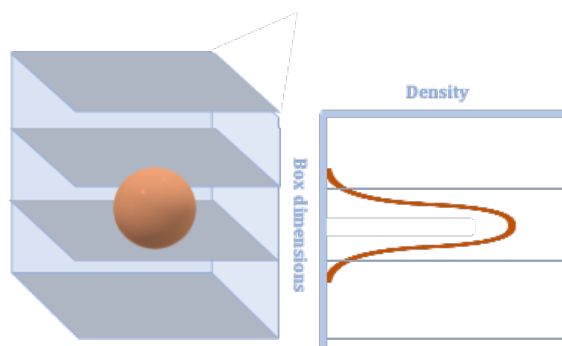
Figure 2.9: Example of the mass density profile of a particle centered on the middle of the box. Layers are depicted in gray.

2.4. References

(1)   Martin, M. G.; Siepmann, J. I. Transferable Potentials for Phase Equilibria. 1. United-Atom Description of n-Alkanes. *J. Phys. Chem. B* **1998**, *102* (14), 2569-2577.

(2)   Yang, L.; Tan, C.; Hsieh, M.-J.; Wang, J.; Duan, Y.; Cieplak, P.; Caldwell, J.; Kollman, P. A.; Luo, R. New-Generation Amber United-Atom Force Field. *J. Phys. Chem. B* **2006**, *110* (26), 13166–13176.

(3)   Dama, J. F.; Sinitskiy, A. V.; McCullagh, M.; Weare, J.; Roux, B.; Dinner, A. R.; Voth, G. A. The Theory of Ultra-Coarse-Graining. 1. General Principles. *J. Chem. Theory Comput.* **2013**, *9* (5), 2466–2480.

(4)   Joshi, S. Y.; Deshmukh, S. A. A Review of Advancements in Coarse-Grained Molecular Dynamics Simulations. *Mol. Simul.* **2021**, *47* (10–11), 786–803.

(5)   Hoogerbrugge, P. J.; Koelman, J. M. V. A. Simulating Microscopic Hydrodynamic Phenomena with Dissipative Particle Dynamics. *Europhys. Lett.* **1992**, *19* (3), 155-160.

(6)   Español, P.; Warren, P. Statistical Mechanics of Dissipative Particle Dynamics. *Europhys. Lett.* **1995**, *30* (4), 191-196.

(7)   Groot, R. D.; Warren, P. B. Dissipative Particle Dynamics: Bridging the Gap between Atomistic and Mesoscopic Simulation. *J. Chem. Phys.* **1997**, *107* (11), 4423–4435.

(8)   Groot, R. D.; Rabone, K. L. Mesoscopic Simulation of Cell Membrane Damage, Morphology Change and Rupture by Nonionic Surfactants. *Biophys. J.* **2001**, *81* (2), 725–736.

(9)   Wijmans, C. M.; Smit, B.; Groot, R. D. Phase Behavior of Monomeric Mixtures and Polymer Solutions with Soft Interaction Potentials. *J. Chem. Phys.* **2001**, *114* (17), 7644–7654.

(10)   Venturoli, M.; Smit, B. Simulating the Self-Assembly of Model Membranes. *Phys. Chem. Comm.* **1999**, *2*(10), 45-49.

(11)   Kranenburg, M.; Smit, B. Phase Behavior of Model Lipid Bilayers. *J. Phys.Chem.B* **2005**, *109* (14), 6553–6563.

(12)   Zhao, Y.; Truhlar, D. G. Applications and Validations of the Minnesota Density Functionals. *Chem. Phys. Lett.* **2011**, *502* (1–3), 1–13.

(13)   Zhao, Y.; Truhlar, D. G. The M06 Suite of Density Functionals for Main Group Thermochemistry, Thermochemical Kinetics, Noncovalent Interactions, Excited States, and Transition Elements: Two New Functionals and Systematic Testing of Four M06-Class Functionals and 12 Other Functionals. *Theor. Chem. Acc.* **2008**, *120* (1–3), 215–241.

(14)   Hay, P. J.; Wadt, W. R. *Ab Initio* Effective Core Potentials for Molecular Calculations. Potentials for K to Au Including the Outermost Core Orbitals. *J. Chem. Phys.* **1985**, *82* (1), 299–310.

(15)   Dunning, T. H.; Hay, P. J. Gaussian Basis Sets for Molecular Calculations. In *Modern Theoretical Chemistry*; Schaefer, H. F., Eds; Springer: Boston, 1977, 1–27.

(16)   Marenich, A. V.; Cramer, C. J.; Truhlar, D. G. Universal Solvation Model Based on Solute Electron Density and on a Continuum Model of the Solvent Defined by the Bulk Dielectric Constant and Atomic Surface Tensions. *J. Phys. Chem. B* **2009**, *113* (18), 6378–6396.

(17)   Español, P.; Warren, P. B. Perspective: Dissipative Particle Dynamics. *J. Chem. Phys.* **2017**, 146, 150901.

(18)   van der Sman, R. G. M. Predicting the Solubility of Mixtures of Sugars and Their Replacers Using the Flory–Huggins Theory. *Food Funct.* **2017**, *8* (1), 360–371.

(19)   Qian, D.; Michaels, T. C. T.; Knowles, T. P. J. Analytical Solution to the Flory–Huggins Model. *J. Phys. Chem. Lett.* **2022**, *13* (33), 7853–7860.

(20)   J-M de Meyer, F.; Rodgers, J. M.; Willems, T. F.; Smit, B. Molecular Simulation of the Effect of Cholesterol on Lipid-Mediated Protein-Protein Interactions. *Biophys. J.* **2010**, *99* (11), 3629-3638.

(21)   Venturoli, M.; Smit, B.; Sperotto, M. M. Simulation Studies of Protein-Induced Bilayer Deformations, and Lipid-Induced Protein Tilting, on a Mesoscopic Model for Lipid Bilayers with Embedded Proteins. *Biophys. J.* **2005**, *88* (3), 1778–1798.

(22)   Born, M.; von Karman, T. Uber Schwingungen Im Raumgittern. *Physikalishe Zeitschrift* **1912**, *13*, 297–309.

(23)   von der Linden, W. A Quantum Monte Carlo Approach to Many-Body Physics. *Phys. Rep.* **1992**, *220* (2–3), 53–162.

(24)   Binder, K. Applications of Monte Carlo Methods to Statistical Physics. *Reports on Progress in Physics* **1997**, *60* (5), 487–559.

(25)   Moebs, W. D. C. A Monte Carlo Simulation of Chemical Reactions. *Math. Biosci.* **1974**, *22*, 113–120.

(26)   Yang, Z. Application of Monte-Carlo Simulations in Environment and Chemistry. *HSET* **2022**, *17*, 5–11.

(27)   Kerr, R. A.; Bartol, T. M.; Kaminsky, B.; Dittrich, M.; Chang, J.-C. J.; Baden, S. B.; Sejnowski, T. J.; Stiles, J. R. Fast Monte Carlo Simulation Methods for Biological Reaction-Diffusion Systems in Solution and on Surfaces. *SIAM J. Sci. Comput.* **2008**, *30* (6), 3126–3149.

(28)   Barbier, J.-E. Note le problème de l'aiguille et le jeu du joint couvert. *J. Math. Pures. Appl.* **1860**, *5,* 273-286.

(29)   Metropolis, N. The Beginning of the Monte Carlo Method *LANL* **1987**, 15, 125-130.

(30)   von Neumann, J.; Richtmyer, R. D. Statistical Methods in Neutron Diffusion. *LAMS-551* **1947**.

(31) Paquet, E.; Viktor, H. L. Molecular Dynamics, Monte Carlo Simulations, and Langevin Dynamics: A Computational Review. *Biomed. Res. Int.* **2015**, *2015*, 1–18.

(32) Neyts, E. C.; Bogaerts, A. Combining Molecular Dynamics with Monte Carlo Simulations: Implementations and Applications. *Theor. Chem. Acc.* **2013**, *132* (2), 1320.

(33) Lindahl, E.; Hess, B.; van der Spoel, D. GROMACS 3.0: A Package for Molecular Simulation and Trajectory Analysis. *J. Mol. Model.* **2001**, *7* (8), 306–317.

(34) Marrink, S. J.; Mark, A. E. Molecular Dynamics Simulation of the Formation, Structure, and Dynamics of Small Phospholipid Vesicles. *J. Am. Chem. Soc.* **2003**, *125* (49), 15233–15242.

(35) Marrink, S. J.; de Vries, A. H.; Mark, A. E. Coarse Grained Model for Semiquantitative Lipid Simulations. *J. Phys. Chem. B* **2004**, *108* (2), 750–760.

(36) Marrink, S. J.; Risselada, J.; Mark, A. E. Simulation of Gel Phase Formation and Melting in Lipid Bilayers Using a Coarse Grained Model. *Chem. Phys. Lipids* **2005**, *135* (2), 223–244.

(37) Monticelli, L.; Kandasamy, S. K.; Periole, X.; Larson, R. G.; Tieleman, D. P.; Marrink, S.-J. The MARTINI Coarse-Grained Force Field: Extension to Proteins. *J. Chem. Theory Comput.* **2008**, *4* (5), 819–834.

(38) López, C. A.; Rzepiela, A. J.; de Vries, A. H.; Dijkhuizen, L.; Hünenberger, P. H.; Marrink, S. J. Martini Coarse-Grained Force Field: Extension to Carbohydrates. *J. Chem. Theory Comput.* **2009**, *5* (12), 3195–3210.

(39) Rossi, G.; Fuchs, P. F. J.; Barnoud, J.; Monticelli, L. A Coarse-Grained MARTINI Model of Polyethylene Glycol and of Polyoxyethylene Alkyl Ether Surfactants. *J. Phys. Chem. B* **2012**, *116* (49), 14353–14362.

(40) Monticelli, L. On Atomistic and Coarse-Grained Models for C_{60} Fullerene. *J. Chem. Theory Comput.* **2012**, *8* (4), 1370–1378.

(41) Marrink, S. J.; Risselada, H. J.; Yefimov, S.; Tieleman, D. P.; de Vries, A. H. The MARTINI Force Field: Coarse Grained Model for Biomolecular Simulations. *J. Phys. Chem. B* **2007**, *111* (27), 7812–7824.

(42) Uusitalo, J. J.; Ingólfsson, H. I.; Akhshi, P.; Tieleman, D. P.; Marrink, S. J. Martini Coarse-Grained Force Field: Extension to DNA. *J Chem. Theory Comput.* **2015**, *11* (8), 3932–3945.

(43) Kitjanon, J.; Khuntawee, W.; Phongphanphanee, S.; Sutthibutpong, T.; Chattham, N.; Karttunen, M.; Wong-ekkabut, J. Nanocomposite of Fullerenes and Natural Rubbers: MARTINI Force Field Molecular Dynamics Simulations. *Polymers* **2021**, *13* (22), 4044.

(44) Marrink, S. J.; Tieleman, D. P. Perspective on the Martini Model. *Chem. Soc. Rev.* **2013**, *42* (16), 6801.

(45) Bruininks, B. M. H.; Souza, P. C. T.; Marrink, S. J. A Practical View of the Martini Force Field. *Methods Mol. Bio.* **2019**, 2022, 105–127.

(46) Tironi, I. G.; Sperb, R.; Smith, P. E.; van Gunsteren, W. F. A Generalized Reaction Field Method for Molecular Dynamics Simulations. *J. Chem. Phys.* **1995**, *102* (13), 5451–5459.

(47) Van Der Spoel, D.; Lindahl, E.; Hess, B.; Groenhof, G.; Mark, A. E.; Berendsen, H. J. C. GROMACS: Fast, Flexible, and Free. *J. Comput. Chem.* **2005**, *26* (16), 1701–1718.

(48) Wassenaar, T. A.; Ingólfsson, H. I.; Böckmann, R. A.; Tieleman, D. P.; Marrink, S. J. Computational Lipidomics with *Insane* : A Versatile Tool for Generating Custom Membranes for Molecular Simulations. *J. Chem. Theory Comput.* **2015**, *11* (5), 2144–2155.

(49) van Eerden, F. J.; de Jong, D. H.; de Vries, A. H.; Wassenaar, T. A.; Marrink, S. J. Characterization of Thylakoid Lipid Membranes from Cyanobacteria and Higher Plants by Molecular Dynamics Simulations. *BBA - Biomembranes* **2015**, *1848* (6), 1319–1330.

(50) Seo, M.; Rauscher, S.; Pomès, R.; Tieleman, D. P. Improving Internal Peptide Dynamics in the Coarse-Grained MARTINI Model: Toward Large-Scale Simulations of Amyloid- and Elastin-like Peptides. *J. Chem. Theory Comput.* **2012**, *8* (5), 1774–1785.

(51) Marrink, S. J.; Risselada, H. J.; Yefimov, S.; Tieleman, D. P.; de Vries, A. H. The MARTINI Force Field: Coarse Grained Model for Biomolecular Simulations. *J. Phys. Chem. B* **2007**, *111* (27), 7812–7824.

(52) Souza, P. C. T.; Alessandri, R.; Barnoud, J.; Thallmair, S.; Faustino, I.; Grünewald, F.; Patmanidis, I.; Abdizadeh, H.; Bruininks, B. M. H.; Wassenaar, T. A.; Kroon, P. C.; Melcr, J.; Nieto, V.; Corradi, V.; Khan, H. M.; Domański, J.; Javanainen, M.; Martinez-Seara, H.; Reuter, N.; Best, R. B.; Vattulainen, I.; Monticelli, L.; Periole, X.; Tieleman, D. P.; de Vries, A. H.; Marrink, S. J. Martini 3: A General Purpose Force Field for Coarse-Grained Molecular Dynamics. *Nat. Methods* **2021**, *18* (4), 382–388.

(53) Humphrey, W.; Dalke, A.; Schulten, K. VMD - Visual Molecular Dynamics. *J. Molec. Graphics* **1996**, *14*, 33–38.

(54) Martínez, L. Automatic Identification of Mobile and Rigid Substructures in Molecular Dynamics Simulations and Fractional Structural Fluctuation Analysis. *PLoS One* **2015**, *10* (3), 1-10.

"Without labor, nothing prospers."

Sophocles

Chapter 3

Is DPD a useful method for studying Au NPs synthesis?

This Chapter attempts to investigate the nucleation and growth steps of Au NPs applying CG models. The main goal was to find a suitable definition of SRP values for describing the metallic nature of Au using DPD method. To do so, five surfactants with different affinity for Au were chosen. A special focus on the surfactant-to-gold binding strength, Surfactant/Au molar ratios as well as the nature and length of the surfactants were considered.

3.1. Chemistry beyond the synthesis of Au NPs

Gold has fascinated mankind since its discovery as quoted by Auric Goldfinger:
"This is gold, Mr. Bond. All my life I've been in love with this color, its brilliance, its divine heaviness".

Being very unreactive, Au does not turnish in the atmosphere and so keeps its attractive color forever. That is why it has been used in many decorative and religious artifacts with a high monetary value. The first milestone in the history of gold ruby glass date back to Roman times and is known as the Lycurgus cup. This cup shows a green jade color due to the diffusion of light when it is illuminated from outside and a deep ruby-red color when it is illuminated from inside. The first one to recognize that the color was related with the size of Au NPs was Prof. M. Faraday[1].

Nanostructured gold materials, as nanomaterials (<100nm), behave differently and are often superior in properties to bulk materials due to two primary factors: surface effects and quantum effects. On one hand, their high surface area to volume ratio makes them very reactive. Thereby, Au NPs with multifunctional activities can be easily obtained. On the other hand, their electronic confinement provides the most powerful means to manipulate their electronic, optical, and magnetic properties. These physicochemical properties are highly dependent not only on material composition but also on their size and shape.

For the sake of preserving their integrity and to prevent their biocompatibility, Au NPs must be stabilized by organic compounds such as surfactants. The growing interest on the synthesis of Au NPs in the last decades is explained by the ability to prepare NPs with a high control on the size distribution. The most common synthesis methods are classified into top-town and bottom-up approaches. While the first one usually employs physical methods including: ultra-violet ration, laser ablation, radiolysis, etc., the second one generally concerns chemical methods such as the reduction of the gold salt into a gold metal.

In the present chapter, we explored the synthesis of Au NPs by bottom-up approaches. Generally, these chemical methods rely in three steps. First, the gold salt is reduced to the gold metal (reduction step). Second, particles started to form clusters, or nuclei (nucleation step). And finally, particles are stabilized via electrostatic, steric or both interactions (growth step) with other compounds such as surfactants.

It is important to mention that even though these steps follow this specific order, they can occur simultaneously. The most common surfactants used to prevent aggregation of the newly synthesized particles are thiolates, amines, carboxylates, alcohols, and others. The surfactant-to-gold binding strength according to Pearson's Hard and Soft Acids and Bases (HSAB) concept[2] is as follows: O<N<S.

There is a long story on the production of Au NPs. The first systematic study of the synthesis and colors of colloidal Au NPs, dating back to 1857, was reported by Prof. M. Faraday[1]. He described the ruby color produced by gold particles via electrochemical reduction of aqueous solution of chloroaurate, $AuCl_4^-$. Nearly one century later, Turkevich *et al.*[3] introduced a new method to produce spherical Au NPs using citrate reduction in water of tetrachloroauric acid, $HAuCl_4$. A further effort to introduce greater control over average particle size by varying the trisodium-to-gold ratio was introduced by Prof. G. Frens in 1973[4].

Since then, numerous applications of Au NPs have led to the development of other approaches for making Au NPs. For instance, Brust and Schiffrin reported a two-phase synthetic strategy to protect Au NPs which impact on the overall field; they used thiol-containing organic compounds which can self-assemble onto Au NPs surface. This route offered the facile synthesis of stable Au NPs with reduced size dispersity and controlled average size[5]. Similar results were obtained by Leff *et al.* who reported the use of primary amines for obtaining amine-capped Au NPs[6].

As aforementioned, the general synthetic pathway for preparing Au NPs involves[7]:

1) The reduction of gold salt to gold metal.

2) The reduced gold, starts to form clusters, initiating the nucleation step.

3) Finally, additional material is deposited on the clusters to obtain the Au NPs. This step is known as the growth step.

Please keep in mind that we considered the atoms in their reduce form. A schematic illustration is shown below (**Figure 3.1**).
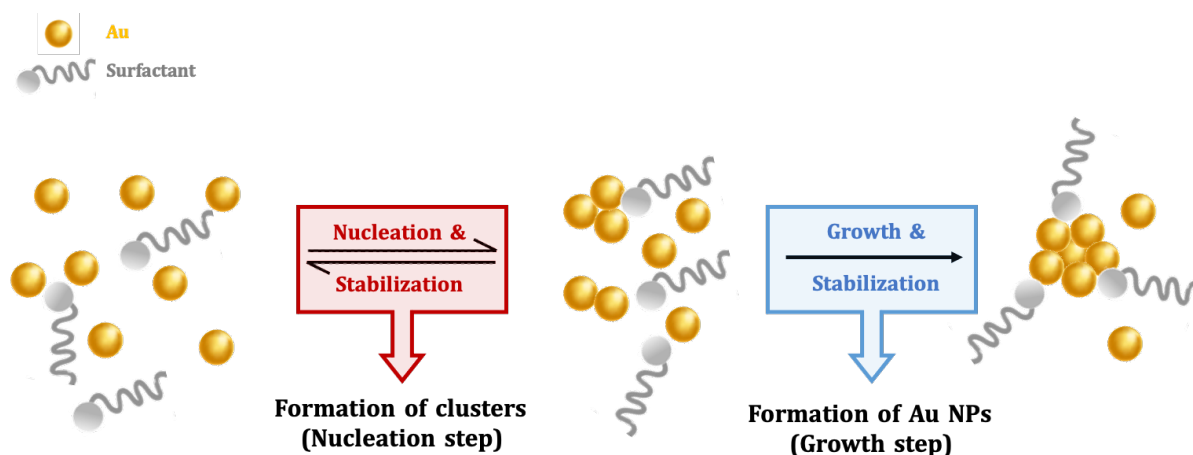
Figure 3.1: Schematic illustration for the nucleation and the growth of Au NPs.

As it stands in **Figure 3.1**, the collision of Au^0 atoms leads to a sudden burst of cluster formation which marks the start of the nucleation step. These clusters have a critical radius that corresponds to the minimum size at which they can stay in solution without being redissolved. The free energy of these clusters should be that critical to obtain stable particles within a solution. The nucleation rate depends on the number of growing units and their mobility. In the following step (growth step), these clusters are either incorporated to Au^0 surface or to other clusters via coalescence or aggregate processes in order to form the desired Au NPs. Unlike the nucleation step, the growth step is considered the rate determining step since it is much slower. Both steps are crucial for controlling the size and shape of the final material as well as their specific functionalities.

The fact of having these intermediate steps (nucleation and growth), which act simultaneously, may result in a broad particle size distribution. However, the modulation of preparing monodisperse Au NPs can be accessed by controlling surfactants properties such as concentration, length, and hydrophobicity. Thanks to the potential advantage of surfactants for tuning the surface and interfacial tension between two or more phases, they may be a key agent in the synthesis of NPs with well-controlled geometries. Their amphiphilic nature not only make them suitable for use in numerous industrial products but also to overcome the current limitations in nanotechnology.

The effect of the surfactants' concentration onto Au NPs was evaluated by Xu *et al.*[8]. They studied the properties of the resultant Au NPs when varying the concentration of the Gemini surfactant (**Figure 3.2.A**). Small-sized Au NPs were obtained at relatively high concentrations of the surfactant, due to the steric hindrance. On the contrary, decreasing the surfactant concentration led to the formation of larger-sized Au NPs. Similar results were obtained by Duangthanu and co-workers[9] who study the aggregation of colloidal Au NPs when changing the concentrations of a non-ionic surfactant, more specifically, Plantacare 2000 (**Figure 3.2.B**). They also concluded that the appearance of the clusters was different depending on the concentration of surfactant. The role of surfactants' concentration was also explained in Shaban and co-workers[10] review. The surfactants not only improve the stability of Au NPs but also control their size distribution. The larger was the tail length of the surfactant, the smaller, less aggregated and a higher number of NPs were obtained.

Regarding the length, Gao *et al.*[11] examined the formation of Au nanostructures using different alkyltrimethylammonium bromides (**Figure 3.2.C**) analogues (C_nTAB in which n=10, 12, 14, 16 and 18). Their results showed that the length tail of surfactants is critical for producing Au nanostructures. Recently, Gemini surfactants with variable length of polymethylene spacer were explored by Pisárčik *et al.*[12]. They concluded that the use of surfactants with short spacer increased the NP size and stability. This was explained considering the strong aggregation tendency of short spacer surfactants.

Another important factor to consider is the surfactant hydrophobicity. Generally, the hydrophobic tail of the surfactants gives to the structure the ability to self-assemble into a dense layer due to the hydrophobic repulsion. These hydrophobic interactions result in a very efficient packing of the molecules onto the Au NPs surface. Such high molecule density on the NPs decreases the molecules mobility[13]. Hassenkam and co-workers[14] predicted that the hydrophobicity of the surfactants' shell should affect the nanostructure formation. At the same time, Aslan *et al.*[15] showed that the physical adsorption of Tween 20 (**Figure 3.2.D**) onto Au NPs would stabilize them against aggregation by means of steric interactions.

Figure 3.2: Surfactants chemical structure.

Up to date, the emerging category of surfactants in nanotechnology has been intensively studied. Nevertheless, it is still necessary to elucidate the fundamental mechanisms and enable the possibility of large-scale production for commercial uses, considering the short history of surfactants since their initial discovery[10]. MD simulations have been valuable in complementing experimental techniques for studying the adsorption of surfactants on metal surfaces. However, parameterizing metal compounds in MD remains challenging due to the intricate nature of their electronic structure, polarization, and coordination geometries. Filling this gap may require the integration of advanced QM methods, refined parameterization techniques and a more comprehensive understanding of metallic complex behavior.

In the present chapter we have introduced a new methodology for defining interactions within metal compounds. Initially, we applied CG models for all the compounds of the system. Concurrently, we calculated the $\Delta E_{binding}$ using QM calculations and linked the resulting values to the SRP values utilized in our program. Subsequently, we explored the influence of five different surfactants during the nucleation step by varying the Surfactant/Au molar ratios. Our research progressed with an examination of Au NPs growth using three established syntheses. Furthermore, we probed the nature and length of the surfactants under study. We should emphasize that our decision to use a pure hydrocarbon chain as a surfactant was largely influenced by the current lack of review articles examining these types of systems.

3.2. Coarse-Grained Model and SRP definition

As previously described in the DPD section of **Chapter 2**, typically one bead is formed by three non-hydrogen atoms. This standard was typically followed in our model, except in the case of gold. Given the requirement for all beads to be of equivalent size and taking into account that a single gold atom occupies half the volume of a water molecule, we modeled Au beads as collections of six gold atoms. In case of surfactants, we followed the convention of representing each bead with approximately three non-hydrogen atoms. **Figure 3.3** puts forward an overview of the CG applied. As one can see, there are seven types of beads:

- A water-like bead, denoted as **W**, which models water.

- A metallic bead, denoted as **Au**, which models gold.

- A thiol-like bead, denoted as **S**, which models the terminal group for both 3-mercaptopropionic acid (MPA) and 11-mercaptoundecanoic acid (MUA).

- A carboxylate-like bead, denoted as **O**, that represents the anion-like fragments of citrate, MPA and MUA molecules.

- An alcohol bead, denoted as **OH**, which models the central alcohol group of citrates (Cit.) molecules.

- A primary amine, denoted as **N**, which models the terminal amine of oleylamine (Ole.) molecules.

- A hydrophobic bead, denoted as **C**, which models the hydrocarbon chains for octadecane (Oct.) MUA and oleylamine molecules.
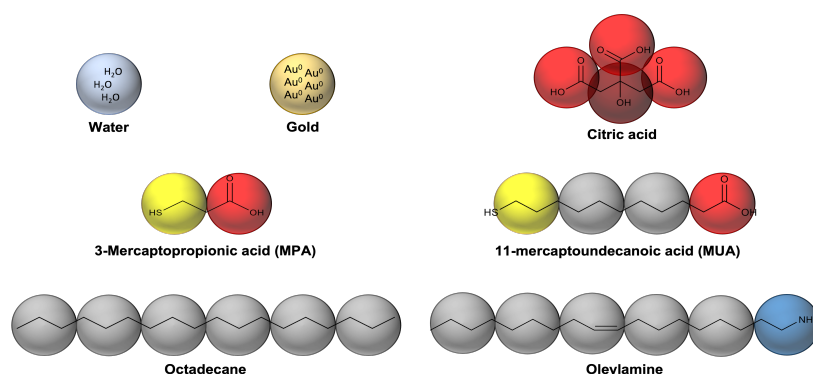

Figure 3.3: Schematic illustration of the CG applied for all compounds. All beads contain three heavy atoms except for gold (type Au) which is formed by six gold atoms. Adapted from reference[16].

In the next step, the SRP matrix to simulate the systems needed to be determined. As said, the definition of metallic behavior in MD is a challenging task due to the metallic bonding properties. An alternative was to derive such properties via QM calculations. We firstly calculated all $\Delta E_{binding}$ by using eq. 2.15 from **Chapter 2**. Detailed information of the resultant values can be found in **Appendix C3-A**: $\Delta E_{binding}$ for the syntheses of Au NPs.

Afterwards, these values were exponentially related with the SRP of our program based on eq. 3.1:

$$K = e^{\frac{-\Delta G}{RT}} \tag{3.1}$$

in which K is the formation constant, ΔG is the Gibbs free energy, R is the gas constant and T is the temperature. We assumed that K corresponds to the SRP values and ΔG to the $\Delta E_{binding}$. To do so, the lowest value of $\Delta E_{binding}$ was assigned to 1 and the $\Delta E_{binding}$ for water to 25 according to Groot and Warren[17]. The highest value was adjusted to obtain the best regression with OriginPro software[18]. The overall matrix as well as the exponential relationships are shown in **Figure 3.4.**

SRP	W	Au	S	O	OH	C	N
W	25	48	54	10	22	82	17
Au		1	5[a]	18	40	55	15
S			56	12	52	78	70
O				10[b]	17	95	46
OH					22	78	20
C						80	85
N							52

$$a_{ij} = 106.1 \cdot e^{(0.1631 \cdot \Delta E_{binding})}$$
$$r^2 = 0.9913$$
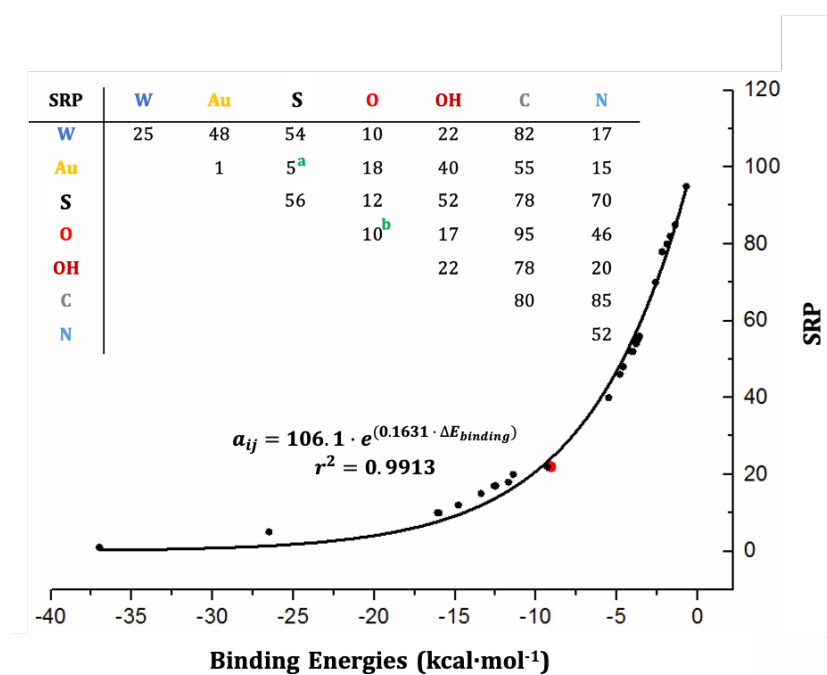
Figure 3.4: Exponential correlation plot between SRP values *vs.* $\Delta E_{binding}$. Red point depicts the **W/W** interactions. Inset: SRP used; **a) S** beads were assumed to interact with **Au** in their negative state; **b) O** beads can undergo protonation or deprotonation depending on the pH, and thus, **O/O** SRP is the average between all the possible interactions between protonated and deprotonated species. Image reproduced from reference [16].

As one can see, the surfactant-to-gold interaction strength is on the same page with Pearson's HSAB concept since **Au**/**OH** < **Au**/**O** < **Au**/**N** < **Au**/**S**. Citrate molecules are labile surfactants that interact weakly with Au by electrostatic interactions (18 and 40 SRP values for **Au**/**O** and **Au**/**OH**, respectively). On the other hand, oleylamines are organic molecules which interact with Au by its terminal N beads (**Au**/**N** = 15). Additionally, their hydrocarbon chain (**C** beads) provides steric stabilization. Finally, **S** beads interact strongly with Au beads due to the formation of a pseudocovalent bond (**Au**/**S** = 5).

These results are likened to Prasad *et al.*[19] studies in which they converted a highly polydisperse colloid into a nearly monodisperse ones using several surfactants. They demonstrated that the final sizes of Au NPs stabilized by different surfactants are highly dependent on the surfactant-to-gold interaction. Overall, they observed that weaker surfactants such as alcohols and amines stabilized larger particles while stronger ones like thiols, stabilized smaller particles. Even though that study clearly showed some features about the effect of surfactant-to-gold interactions, some efforts need to be addressed to apply such results to large-scale synthesis of Au NPs.

To the best of our knowledge, no examples of the use of pure linear hydrocarbon chains for the syntheses of Au NPs in aqueous solution have been reported hitherto. However, several studies predicted that Au NPs can be also used for the enrichment of environmental pollutants as traces of polycyclic aromatic hydrocarbons (PAHs) due to the strong affinity of PAHs for the unmodified surface of Au NPs[20,21]. In this sense and according to the SRP matrix from **Figure 3.4**, we can see that the SRP value for **Au**/**C** is the less repulsive in comparison to the others SRP for **C** beads.

Coming back to the point; once the SRP were determined, we then dealt with the DPD study of the formation of Au NPs. Keep in mind that we did not consider the reduction step since redox reactions are not reachable with DPD method. Therefore, the Au beads were considered in their metallic form. On the other hand, the choice of the surfactants was based on experimental studies in order to know how efficient the SRP values were.

3.3. Formation of Au NPs

In light of the SRP matrix obtained in the last section, we then evaluated the effect of the surfactant in the synthesis of Au NPs. Remember that we focused our attention on the nucleation and growth steps. Within this frame, we considered the following assumptions:

1) Au CG beads behaved similarly to gold atoms. Thus, they were represented in its elementary state, *i.e.,* once tetrachloroauric(III) acid is reduced by sodium citrate (SC).

2) Clusters were formed when roughly 3 Au CG beads (18 Au atoms) joined together.

3) The growth of such clusters led to the formation of Au NPs.

Despite all the studies performed for the synthesis of Au NPs, the minimum number of Au atoms contained either in one cluster or in one Au NP is not evident. Several studies have shown that the value can vary, and it is specific to the cluster being studied or synthesized. However, clusters are usually defined as small Au NPs (<3 nm) that are composed by a few to some hundred atoms[22–28].

For an easier approach, it was decided to split the information into two parts: the first one containing DPD simulations for the nucleation step and the second one containing simulations for studying the formation of Au NPs (growth step).

3.3.1 The Nucleation Step

As stated at the beginning, the nucleation step is basically, the progress in which particles can be self-associated to form clusters. Recent studies have shown that the monomer concentration, in our case, the initial number of Au CG beads, represents a key parameter in determining the path of the colloidal reaction[29]. Moreover, it has been proven that surfactants can also influence the nucleation step and, consequently, can control the morphology and size of the final Au NPs[10]. Despite tremendous progress in experimental techniques for the detection of Au clusters, the development of more efficient, accurate and practicable methods remains necessary. The present section aims to investigate the formation of Au clusters depending on the Au/Surfactant molar ratios and the surfactant structure, chemical nature and length. The idea was to estimate if our simulations were in accordance with previous studies, with the aim of being able to predict results in the future.

To do so, three simulations with Au/Surfactant molar ratios of 0.5, 1 and 2 for each surfactant were run. At the beginning of simulations, Au beads started to group together; however, that aggrupation smaller than the critical nucleation radii redissolve indicating their instability. The number of clusters formed was dependent on the initial number of Au CG beads.

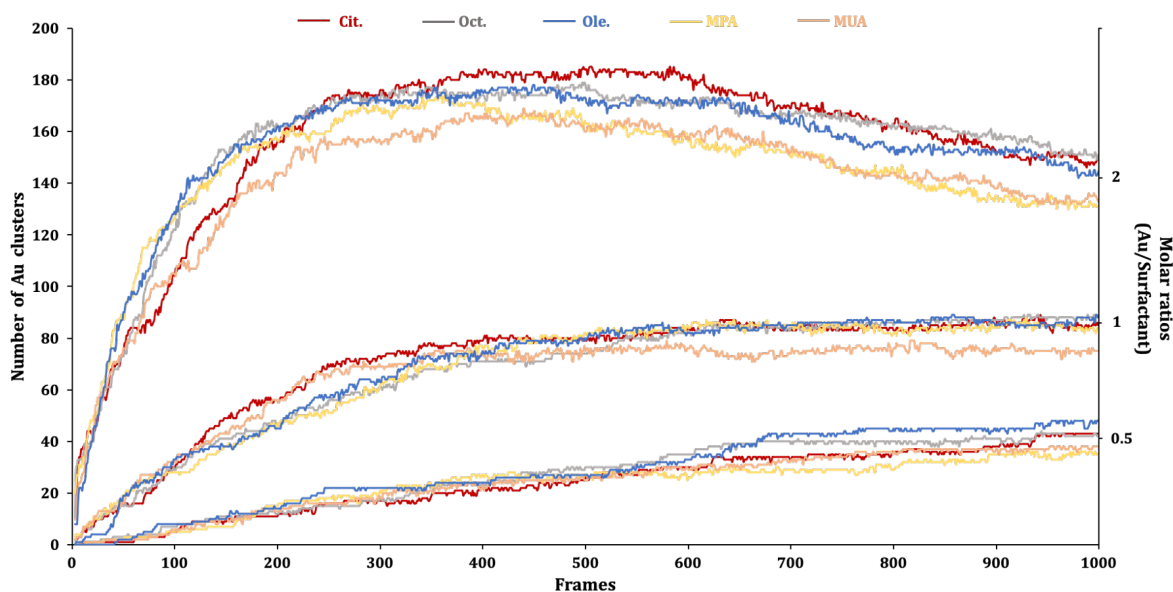Results are plotted in **Figure 3.5**. Please, find the simulation details in **Chapter 8**.

Figure 3.5: Number of Au clusters (on the left) for each surfactant at three Au/Surfactant molar ratios (on the right) along the simulation. Color code: scarlet red for citrate (**Cit.**) molecules, gray for octadecane (Oct.), blue for oleylamine (**Ole.**), yellow for MPA and pastel orange for MUA.

As it stands, **Figure 3.5** is a scatter plot that feeds us with information as to what is the number of Au clusters when changing the Au/Surfactant molar ratios for each surfactant type. Broadly speaking, as the molar ratio increases, the number of clusters formed also increases, with a steep rise in cluster formation occurring at higher Au concentrations. This data suggests that the formation of Au clusters is dependent on Au concentrations, with a threshold Au/Surfactant ratio at which clusters formation becomes more favorable, with a sharp increase in the number of clusters formed beyond this point. It is important to note that other variables such as pH, temperature, etc. may also influence the formation of Au clusters, although we have not considered them.

The tendency of metal suspensions to coagulate in the presence of electrolytes was studied by Frens[4]. To do this, they used six different solutions in which the Au/Cit. molar ratios were varied. Their results showed that at higher concentrations of Cit., the clusters formed were smaller while at lower concentrations of Cit., the Au clusters were bigger. That is to say that the diameter of resulting clusters was governed by the initial amounts of the reactants[30]. Accordingly, Kumar and co-workers[31] developed a model to determine the clusters size distribution depending on citrate concentrations. Such model predicted that the cluster size increased when there was a stoichiometric deficiency of Cit. concentrations and the other way around.

The latter authors[32] also explored the effect of Ole. on the formation of Au clusters. They concluded that, at lower concentrations of Au, the excess of these molecules limited the nucleation processes and slowed down the growth and therefore, the Au clusters were smaller and less reactive. Likewise, the concentration of thiol groups can also have a significant impact on preventing the uncontrolled aggregation or coalesce of gold atoms[33]. Thiols are able to strongly adsorb on metal surface and act to minimize the van der Waals interactions between nearby metallic atoms. And therefore, an increase in the concentration of these surfactants hinders the aggregation of gold atoms and consequently, promotes the formation of larger number of clusters[34].

Yet, on the other side of the spectrum, the chart also illustrates the relationship between the number of clusters formed according to the surfactant nature. Results show an initial increase in the number of clusters as the binding strength increases, followed by a peak and subsequent decline. There is an optimal range of binding strength for cluster formation.

At the same molar ratio (i.e. 2/1) the number of clusters obtained for each surfactant differs. As outlined, the surfactant-to-gold binding strength follows the Pearson's HSAB theory[2] in which: O<N<S. Although Oct. interacts worse than the others, the soft nature of both hydrocarbon chains and gold can facilitate weak interactions which contribute to the adsorption of these chains onto the Au surface[35]. The number of clusters obtained not only depends on the surfactant binding but also with its own structure.

Typically, when surfactants are longer or present complex structure like Cit., it leads to a higher number of clusters. In this scenario, the interaction between Au beads become more challenging, resulting in a slower cluster growth. Additionally, the presence of Cit., with its chelating effect and its influence on cluster formation, affects their interaction. This can hinder the encounter between Au beads and make them to interact slowly. In contrast, MUA and MPA promote the encounter and interaction between Au beads, leading to faster cluster growth and thus, the formation of clusters is reduced.

3.3.2 The Growth Step

This section is the second part of the research developed in the present chapter. The surfactant composition not only affects the formation of Au clusters but also the final size and dispersity of Au NPs. Fundamental studies have shown that the composition of the surfactants can affect the clusters stabilization. If the surfactant-to-gold binding strength is higher, the growth of Au clusters will be limited resulting in small sized NPs with low polydispersity.

The efficiency of SRP values was tested using three well-known procedures for the formation of Au NPs: Turkevich-Frens[3], Aslam *et. al*[36] and Yonezawa's[37] experiments. As aforementioned, in the first one, the synthesis was done in water and involves the reduction of gold salt ($HAuCl_4$) by citrate ions which acts as both a stabilizer and a reducing agent. The resultant dispersion exhibits the presence of spherical and narrowly dispersed Au NPs. Similarly, the second demonstrated that Au NPs can be also synthesized by the complexation of alkylamine molecules in water. At last, the third experiment proposed several methods to obtain stable Au NPs via MPA in water.

For that, different sets of simulations were run adjusting the Surfactant/Au molar ratios from 0.02 to 2.70 according to the syntheses previously mentioned. The number of Au NPs for each surfactant at the end of simulations is collected in **Figure 3.6.**
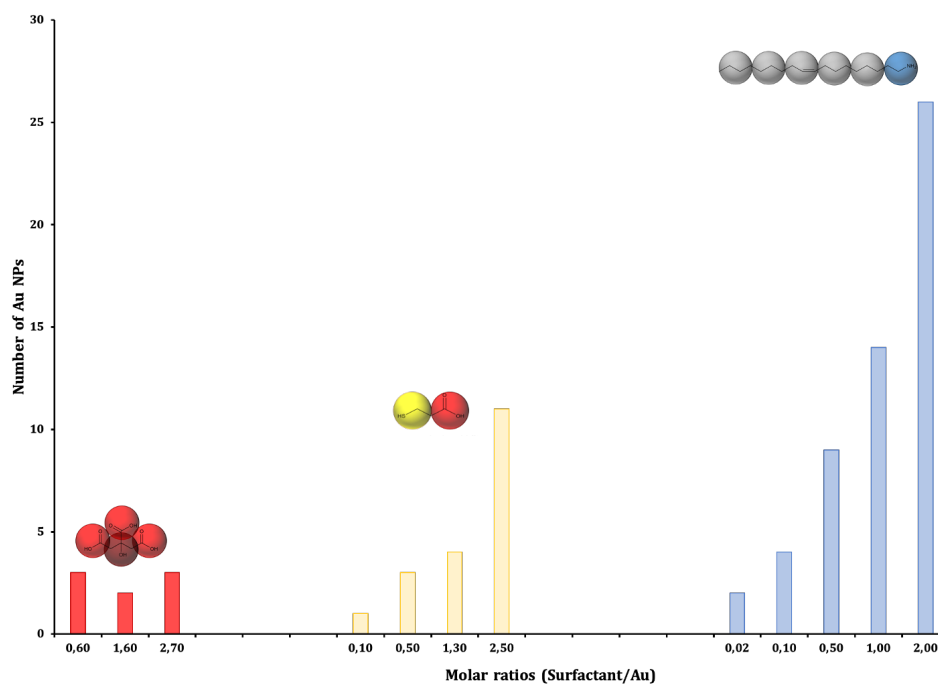
Figure 3.6: Number of Au NPs obtained for each surfactant at different Surfactant/Au molar ratios.

Figure 3.6 shows that increasing the Surfactant/Au generally leads to an increase of the number of Au NPs since they can help to prevent excessive aggregation. However, the trend differs for Cit. molecules, as their number of Au NPs remains almost constant across the three molar ratios. This suggest that Cit. molecules may have a unique stabilization mechanism in comparison to the other surfactants. Even though they present a good interaction with Au beads, they exhibit favorable interactions with water.

Regarding the surfactant-solvent affinity, Min-Soo and co-workers[38] showed that the interaction between surfactants and solvent affect considerably the morphology and the size of Au NPs. When surfactants have strong affinity for water, they tend to be more stabilized in the solvent. Cit. molecules and in some sense also MPA, contain highly hydrophilic groups that can interact with water via hydrogen bonds. Furthermore, Cit. molecules present a strong chelate effect (three anchoring sites) which can enhance their interaction with water and therefore, to contribute to its stability and solvation. This increased stabilization in the solvent results in a weaker interaction between surfactants and Au[39,40]. On the contrary, Ole. surfactants have the tendency to get closer once attached onto Au NP surface to minimize as much as possible its interaction with water.

Yet, on the other side, results also suggest that there is a correlation between the surfactant length and the number of Au NPs obtained. Specifically, as the length of surfactant increases, a higher number of Au NPs are obtained. This indicates that the size of surfactant molecules plays a role in the formation or stabilization of such NPs during the synthesis. Longer surfactant molecules might provide better coverage or stabilization for the growing Au NPs, leading to an increased yield.

The next section gives a detailed information about the role of the surfactant length comparing MPA with MUA when working with the same molar ratios for both.

3.3.2.1 Which is the effect of the surfactants' length?

One such approach in which the tail length of the surfactant was altered to control the NPs size, growth and colloidal stability was reported[41–43]. Qian Liu *et al*[44]. reported the effect of the spacer length of a synthesized Gemini cationic surfactant on the stability of Au NPs. They found that as the spacer length increased, the stability of the synthesized Au NPs increased as well. Similar results have been reported by Pisárčik Martin and co-workers[45] who investigated the correlation between the surfactant structure and stability of Ag NPs. Increasing the length of the hydrophobic carbon chains led to the formation of stable Ag NPs.

Herein, four simulations with Surfactant/Au molar ratios of 0.10, 0.50, 1.30 and 2.50 were performed. The total number of Au NPs obtained are shown in **Figure 3.7**.
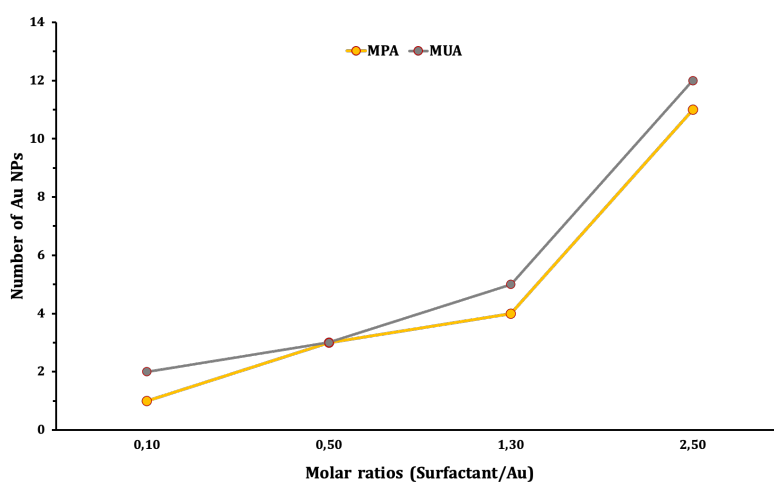

Figure 3.7: Number of Au NPs obtained when using 0.10, 0.50, 1.30 and 2.50 Surfactant/Au molar ratios.

The line chart obtained in **Figure 3.7** furnishes proof about the influence of surfactant length on the obtention of Au NPs. In almost all cases, the number of Au NPs obtained with MUA is greater than with MPA. As aforementioned, the hydrocarbon chain of MUA likely contributes to improve the stabilization and coverage of the Au NPs during their synthesis. Conversely, MPA, may exhibit reduced efficiency in such processes, resulting in a lower number of NPs.

On the other hand, the length of hydrocarbon chains can also introduce steric effects around the Au NPs during their formation[46]. This hindrance limits the accessibility of Au NPs' surface and blocks the access of other beads to the Au NP surface. As a result, the growth of such particles is impeded, favoring the formation of elongated or anisotropic NPs, and thus, increasing the number of Au NPs obtained.

Notably, at higher surfactant concentrations, there is an increased availability of MUA molecules for interacting with Au. And therefore, their ability to bind to the Au NPs is enhanced preventing further aggregation and facilitating their controlled growth. However, the fact of having this strong interaction promotes a unidimensional growth pattern, meaning that NPs tend to growth predominantly in one direction rather than uniformly in all directions. Consequently, at higher concentrations of MUA surfactants, unidimensional growth is promoted, recalling CTAB-Gold nanorod mechanisms of growth (**Figure 3.8**).
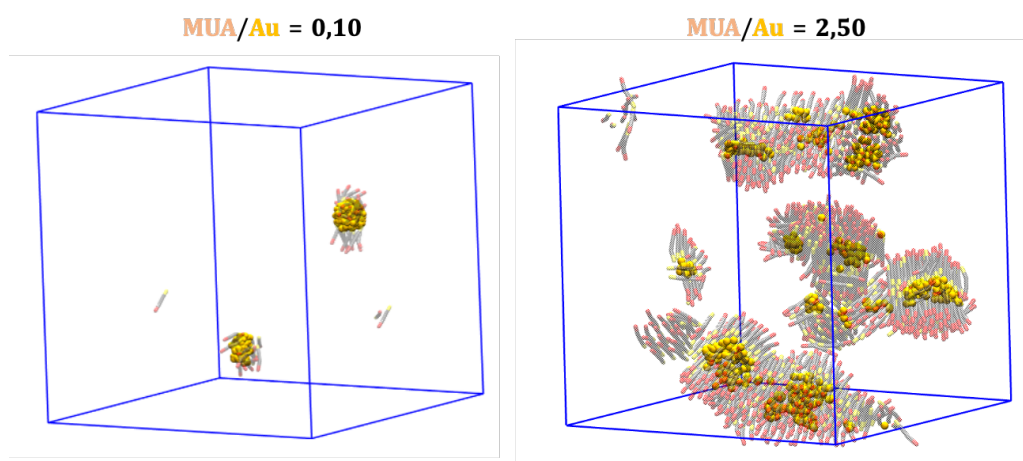

Figure 3.8: Snapshots of the lowest (on the left) and the highest (on the right) MUA/Au molar ratios. Au beads are depicted in dark yellow spheres while MUA molecules are shown in a transparent manner. W beads have been removed for sake of clarity.

3.3.2.2 Experimental study of Au NPs with an excess of MUA molecules

To further verify the previous premises, the group of Prof. Víctor Puntes performed experiments for the synthesis of Au NPs in the presence of both a defect and an excess of MUA. The resultant TEM images are collected in **Figure 3.9**.
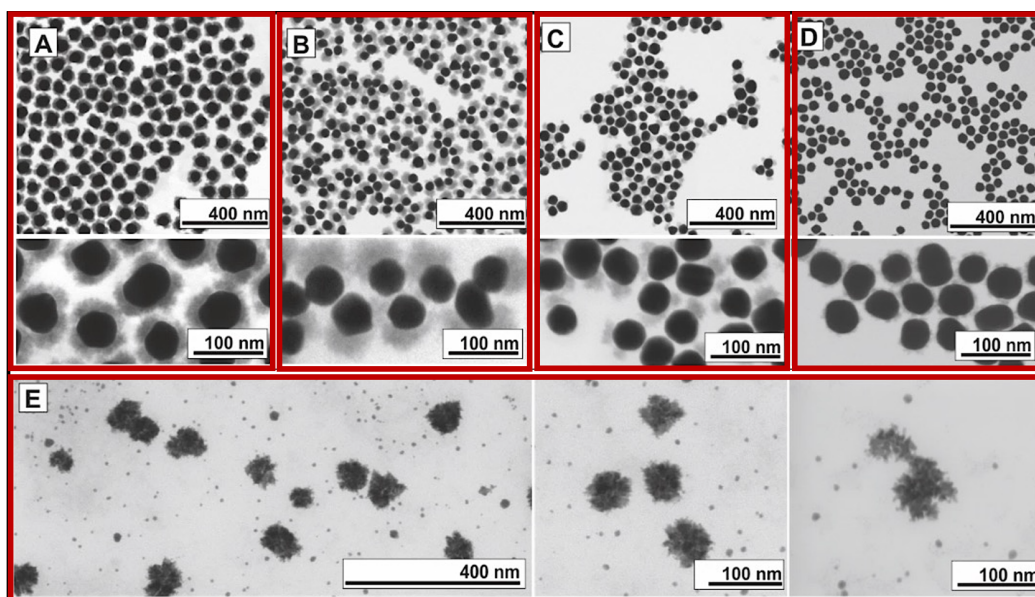

Figure 3.9: TEM images of Au NPs at different MUA molecules to Au surface ratios. A) 0. B) 0.5. C) 50. D) 500. And E) 5000. Adapted from the original reference[16].

As asserted on **Figure 3.9**, the concentration of MUA plays an important role either on both the size and shape of the final Au NPs. At first, citrate-stabilized Au NPs of 50 nm were synthesized[47] in a deficiency of MUA, at concentrations where there was no enough MUA to cover all the NPs surface completely. Such Au NPs were used as seeds for the growth of CeO_2 coating[48]. As expected, while homogeneous CeO_2 layer was grown in the absence of MUA, the formation of separated domains in the form of heterodimer-like structures was observed as MUA concentration was increased (**Figure 3.9.C**). The selective deposition of CeO_2 could be explained by the formation of MUA domains that protect certain areas of the NP surface. As a result, the surface available exposed was reduced, thereby generating binary Au-CeO_2 structures. Otherwise, if subsaturation MUA was evenly distributed on the surface, the corona would take longer and make less dense coronas, but isotropic. Accordingly, the architecture of the final NPs was determined by the concentration of MUA used in the experiment, comprising also complete core–shell (**Figure 3.9.A**) and clover-like structures (**Figure 3.9.B**).
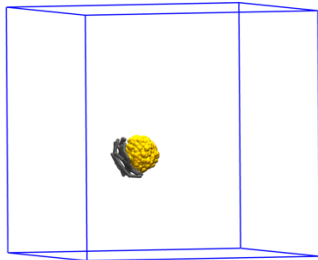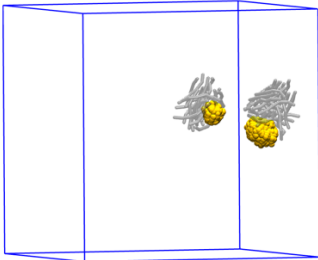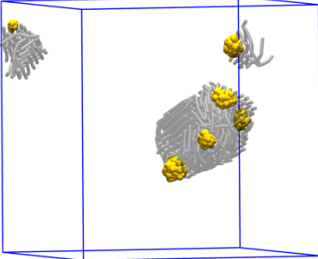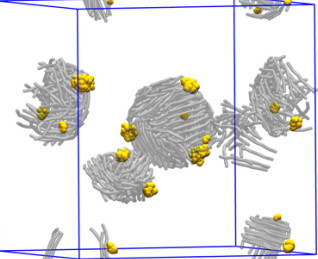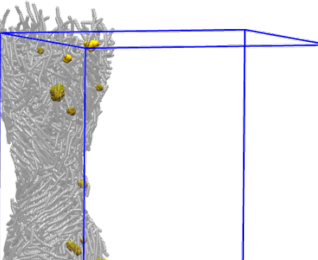
Finally, when the concentration of MUA is the highest tested, the growth of CeO$_2$ is almost suppressed (**Figure 3.9.D**). For the same reasons, the spherical symmetry of the Au NPs was lost when the synthesis of Au NPs was performed in the presence of a high concentration of MUA. Furthermore, the presence of MUA promoted the substantial decrease of Au NP surface energy and the template-assisted growth of Au into spike structures confined in elongated MUA micelles (**Figure 3.9.E**). All the experimental reagents and procedures used to perform the study can be found in **Chapter 8.**

3.3.2.3 What would happen with the use of pure hydrocarbon chains (C type) as surfactants?

As mentioned before, there have not been experimental studies conducted on the utilization of pure hydrocarbon chains for the synthesis of Au NPs since they typically lack on interacting stronger with Au surface. However, several studies[42,49–54] have shown that the hydrophobic tail of the surfactants not only allow them to be adsorbed onto NPs via repulsive forces but also, undergo micellization to stabilize the system by lowering the free energy. Therefore, an increase of surfactant hydrophobicity will enhance both the adsorption and their self-assembly on the NP surface.

In this section, we explored how their hydrophobic effects as well as its concentration impacted on the formation of Au NPs. The chosen molecule to perform this study was octadecane, a surfactant formed by six **C** beads (look at the **Figure 3.3**). The SRP values are defined in the 6th column of the inset in **Figure 3.4.** Five different simulations at different molar ratios were performed. The resultant number of Au NPs as well as the final image obtained for each case are collected in **Table 3.1.**

Table 3.1: Simulations for the synthesis of Au NPs using five different ratios for C surfactants. Water beads removed from clarity.

Molar Ratios Surfactant/Au	Nº of Au NPs	Final structure
0.02	1	
0.1	2	
0.5	6	
1	15	
2	29	

Results show that, despite the low affinity of C-type beads for gold (SRP Au/C = 55), surfactant molecules end up on Au NP surfaces because they are expulsed from water. In words of Charles Tandford[55]: *"The hydrophobic effect is a unique organizing force, based on the repulsion by the solvent instead of attractive forces at the site of organization"*.

In the absence of other attractions, the hydrophobic parts of surfactants interact with the nanomaterials surface. As the tail length increases, the smaller, less aggregated, and more stable are the NPs produced. Sánchez-Iglesias *et al.*[56] proposed a theoretical description for the assembly processes in which they explained that the repulsion due to the polymer chains overcomes the attractive van der Waals interactions, preventing the assembly of Au NPs.

On the other hand, it is worth mentioning that when surfactants concentrations are low, Au NPs surfaces have the potential to connect smaller particles, leading to the creation of larger Au NPs. Feng Xu *et al.*[8] demonstrated that the aggregation of Au clusters to form Au NPs occurred when the surfactant concentration was decreased. Their optical images showed a change in color (which means a different average size of Au NPs) depending on the concentration of surfactants. At lower concentrations, the solution gave rise to dark red or purple dispersions indicating bigger NPs while at higher concentrations, the solution turned to yellow, indicating that the NPs size was decreased.

Interestingly, at higher concentrations of ligands, molecules coalesce forming a separate phase distinct from the water surrounding. This behavior suggests the strategy that the ligands adopt to minimize their interaction with water, thereby reducing unfavorable energy interactions.

3.4. Conclusions

These findings aligned with Pearson's HSB theory, demonstrating that the surfactant-to-gold binding strength follows the order: O<N<S. In the presence of strongly surfactant-to-gold binding, the nucleation and growth processes are slowed until virtually stopped. In contrast, surfactants with weaker bindings facilitate the formation of larger Au NPs, resulting in fewer number of clusters. Furthermore, when the concentration of MUA surfactants was increased, the unidimensional growth of Au NPs was promoted, recalling CTAB-Gold nanorod mechanisms of growth.

A novel study was the exploration of pure linear hydrocarbon chains as stabilizing agent. Despite the low affinity of **C** type surfactants for Au, their repulsion for water makes them to interact with Au.

In summary, this study mapped out the effect of the surfactant's nature in the nucleation and growth steps for the synthesis of Au NPs. From all of what has been said before, one can conclude that CG models are useful to illustrate a wide range of applications in the fields of biomedicine and energy harvesting materials. In addition, DPD is behaving as a powerful tool for studying complex systems in reasonable periods of time, despite its limitation of losing atomic details.

3.5. Highlights of this chapter

The relevant highlights from this chapter are listed below:

- Used QM calculations to consider the metallic nature of Au.

- Related exponentially $\Delta E_{binding}$ with SRP to build a proper SRP matrix.

- Verified that SRP values obey Pearson's HSAB law.

- Studied the effect of surfactants' concentration and nature in the nucleation and growth steps of the Au NPs synthesis.

- Demonstrated the CTAB-Gold nanorod mechanisms of growth at higher concentrations of MUA.

- Predicted observations made by many investigators.

- Studied the effect of hydrophobic interactions when working with pure C-type surfactants.

3.6. References

(1)   Faraday, M. X. The Bakerian Lecture. Experimental Relations of Gold (and Other Metals) to Light. *Philos. Trans. R. Soc. Lond.* **1857**, *147*, 145–181.

(2)   Pearson, R. G. **Hard and Soft Acids and Bases**. *J. Am. Chem. Soc.* **1963**, *85* (22), 3533–3539.

(3)   Turkevich, J.; Stevenson, P. C.; Hillier, J. A Study of the Nucleation and Growth Processes in the Synthesis of Colloidal Gold. *Discuss. Faraday Soc.* **1951**, *11*, 55–75.

(4)   FRENS, G. Controlled Nucleation for the Regulation of the Particle Size in Monodisperse Gold Suspensions. *Nature Physical Science* **1973**, *241* (105), 20–22.

(5)   Bethell, D.; Brust, M.; Schiffrin, D. J.; Kiely, C. From Monolayers to Nanostructured Materials: An Organic Chemist's View of Self-Assembly. *Journal of Electroanalytical Chemistry* **1996**, *409* (1–2), 137–143.

(6)   Leff, D. V.; Brandt, L.; Heath, J. R. Synthesis and Characterization of Hydrophobic, Organically-Soluble Gold Nanocrystals Functionalized with Primary Amines. *Langmuir* **1996**, *12* (20), 4723–4730.

(7)   Thanh, N. T. K.; Maclean, N.; Mahiddine, S. Mechanisms of Nucleation and Growth of Nanoparticles in Solution. *Chem. Rev.* **2014**, *114* (15), 7610–7630.

(8)   Xu, F.; Zhang, Q.; Gao, Z. Simple One-Step Synthesis of Gold Nanoparticles with Controlled Size Using Cationic Gemini Surfactants as Ligands: Effect of the Variations in Concentrations and Tail Lengths. *Colloids Surf. A Physicochem. Eng. Asp.* **2013**, *417*, 201–210.

(9)   Duangthanu, M.; Pattanaporkratana, A. Effect of Surfactant Concentration to Aggregations of Nanogold Particles. *J. Phys. Conf. Ser.* **2017**, *901*, 012098.

(10)   Shaban, S. M.; Kang, J.; Kim, D.-H. Surfactants: Recent Advances and Their Applications. *Compos. Commun.* **2020**, *22*, 100537.

(11)   Gao, J.; Bender, C. M.; Murphy, C. J. Dependence of the Gold Nanorod Aspect Ratio on the Nature of the Directing Surfactant in Aqueous Solution. *Langmuir* **2003**, *19* (21), 9065–9070.

(12)   Pisárčik, M.; Lukáč, M.; Jampílek, J.; Pašková, Ľ.; Bilka, F.; Bilková, A.; Devínsky, F.; Vaľko, J.; Horáková, R.; Hošek, J.; Březina, M.; Opravil, T. Controlled Synthesis of Gemini Surfactant-Capped Gold Nanoparticles. Gemini Structure-Nanoparticle Properties Relationship Study. *J. Mol. Liq.* **2022**, *365*, 120210.

(13)   Pale-Grosdemange, C.; Simon, E. S.; Prime, K. L.; Whitesides, G. M. Formation of Self-Assembled Monolayers by Chemisorption of Derivatives of Oligo(Ethylene Glycol) of Structure HS(CH2)11(OCH2CH2)MOH on Gold. *J. Am. Chem. Soc.* **1991**, *113* (1), 12–20.

(14)   Hassenkam, T.; Nørgaard, K.; Iversen, L.; Kiely, C. J.; Brust, M.; Bjørnholm, T. Fabrication of 2D Gold Nanowires by Self-Assembly of Gold Nanoparticles on Water Surfaces in the Presence of Surfactants. *Advanced Materials* **2002**, *14* (16), 1126-1130.

(15)   Aslan, K.; Pérez-Luna, V. H. Surface Modification of Colloidal Gold by Chemisorption of Alkanethiols in the Presence of a Nonionic Surfactant. *Langmuir* **2002**, *18* (16), 6059–6065.

(16)   Suárez-López, R.; Puntes, V. F.; Bastús, N. G.; Hervés, C.; Jaime, C. Nucleation and Growth of Gold Nanoparticles in the Presence of Different Surfactants. A Dissipative Particle Dynamics Study. *Sci. Rep.* **2022**, *12* (1), 13926.

(17)   Groot, R. D.; Warren, P. B. Dissipative Particle Dynamics: Bridging the Gap between Atomistic and Mesoscopic Simulation. *J. Chem. Phys.* **1997**, *107* (11), 4423–4435.

(18)   OriginLab Corporation, Northampton, MA, USA.

(19)   Prasad, B. L. V.; Stoeva, S. I.; Sorensen, C. M.; Klabunde, K. J. Digestive-Ripening Agents for Gold Nanoparticles: Alternatives to Thiols. *Chem. Mater.* **2003**, *15* (4), 935–942.

(20)   Liu, S.; Lämmerhofer, M. Functionalized Gold Nanoparticles for Sample Preparation: A Review. *Electrophoresis* **2019**, *40* (18-19), 2438-2461.

(21)   Wang, H.; Campiglia, A. D. Determination of Polycyclic Aromatic Hydrocarbons in Drinking Water Samples by Solid-Phase Nanoextraction and High-Performance Liquid Chromatography. *Anal. Chem.* **2008**, *80* (21), 8202–8209.

(22)   Liu, X.; Atwater, M.; Wang, J.; Huo, Q. Extinction Coefficient of Gold Nanoparticles with Different Sizes and Different Capping Ligands. *Colloids Surf. B Biointerfaces* **2007**, *58* (1), 3–7.

(23)   Curry, T.; Kopelman, R.; Shilo, M.; Popovtzer, R. Multifunctional Theranostic Gold Nanoparticles for Targeted CT Imaging and Photothermal Therapy. *Contrast Media Mol. Imaging* **2014**, *9* (1), 53–61.

(24)   Mori, T.; Hegmann, T. Determining the Composition of Gold Nanoparticles: A Compilation of Shapes, Sizes, and Calculations Using Geometric Considerations. *J. Nanopart. Res.* **2016**, *18* (10), 295-331.

(25)   Zhang, J.; Li, Z.; Huang, J.; Liu, C.; Hong, F.; Zheng, K.; Li, G. Size Dependence of Gold Clusters with Precise Numbers of Atoms in Aerobic Oxidation of D-Glucose. *Nanoscale* **2017**, *9* (43), 16879–16886.

(26)   Bain, D.; Maity, S.; Debnath, T.; Das, A. K.; Patra, A. Luminescent Au_6 and Au_8 Nanoclusters from Ligand Induced Etching of Au Nanoparticles. *Mater. Res. Express* **2019**, *6* (12), 124004.

(27)   Cheng, D.; Liu, R.; Hu, K. Gold Nanoclusters: Photophysical Properties and Photocatalytic Applications. *Front. Chem.* **2022**, *10*.

(28)   Thumu, U.; Pradeep, T. Ag and Au Nanoclusters. In *Atomically Precise Metal Nanoclusters*; Pradeep, T., Eds; Elsevier, 2023, 343–393.

(29) Rempel, J. Y.; Bawendi, M. G.; Jensen, K. F. Insights into the Kinetics of Semiconductor Nanocrystal Nucleation and Growth. *J. Am. Chem. Soc.* **2009**, *131* (12), 4479–4489.

(30) Volkert, A. A.; Subramaniam, V.; Haes, A. J. Implications of Citrate Concentration during the Seeded Growth Synthesis of Gold Nanoparticles. *Chem. Commun.* **2011**, *47* (1), 478–480.

(31) Kumar, S.; Gandhi, K. S.; Kumar, R. Modeling of Formation of Gold Nanoparticles by Citrate Method. *Ind. Eng. Chem. Res.* **2007**, *46* (10), 3128–3136.

(32) Ramamoorthy, R. K.; Yildirim, E.; Barba, E.; Roblin, P.; Vargas, J. A.; Lacroix, L.-M.; Rodriguez-Ruiz, I.; Decorse, P.; Petkov, V.; Teychené, S.; Viau, G. The Role of Pre-Nucleation Clusters in the Crystallization of Gold Nanoparticles. *Nanoscale* **2020**, *12* (30), 16173–16188.

(33) Goswami, N.; Yao, Q.; Chen, T.; Xie, J. Mechanistic Exploration and Controlled Synthesis of Precise Thiolate-Gold Nanoclusters. *Coord. Chem. Rev.* **2016**, *329*, 1–15.

(34) Chen, X.; Wei, M.; Jiang, S.; Förster, S. Two Growth Mechanisms of Thiol-Capped Gold Nanoparticles Controlled by Ligand Chemistry. *Langmuir* **2019**, *35* (37), 12130–12138.

(35) de Weldige, K.; Rohwerder, M.; Vago, E.; Viefhaus, H.; Stratmann, M. Adsorption of Self-Assembled Monolayers of Mercaptan on Gold. *Anal. Bioanal. Chem.* **1995**, *353* (3–4), 329–332.

(36) Aslam, M.; Fu, L.; Su, M.; Vijayamohanan, K.; Dravid, V. P. Novel One-Step Synthesis of Amine-Stabilized Aqueous Colloidal Gold Nanoparticles. *J. Mater. Chem.* **2004**, *14* (12), 1795-1797.

(37) Yonezawa, T.; Kunitake, T. Practical Preparation of Anionic Mercapto Ligand-Stabilized Gold Nanoparticles and Their Immobilization. *Colloids Surf. A Physicochem. Eng. Asp.* **1999**, *149* (1–3).

(38) Min-Soo, K.; Ha-Seung, S.; Park, H. J. P.; Sung-Joo, H. Effect of Solvent Type on the Nanoparticle Formation of Atorvastatin Calcium by the Supercritical Antisolvent Process. *Chem. Pharm. Bull.* **2012**, *60* (4), 543–547.

(39) Winter, N.; Vieceli, J.; Benjamin, I. Hydrogen-Bond Structure and Dynamics at the Interface between Water and Carboxylic Acid-Functionalized Self-Assembled Monolayers. *J. Phys. Chem. B* **2008**, *112* (2), 227–231.

(40) Li, Y.; Huang, S.; Zhou, S.; Fane, A. G.; Zhang, Y.; Zhao, S. Enhancing Water Permeability and Fouling Resistance of Polyvinylidene Fluoride Membranes with Carboxylated Nanodiamonds. *J. Memb. Sci.* **2018**, *556*, 154–163.

(41) Peng, X.; Yuan, Y.; Wang, H.; Liang, C. Aqueous Stability and Mobility of C60 Complexed by Sodium Dodecyl Benzene Sulfonate Surfactant. *J. Environ. Sci.* **2016**, *42*, 89–96.

(42)   Badr, E. a; Hefni, H. H. H.; Shafek, S. H.; Shaban, S. M. Synthesis of Anionic Chitosan Surfactant and Application in Silver Nanoparticles Preparation and Corrosion Inhibition of Steel. *Int J. Biol. Macromol.* **2020**, *157*, 187–201.

(43)   Ordóñez, F.; Chejne, F.; Pabón, E.; Cacua, K. Synthesis of ZrO2 Nanoparticles and Effect of Surfactant on Dispersion and Stability. *Ceram. Int.* **2020**, *46* (8), 11970–11977.

(44)   Liu, Q.; Guo, M.; Nie, Z.; Yuan, J.; Tan, J.; Yao, S. Spacer-Mediated Synthesis of Size-Controlled Gold Nanoparticles Using Geminis as Ligands. *Langmuir* **2008**, *24* (5), 1595–1599.

(45)   Pisárčik, M.; Lukáč, M.; Jampílek, J.; Bilka, F.; Bilková, A.; Pašková, Ľ.; Devínsky, F.; Horáková, R.; Opravil, T. Silver Nanoparticles Stabilised with Cationic Single-Chain Surfactants. Structure-Physical Properties-Biological Activity Relationship Study. *J. Mol. Liq.* **2018**, *272*, 60–72.

(46)   Paulini, R.; Frankamp, B. L.; Rotello, V. M. Effects of Branched Ligands on the Structure and Stability of Monolayers on Gold Nanoparticles. *Langmuir* **2002**, *18* (6), 2368–2373.

(47)   Bastús, N. G.; Comenge, J.; Puntes, V. Kinetically Controlled Seeded Growth Synthesis of Citrate-Stabilized Gold Nanoparticles of up to 200 Nm: Size Focusing versus Ostwald Ripening. *Langmuir* **2011**, *27* (17), 11098–11105.

(48)   Piella, J.; Gónzalez-Febles, A.; Patarroyo, J.; Arbiol, J.; Bastús, N. G.; Puntes, V. Seeded-Growth Aqueous Synthesis of Colloidal-Stable Citrate-Stabilized Au/CeO2 Hybrid Nanocrystals: Heterodimers, Core@Shell, and Clover- and Star-Like Structures. *Chem. Mater.* **2019**, *31* (19), 7922–7932.

(49)   Chekuri, R. D.; Tirukkovalluri, S. R. Synthesis of Cobalt Doped Titania Nano Material Assisted by Gemini Surfactant: Characterization and Application in Degradation of Acid Red under Visible Light Irradiation. *S. Afr. J. Chem. Eng.* **2017**, *24*, 183–195.

(50)   Yuenyongsuwan, J.; Nithiyakorn, N.; Sabkird, P.; O'Rear, E. A.; Pongprayoon, T. Surfactant Effect on Phase-Controlled Synthesis and Photocatalyst Property of TiO2 Nanoparticles. *Mater. Chem. Phys.* **2018**, *214*, 330–336.

(51)   Khan, Z.; Al-Zahrani, S. A.; AlSulami, Q. A.; Al-Thabaiti, S. A.; Al-Arjan, W. S. Effects of Shape-Controlling Cationic and Anionic Surfactants on the Morphology and Surface Resonance Plasmon Intensity of Silver@copper Bimetallic Nanoparticles. *J. Mol. Liq.* **2019**, *275*, 354–363.

(52)   Li, D.; Fang, W.; Feng, Y.; Geng, Q.; Song, M. Stability Properties of Water-Based Gold and Silver Nanofluids Stabilized by Cationic Gemini Surfactants. *J. Taiwan Inst. Chem. Eng.* **2019**, *97*, 458–465.

(53) Naderi, O.; Nyman, M.; Amiri, M.; Sadeghi, R. Synthesis and Characterization of Silver Nanoparticles in Aqueous Solutions of Surface Active Imidazolium-Based Ionic Liquids and Traditional Surfactants SDS and DTAB. *J. Mol. Liq.* **2019**, *273*, 645–652.

(54) Shaban, S. M.; Kim, D.-H. The Influence of the Gemini Surfactants Hydrocarbon Tail on In-Situ Synthesis of Silver Nanoparticles: Characterization, Surface Studies and Biological Performance. *Korean J. Chem. Eng.* **2020**, *37* (6), 1008–1019.

(55) Tanford, C. The Hydrophobic Effect and the Organization of Living Matter. *Science* **1978**, *200* (4345), 1012–1018.

(56) Sánchez-Iglesias, A.; Grzelczak, M.; Altantzis, T.; Goris, B.; Pérez-Juste, J.; Bals, S.; Van Tendeloo, G.; Donaldson, S. H.; Chmelka, B. F.; Israelachvili, J. N.; Liz-Marzán, L. M. Hydrophobic Interactions Modulate Self-Assembly of Nanoparticles. *ACS Nano* **2012**, *6* (12), 11059–11065.

"I have emphasized experiments more than theory.
Of course, we need some theory when thinking of soft matter".
Pierre-Gilles de Gennes (1991)

Chapter 4

Is it possible to obtain Janus distributions onto Au NPs?

This chapter is the result of a cooperative project with Prof. Víctor F. Puntes and Dr. Neus G. Bastús from ICN2. The purpose was to develop bispecific Au NPs through the cooperative adsorption of two IgG onto their surface[1]. Within this context, the current chapter aims to provide a comprehensive exploration of the necessary parameters for achieving Janus distributions of IgGs on Au NPs using CG models.

4.1. The Janus grains

In words of Pierre-Gilles de Gennes at the Nobel Lecture, December 9, 1991[2]:

"Let me quote still another new animal: the Janus grains, first made by C. Casagrande and M. Veyssié. The god Janus had two faces. The grains have two sides: one apolar, and the other polar. Thus, they have certain features in common with surfactants. But there is an interesting difference if we consider the films which they make, for instance at a water/air interface. A dense film of a conventional surfactant is quite impermeable. On the other hand, a dense film of Janus grains always has some interstices between the grains, and allows for chemical exchange between the two sides; "the skin can breathe". This may possibly be of some practical interest".

The name "*Janus*" comes from the Roman god of doorways, traditionally depicted with two back-to-back faces -one looking to the past and the other towards the future (**Figure 4.1**). This concept was adopted to describe the amphiphilic nature of complex systems, characterized by one hydrophilic side and one hydrophobic side. To describe spherical particles with this property, Casagrande *et al.*[3] introduced the term "*Janus beads*". Their experiments consisted of preparing glass spherical particles with two distinct hemispheres at oil/water interfaces. The results showed that these "*Janus beads*" behaved differently from ordinary solid particles at liquid/liquid interfaces. As a result, they called them *"amphiphilic solids"* due to their dual surface affinity and their unique solid properties, drawing an analogy to the familiar behavior of surfactant molecules.
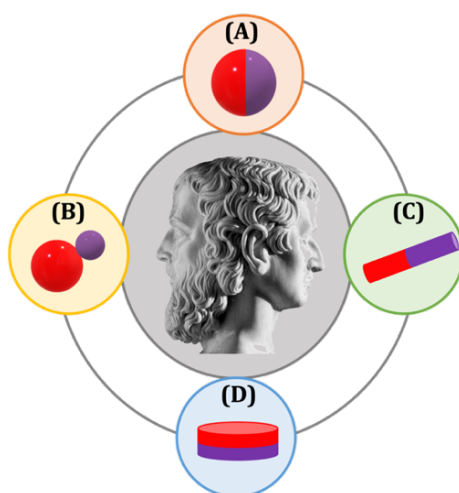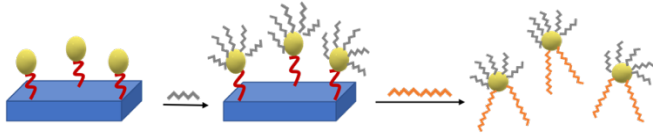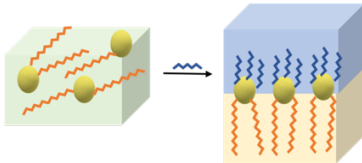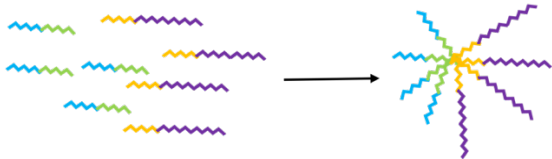

Figure 4.1: Schematic illustration of the Roman god Janus (center) and four morphologies of Janus particles. **(A)** Spherical. **(B)** Snowman. **(C)** Rod & **(D)** Disc.

Since then, Janus particles have been extensively studied far beyond the original structure[4] and have impacted in various fields including catalysis[5], optics[6] and biomedicine[7,8]. Their unique characteristic of having two distinct faces within a single particle not only allows to have distinct domains in different physicochemical nature but also the properties of each domain are seldom altered or lost. Janus particles can adopt a variety of shapes such as spherical (**Figure 4.1.A**), snowman (**Figure 4.1.B**)[9], rod-shape[10] (**Figure 4.1.C**), disk-shape[11] (**Figure 4.1.D**), and more[12,13].

It is well-known that the properties and applications of these systems are highly dependent on their surface chemistry, as well as the morphology they adopt, with defined size and chemical composition. Initially, the most significant challenge was finding out new routes to produce Janus particles with higher reaction yields. Due to their anisotropic structure, they were considered the most complicated colloidal particles in existence. However, innovative methods have been developed to make their production more feasible. **Table 4.1.** briefly summarizes the most common fabrication approaches used.

Table 4.1: Common fabrication approaches, schematic procedures and applications for Janus particles.

Fabrication Approaches	Schematic Procedure	Applications
1. Surface modification		Analytical sensors[14]
2. Phase separation		Theragnostic agents[15]
3. Self - assembly		Drug delivery[16]

While this chapter is not focused on the synthesis of these particles, it does provide a brief explanation of the processes involved. The first approach consists of stabilizing one face of the particle while leaving the other unchanged. To achieve this, the NP is immobilized on a solid surface and subsequently their exposed upper part is modified. Once the NP is fully covered, another NP-like compound is added in the solution to detach the NP from the solid surface. The second approach is useful for incompatible compounds that need to coexist in different phases. To obtain Janus distributions, an immiscible substance is introduced to the system to induce phase separation. The third approach takes place when several compounds of a disordered system are associated into a highly arranged/ordered system that can draw some specific patterns or structures[13,17,18].

Depending on the materials that they are made of, they can be classified into three categories[19]:

- polymeric or organic which present higher stability, flexibility, and biocompatibility.

- Inorganic Janus particles that produce varied architectures and can be easily obtained by controlled synthesis.

- Hybrid organic/inorganic particles that are useful to reduce the cytotoxicity and to enhance the interactions with living organisms.

This chapter primarily addresses hybrid Janus particles, which consist of inorganic cores that are covered either with one or two distinct organic or biological compounds, also known as, ligands[20]. These particles present different properties compared to their purely counterparts, thus offering multifunctional activities. While the metallic core provides mechanical, photoelectric, and magnetic properties, the organic compounds present potential applications from drug delivery to bioimaging and theragnostics[21].

Despite the huge amount of experimental work carried out in this field, a better understanding of the complex relationship between the structure and functionality of Janus particles needs raising. Thanks to the mounting availability of computational power, theoretical studies have begun to shed light on the interactions of Janus particles. One of the first steps in this direction was to employ computational methods to model the properties of self-assembly monolayers (SAMs) onto Au NPs[22]. In essence, studying how ligands can interact on a NPs surface provides insight into the complexity of engineering dualistic surface.

The first theoretical report about Janus distributions onto Au NPs was published by Singh *et al.*[23]. They used atomistic and mesoscopic simulations to explain the unexpected stripe-like patterns of two immiscible surfactants on Au NPs. Three years later, Ghorai and Glotzer identified the difference in ligand length and NP size as a key determinant of the morphology of self-assembled monolayers employing all-atom techniques[24]. Further studies on tripe-like patterns were done by Ge *et al.*, concluding that striped domain separation takes place on NP surfaces when the ligands possess specific physicochemical properties[25]. More recently, these advanced techniques have also been used for getting insights on interfacial properties. Furthermore Velachi *et al.* [26] findings had also had relevant implications on the binding nature in biological processes.

To the best of our knowledge, no previous simulation work aimed at obtaining Janus distributions with two IgGs on Au NPs using DPD has been conducted. Hence, this chapter focuses on identifying the necessary SRP values to obtain Janus distribution onto Au NPs using two different IgGs. When applying CG models to these systems, at least, two factors should be considered:

1) The class they belong to. In this case, both are part of IgG class, and therefore, the same CG approach will apply to both. In this context, we consider two important components of IgG: the Crystallizable Fragment (F_c) and the Antigen Binding Fragment (F_{ab}), which is responsible for antigen recognition.

2) Their AAs composition. This is time to keep in mind that Janus distributions are achieved when the compounds exhibit opposite properties. Hence, the more similar the IgGs are, the more challenging it becomes to achieve Janus distribution. Given that they belong to the same class, their differences will primarily lie in the aforementioned F_{ab}.

4.2. The simplest model

As previously noted, obtaining Janus distributions on Au NPs primarily depends on the structure (their class: IgG, IgA, IgE, etc.) and the composition (their AAs sequence) of the IgG. In this chapter we present various models for representing the structure of IgGs by splitting the compounds into CG beads. Additionally, we define the SRP matrices in relation to the composition of each fragment - that is, its sequence of AAs - using four different approaches.

For clarity, we have defined our own nomenclature: **"(IgGa-IgGb)$_n$-(SRP)$_m$-*ApproachAcronym"*** where **"n"** refers to the number of beads for each IgG, **"m"** is the number of approaches used to define the SRP and **"*ApproachAcronym"*** is the abbreviation for the names of the approaches used, such as QM for Quantum Mechanics.

To answer the question, we did a first attempt named "**(IgGa-IgGb)$_1$-(SRP)$_1$-*Custom"***. Here, IgGs were represented with the simplest CG model, comprising a single CG bead. On the other hand, a customized definition for SRP values was employed (**Figure 4.2).**

(a) Water **(Type W)**

(b) Au NP **(Type Au)**

(c) Immunoglobulins

1 Bead = Σ amino acids

SIMPLE MODEL

IgGa **(Type IgGa)**   IgGb **(Type IgGb)**

SRP	W	Au	IgGa	IgGb
W	25	120	50	50
Au		1	15	15
IgGa			30	80
IgGb				30
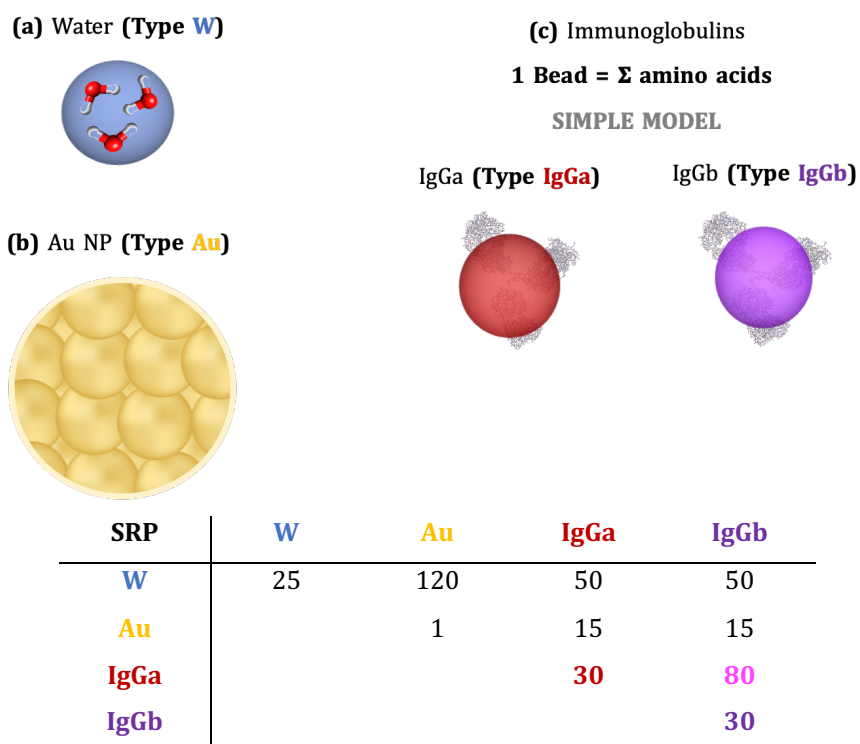
Figure 4.2: Level of CG for the compounds. a) Solvent beads are depicted in blue (type W). b) The Au NP consists of multiple gold beads (type Au), depicted in golden yellow. c) IgGa and IgGb are illustrated in crimson red and bright purple, respectively, each composed by a single type of CG bead. The custom SRP values with units of $\in_0$ for each bead are tabulated below. The crucial SRP values for obtaining Janus distribution are: IgGa/IgGa in crimson red, IgGb/IgGb in bright purple and IgGa/IgGb in magenta.

W/W SRP was maintained to 25 according to Groot and Warren[27] definition. To represent the hydrophobicity and compactivity of the Au NP, we introduced a new bead type with W/Au = 120 and Au/Au = 1. **These values will remain constant in the following sections**. Given that IgGs are composed of AAs of different polarities, the W/IgG SRP was set to 50. To ensure their adsorption onto the surface, the Au/IgG was set to 15.

Theoretically, to obtain Janus distributions, the involved compounds should exhibit contrasting chemical properties (e.g., acid/base, hydrophilic/hydrophobic, etc.)[28]. This leads us to the question: *How can these differences be effectively incorporated in our model?* Our approach was to adjust the SRP in a way that IgGs of the same type (like **IgGa**/**IgGa** or **IgGb**/**IgGb**) interact more favorably with each other than with the different types (**IgGa**/**IgGb**). In essence, the SRP value for **IgGa**/**IgGa** and **IgGb**/**IgGb** must be lower than **IgGa**/**IgGb**. This leads to the next question: *how different should be these values*? To answer this, we conducted simulations with a SRP value of 80 for **IgGa**/**IgGb** while varying the SRP values for **IgGa**/**IgGa** or **IgGb**/**IgGb**, from 5 to 35 with the purpose of analyzing the morphology that they adopt onto Au NP surface.

Ideally, a perfect spherical Janus distribution on the Au NP is achieved when the *c.o.m.* of IgGa, Au NP and IgGb form an angle of 180° (as depicted in **Figure 4.3**).
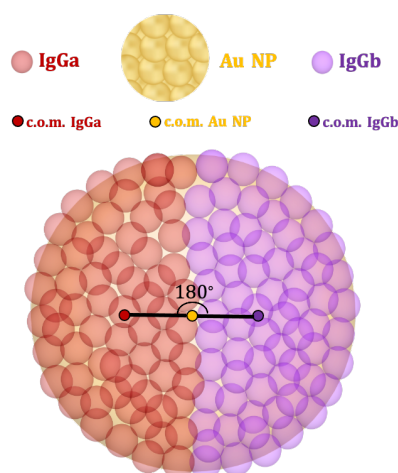
Figure 4.3: Schematic illustration for ideal spherical Janus distribution where all IgGs are adsorbed onto Au NP surface. On the left, IgGa with their respective c.o.m. (point depicted in crimson red). The center golden point denotes the c.o.m. of Au NP. Finally, on the right, all the IgGb with the respective c.o.m. are depicted in bright purple. The angle formed between the c.o.m. of IgGa, Au NP and IgGb, designated as IgGa-Au NP-IgGb is 180°.

The methodology employed was as follow:

1) Simulations were run including an Au NP made up of 5000 beads and 750 beads of each type of IgG randomly distributed along the box.

2) All the IgG beads that were not adsorb onto Au NP surface were removed. This step was important to prevent any deviation in the calculation of the *c.o.m.*

3) The *c.o.m.* was calculated for each set of compounds: *c.o.m.* of IgGa, *c.o.m.* of Au NP and *c.o.m.* of IgGb.

4) Finally, the angle between these three *c.o.m.* was measured.

The distribution of IgG onto Au NP was expected to vary when changing the SRP value for **IgGa**/**IgGa** and **IgGb**/**IgGb**. Keep in mind that as the SRP values increase, the interaction becomes more repulsive, and conversely, as the values decrease, the interaction becomes more attractive. The changes in the angle between the three *c.o.m.* for different SRP values are shown in **Figure 4.4**.
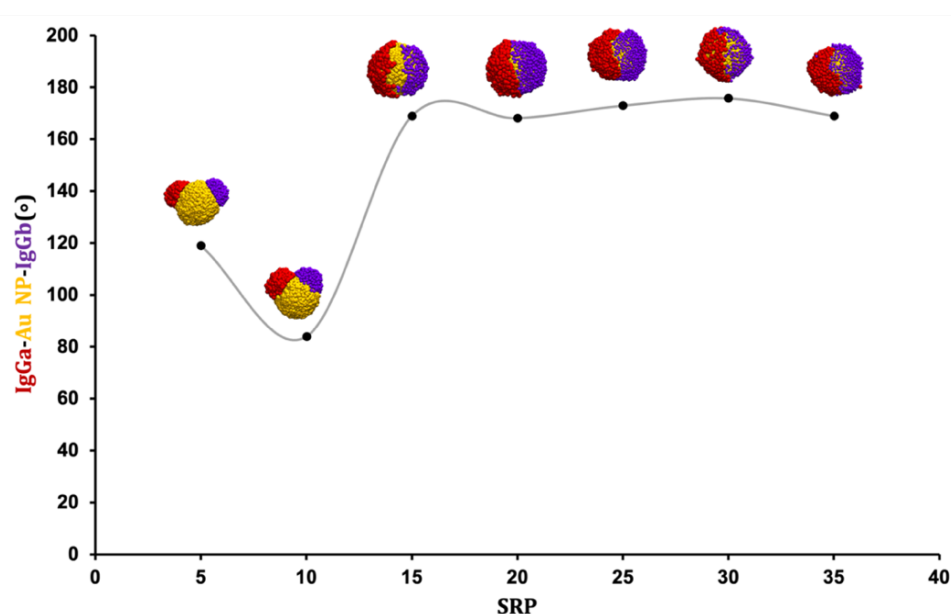
Figure 4.4: Schematic illustration of IgG morphologies onto Au NP surface. Each point shows the angle between the three c.o.m. (IgGa-Au NP-IgGb) for a given IgGa/IgGa and IgGb/IgGb SRP values. Water beads (W) are not shown for sake of clarity.

It is paramount to draw special attention to the fact that IgG can adopt two different architectures onto Au NP surface depending on the SRP values. At lower values of SRP (<15), adopt a "*Mickey mouse*"-like, whereas values ≥15 they are more separated and spherically distributed around the Au NP surface. These results sit alongside Kang and Honciuc experiments[29], who demonstrated that the individual lobes of snowman-shaped Janus particles can be easily and independently tuned in their chemical compositions.

4.2.1 SRP values for a real IgG

As aforementioned, this study was performed in collaboration with Prof. Víctor F. Puntes and Dr. Neus G. Bastús from ICN2. Their interests were to construct bispecific Au NPs using two IgG: the A32 (which recognizes the protein gp120 expressed on the membrane of HIV-infected cells) and the 3G8 (which recognizes one receptor expressed on NK cells). At this point, we focused on the definition of SRP matrices for such IgG considering only their F_{ab} fragment. As said, the main differences of their AA sequences are found within this fragment. The question we must answer was: *how does the F_{ab} of A32 differ from the F_{ab} of 3G8?* Remember that they must present considerable differences to obtain Janus distributions.

This section presents several approaches to define the SRP values for the $\boldsymbol{F_{ab}}$ depending on its AA side chain (R) sequences. **Although we were able to find the full sequence of $\boldsymbol{F_{ab}}$ for both IgGs, A32 and 3G8**[30–32] (included in **Appendix C4-A**: $\boldsymbol{F_{ab}}$ sequences for A32 and 3G8)**, we were unable to locate the $\boldsymbol{F_c}$ sequence for 3G8. Given that immunoglobulins of the same class, such as IgG, typically share the same $\boldsymbol{F_c}$ sequence, we decided to use the A32's $\boldsymbol{F_c}$ for both IgGs.**

The goal was twofold. On one hand, we aimed to calculate the number of AAs for each CG bead (A32 and 3G8). On the other hand, the contribution of all AAs was considered to build the SRP matrix. **It is worth noting that we only considered the side chains (R) of the AAs to perform all the calculations.** We made this decision because the peptide bonds, which form the protein's backbone, are relatively conserved, providing little variances between such IgGs.

This is time to remember that W/W, W/Au and Au/Au (25, 120 and 1, respectively) will remain constant up till the end. As previously discussed, these SRP values were fixed to represent the thermodynamic properties of water and the hydrophobicity and compactness of the Au NP. Thus, we focused on the derivation of W/A32, W/3G8, Au/A32, Au/3G8, A32/A32, A32/3G8 and 3G8/3G8 SRP values. On the grounds of the method explained before, we need ensure that:

- IgG prefer to be attached onto the Au NP surface rather than remaining freely dispersed in solution. As a result, Au/A32 and Au/3G8 must be lower (indicating stronger attraction) than those for W/A32 and W/3G8.

- **A32**/**A32** and **3G8**/**3G8** should be significantly lower than **A32**/**3G8**. Otherwise, IgGs would be randomly distributed onto the Au NP without exhibiting Janus distributions.

4.2.1.1. "(A32-3G8)1-(SRP)1-QM". In line with **Chapter 3**, the SRP for the first approach were derived from QM calculations following these steps:

- Step 1: the binding energies ($\Delta E_{binding}$) (Eq. 2.15 from Chapter 2) between all AAs' side chains with W, Au and themselves were obtained by Gaussian16 software package[33]. Geometrical optimizations were carried out using the Minnesota M06-2X functional[34] and with LANL2DZ basis[35–38]. The effect of solvent (W) was modelled using a continuum model of water, applying the integral equation formalism SMD[39].

- Step 2: The values obtained in Step 1 were linearly correlated with the SRP values. Like polymers, AAs have an R group with different polarities, influencing how they interact with other compounds. As such, we based our relationship with Flory-Huggins theory. For doing so, the lowest and the highest values were fixed to 5 (less repulsive) and 120 (more repulsive), respectively. Figure 4.5 presents an example of the regression obtained between Au and the R of A32 beads.
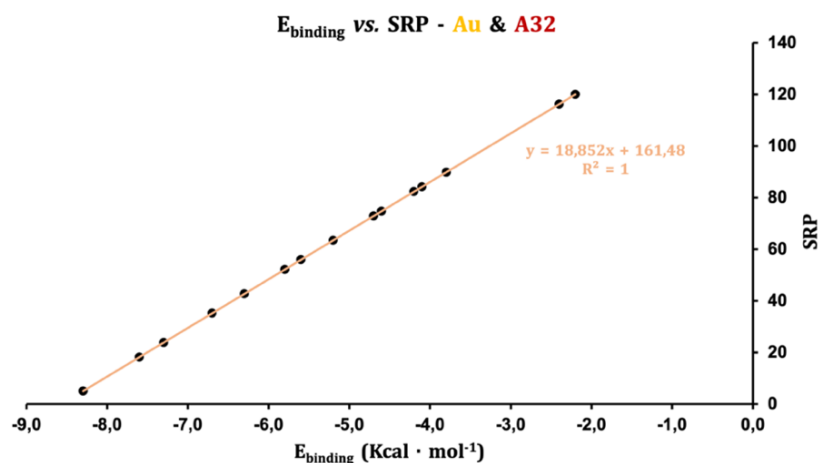

Figure 4.5: Linear regression plot between the binding energies ($E_{binding}$) vs. SRP for Au and A32. The lowest value (-8.3,5) corresponds to Au-Methionine interaction while the highest one (-2.2,120) to Au-Glycine.

- Step 3: Boltzmann distributions were applied to the results of Step 1. This was done for two main reasons: to provide an indication of the most representative interaction and to take into account the varying quantities of different AAs in the sequences of each IgG.

- Step 4: the "mole fraction" obtained from Step 3 was then multiplied by the corresponding SRP value determined in Step 2.

- Final step: the sum of the values obtained in Step 4 gave us the individual interaction between the considered beads. An example of the calculations for **Au**/**A32** is shown in **Table 4.2**.

Table 4.2: $\Delta E_{binding}$, SRP, mole fraction and the final value of SRP for Au/A32. Each column but the interaction is associated to the previous steps from (1) to (4).

Interaction	Number of AAs	(1) $E_{binding}$ (Kcal/mol)	(2) SRP	(3) "Mole fraction"	(4) SRP x Mole fraction
Au/Gly	74	-2.2	120.01	1.40E-04	0.02
Au/Ala	52	-2.4	116.24	1.38E-04	0.02
Au/Val	76	-3.8	89.84	2.15E-03	0.19
Au/Ile	24	-2.4	116.24	6.38E-05	0.01
Au/Leu	58	-3.8	89.84	1.64E-03	0.15
Au/Phe	20	-6.3	42.71	3.84E-02	1.64
Au/Trp	18	-7.6	18.20	3.10E-01	5.65
Au/Met	0	-8.3	5.01	0.00	0.00
Au/Pro	54	-4.2	82.30	3.00E-03	0.25
Au/Ser	136	-4.1	84.19	6.37E-03	0.54
Au/Thr	84	-4.7	72.87	1.08E-02	0.79
Au/Tyr	16	-7.3	23.86	4.36E-01	10.41
Au/Asn	42	-5.6	55.91	2.12E-02	1.19
Au/Gln	36	-5.2	63.45	1.26E-02	0.80
Au/Cys	42	-6.7	35.17	6.04E-02	2.12
Au/His	20	-6.3	42.71	3.84E-02	1.64
Au/Arg	48	-5.8	52.14	1.32E-02	0.69
Au/Lys	16	-5.8	52.14	3.96E-02	2.07
Au/Asp	26	-4.7	72.88	2.58E-03	0.19
Au/Glu	20	-4.6	74.76	2.83E-03	0.21
TOTAL	862	-	-	1.00	**28.55**

As outlined, **Table 4.2** feeds us with information as to what is the most representative interaction when considering Boltzmann distributions. It stands the reason that not only are the $\Delta E_{binding}$ are the most important parameters but also the number of existing interactions between CG beads. Proof hereof is the interaction between Au and Met. Even though they have the lowest $\Delta E_{binding}$, the contribution to the final SRP is null.

The same procedure was followed to define the final matrix (**Table 4.3).**

Table 4.3: SRP values based on QM calculations.

SRP	W	Au	A32	3G8
W	25	120	12	11
Au		1	29	21
A32			12	10
3G8				8

According to the matrix, the SRP values for **W**/**A32** and **W**/**3G8** are lower than those for **Au**/**A32** and **Au**/**3G8**, implying that these IgG are more inclined to interact with W beads than to adsorb onto Au NP surface. To verify this, we calculated the radial distribution (g(r)) and the integration for Au, A32 and 3G8 (**Figure 4.6**). In this context, the g(r) provides information about the density of Au at a given radius from the Au NP *c.o.m.* while the integration indicates the number of beads expected at certain distances (r) from the *c.o.m.* of the Au NP.
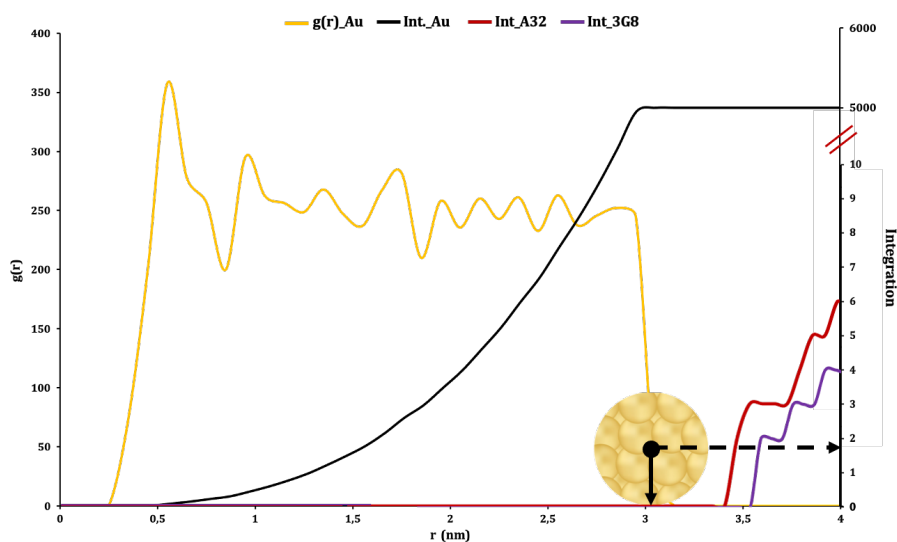

Figure 4.6: Graphic of g(r) and integration for Au (black line), A32 (red line) and 3G8 (purple line).

As seen in **Figure 4.6**, the distance from the *c.o.m.* of the Au NP to its surface is approximately 3 nm, as shown by the g(r)_Au. This suggests an overall size of about 6 nm for the Au NP. Further to this, there are no doubts whatsoever that a small number of IgG are adsorbed onto Au NP surface, indicating that most of them are freely distributed in solution. Following the discontinuous black line one can see that only 1 or 2 IgG of each type are found onto the Au NP. As the distance from the surface increases, the number of IgG keep on mushrooming.

This analysis also confirms that no Janus distributions were obtained. Firstly, the IgG were not attached to Au NP surface. Secondly, even if they were adsorbed to the surface, they would be randomly distributed along the surface since SRP values for **A32**/**A32 3G8**/**3G8** and **A32**/**3G8** are roughly equivalent.

4.2.1.2. "(A32-3G8)1-(SRP)1-BS". The second approach closely follows the methodology developed by Prof. Berend Smit's (hereinafter named as BS) group[40], which defines the parameters based on the hydrophilicity and hydrophobicity of proteins and lipids. We aimed to test its applicability to our system.

Initially, we categorized AAs based on the properties of their R. It is crucial to note that AAs can be classified in multiple ways and sometimes, the classification can be ambiguous[41]. To address this, we initially divided the AAs in three groups, according to whether the functional group on the R is nonpolar (ØP), polar (P) or electrically charged (E) at about pH 7. In this classification, we assumed that AAs with R primarily composed of hydrocarbon chains were ØP, those capable of forming hydrogen bonds were P, and those exhibiting acidic or basic behaviors were considered E (**Table 4.4**). Later in this chapter, we used a five-type classification, based on hydropathy indexes[42] (section **4.5**).

Table 4.4: Classification of AAs according to the R polarity.

R Polarity	R structure	Amino acid name	3 Letter code	1 Letter code
Non-polar (ØP)	—H	Glycine	Gly	G
	—CH₃	Alanine	Ala	A
	—HC(CH₃)(CH₃)	Valine	Val	V
	—HC–CH₃ / CH₂ / CH₃	Isoleucine	Ile	I
	—H₂C–HC(CH₃)(CH₃)	Leucine	Leu	L
	—CH₂–⬡	Phenylalanine	Phe	F
	—CH₂–(indole)	Tryptophan	Trp	W
	—H₂C–H₂C–S–CH₃	Methionine	Met	M
	(proline ring)	Proline	Pro	P
Polar (P)	—H₂C–OH	Serine	Ser	S
	—HC–OH / CH₃	Threonine	Thr	T
	—CH₂–⬡–OH	Tyrosine	Tyr	Y
	—H₂C–C(O)–NH₂	Asparagine	Asn	N
	—H₂C–H₂C–C(O)–NH₂	Glutamine	Gln	Q
	—H₂C–SH	Cysteine	Cys	C
Electrically charged (E)	(imidazolium ring) —H₂C–C=CH	*Histidine	His	H
	—H₂C–H₂C–H₂C–NH–C–NH₂ / NH₂⁺	Arginine	Arg	R
	—H₂C–H₂C–H₂C–H₂C–NH₃⁺	Lysine	Lys	K
	—H₂C–COO⁻	Aspartate	Asp	D
	—H₂C–H₂C–COO⁻	Glutamate	Glu	E

*NOTE: Although histidine is partially charged at pH 7, we have considered it fully charged.

Next, we build an initial matrix under the assumption that each IgG CG bead contained a 100% of each amino acid group (**Table 4.5**). We referred to this as the "pre-matrix".

Table 4.5: "Pre-matrix" of SRP values between **W**, **Au**, **ØP**, **P** and **E** expressed in units of $\in_0$.

SRP	W	Au	ØP	P	E
W	25	120	120	15	5
Au		1	80	35	25
ØP			25	80	80
P				35	35
E					50

In this model, we applied basic parameterization for most of the interactions. Thus, **W**/**ØP**, **W**/**P**, **ØP**/**ØP**, **ØP**/**P**, **P**/**P** were defined similarly to the parameters for hydrophobic (ØP) and hydrophilic (P) beads from BS studies[40] (see **Chapter 2**). For **W**/**E**, **ØP**/**E**, **P**/**E** and **E**/**E** the effect of charges was considered. Keep in mind that E contains both attractive and repulsive forces between AAs with the same and opposite charges. We used smaller SRP values for interacting beads that are more attractive than **W**/**W**, such as **W**/**E** due to the formation of stronger hydrogen bonds. On the contrary, the more repulsive the interaction between beads, the higher the SRP values, such as **ØP**/**E** or **E**/**E**. For interactions involving metallic beads (Au) we set the values based on whether their interaction with each group of AAs was weaker or stronger. Several studies have shown that the interaction of Au NPs with charged ligands prevents the Au NPs aggregation in aqueous solutions[43]. Hence, **Au**/**E** was more attractive than **Au**/**P** and **Au**/**ØP**.

As said, the "pre-matrix" from **Table 4.5** assumes that IgG CG beads contained a 100% of each AA group (ØP, P and E). However, this was not the case because each IgG bead was defined by the contributions of all AA groups (**Figure 4.7**).
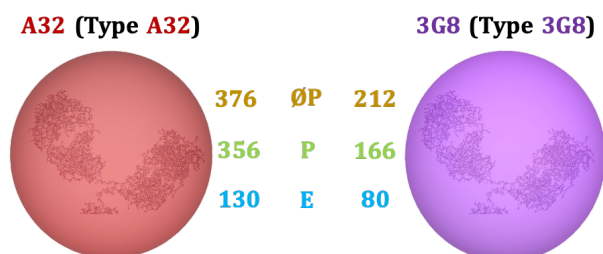

A32 (Type A32)   **3G8 (Type 3G8)**

376   ØP   212
356   P   166
130   E   80

Figure 4.7: Number of AA groups found for each IgG CG bead.

The question arises: *how should we consider such contributions?* We calculated the molar faction of the AAs. Then, this resultant value was multiplied by its corresponding value that we had assigned in the "pre-matrix. To clarify this process, let us use an example:

(A) PREMATRIX:

SRP	ØP	P	E
W	120	15	5

(B) AA GROUPS MOLAR FRACTION:
(**Ex: ØP**/ΣAA = 376/862=0.4361)

Molar Fraction	ØP	P	E	Total
W/A32	0.4361	0.4129	0.1508	1

(C) SRP VALUE FOR W/A32:

Final SRP	A32
W	= (120 x 0.436) + (15 x 0.412) + (5 x 0.150)

The final matrix is collected in **Table 4.6.**

Table 4.6: SRP values based on BS studies. Color code for the relevant values: crimson red for A32/A32, bright purple for 3G8/3G8 and magenta for A32/3G8.

SRP	W	Au	A32	3G8
W	25	120	59	62
Au		1	53	54
A32			49	56
3G8				49

The highlighted values from **Table 4.6** bring evidence that the derivation of SRP values following the BS[40] approach will not yield Janus distributions, as **A32**/**A32** = **3G8**/**3G8** ~ **A32**/**3G8**. Unlike the first approach (**section 4.2.1.1**), the **W**/**A32** and **W**/**3G8** were found to be more repulsive, leading them to be attached onto the Au NP surface. This provides further evidence that when SRP values are similar, there is no preference for the compounds to interact with one compound or another. Moreover, given that the number of W beads in the system is higher than that of Au, the attachment to the Au NP emerges as a mechanism to minimize their contact with W. **Figure 4.7** provides a snapshot of the simulation.
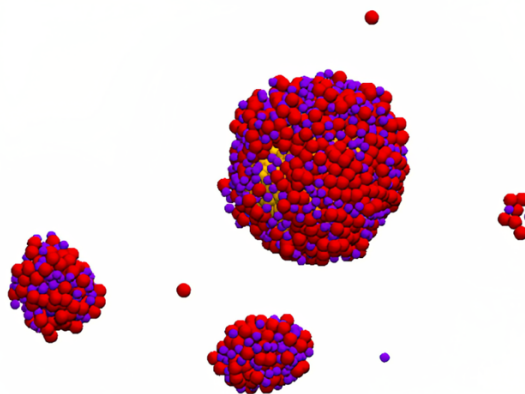
Figure 4.7: Snapshot of Au NP with A32 and 3G8 using BS approach. For sake of clarity, water beads are removed.

Briefly, as initially stated in this section, IgG must exhibit distinctive properties to enable the formation of spherical Janus distributions onto the Au NP surface. While the derived matrix indicates higher values for **A32**/**3G8** compared to **A32**/**A32** or **3G8**/**3G8**, these differences are not substantial enough. As seen in **Figure 4.**7, IgGs are irregularly distributed along the Au NP surface.

4.2.1.3. "(A32-3G8)1-(SRP)2-QM BS". The last attempt was a hybrid approach, combining elements of both the QM and the BS methodology. For this, QM were used to derive the SRP for interactions involving Au, while the behavior of A32 and 3G8 was described by BS approach. **Table 4.7** gathers the values from the combine approaches.

Table 4.7: SRP values derived from QM and BS approaches.

SRP	W	Au	A32	3G8
W	25	120	59	62
Au		1	29	21
A32			49	56
3G8				49

As expected, the results did not shown improvements. However, we assumed that this approach was the best to monitor both the metallic and protein behaviors. **Thus, we decided to use this SRP values definition for the following sections.**

While single bead models allow a significant computer time saving and relatively straightforward model implementation, they present disadvantages. Before all else, the definition of SRP for a single-type bead poses a problem in CG models. On the face of it, a prior knowledge of the system is necessary to preserve the essential features. Yet, on the other side of the coin, several effects different in nature must be included to produce accurate and transferable models. Therefore, a less CG model was design considering the Y-like shape of IgGs.

4.3. "Less is more"

The less CG applied is shown in **Figure 4.8** and some remarks must be mentioned:

- We decided to increase the complexity of the IgG models, making them composed of four beads: one representing each F_{ab} and the other two symbolizing the F_c region. With an increase in the number of beads representing each IgG, the size of the Au NP was correspondingly increased.

- The F_c AAs composition for both IgG was: **42%, 33%** and **25%** for **ØP**, **P** and **E**, respectively. Find the sequences of the F_c for A32 and 3G8 in the **Appendix C4-B**: F_c sequences for A32.

- A new column was incorporated into the SRP matrix for defining the interactions involving this F_c.
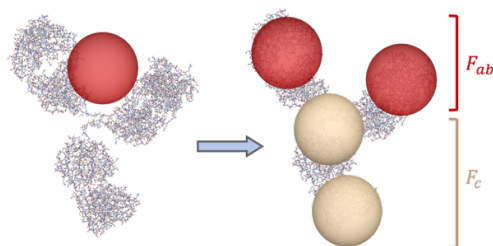

Figure 4.8: Y-like shape of IgG. In the less CG model, IgG is represented by four beads: the crimson red beads represent each F_{ab} while the two sanded-colored beads represent the F_c.

Every time you add a new bead into the system, the description of the local interactions within a protein needs to be increased. The fact of using a less CG model served dual purposes: firstly, to determine if Janus distribution can be achieved, and secondly, it provides insight into whether specific fragments (F_c or F_{ab}) exhibit a preference for adsorption onto the Au surface.

Several studies have demonstrated that antibodies can interact with Au providing stability in colloidal solutions. This adsorption to Au NP can be mediated either with covalent or non-covalent immobilization methods[44–46]. While the first one, involves the use of mediator linkers, which directly bind the antibodies to the Au NP surface via thiol group-containing molecules or through the complexation of streptavidin and biotin, the second method is described as spontaneous, where antibodies mainly attach to the Au NPs due to hydrophobic and ionic interactions[47,48]. Considering that covalent immobilization requires pre-modification of the species and in light of our interests –which include determining whether if F_c or F_{ab} exhibit preference onto Au NP surface- we used the non-covalent method.

As said in **section 4.2.1.3**, the approach used to define the SRP values will be the one that combines QM with BS: "(IgGa-IgGb)4-(SRP)2-QM_BS". **Figure 4.9** presents the final matrix that includes the new parameters for the F_c bead, alongside a snapshot for the last frame of the simulation. Keep in mind that the F_c is the same for both IgGs.

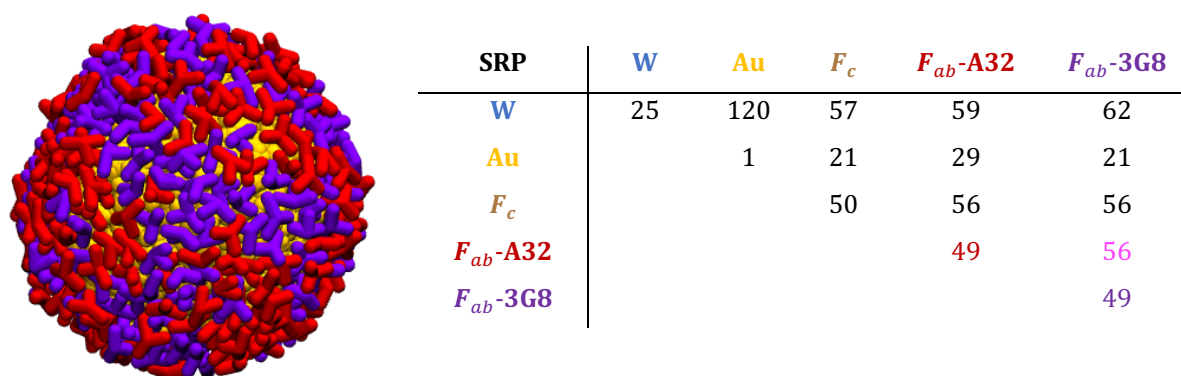| SRP	W	Au	F_c	F_{ab}-A32	F_{ab}-3G8
W	25	120	57	59	62
Au		1	21	29	21
F_c			50	56	56
F_{ab}-A32				49	56
F_{ab}-3G8					49

Figure 4.9: **A snapshot for the final frame of the simulation is shown on the left. For sake of clarity, water beads are removed and IgGs are depicted in crimson red for the A32 and bright purple for the 3G8. SRP matrix obtained when adding the new F_c bead (on the right).**

It is worth noting that in **Figure 4.9**, the IgGs form patches onto Au NP surface. During the simulation, once the IgG were attached to the surface, they begin to reorganize themselves along the Au NP. Furthermore, results suggest that F_c or F_{ab} have the same probability to be adsorbed onto Au NP surface, as indicated by **Au**/F_c ∼ **Au**/F_{ab}-**A32** ∼ **Au**/F_{ab}-**3G8**. This fact greatly affects the antigen-binding capacity because of the random orientation of antibodies that make F_{ab} to be less accessible.

4.4. Effect of changes in the percentage of AAs

Up to this point, the distributions of IgG around the surface of Au NP have been examined using different approaches and CG models. However, no spherical Janus distributions have been achieved. Quantitatively speaking, both IgGs have similar polarities, indicating that they do not possess the favorable properties required for separation into two distinct sides. This raises the question: *how can we alter these properties to achieve Janus distributions?* The answer lied in modifying the AA sequences of the IgG to see if this results in more significant differences in the SRP values. Since the F_c was identical in both IgGs, modifications were only made to the $\boldsymbol{F_{ab}}$.
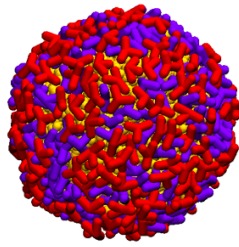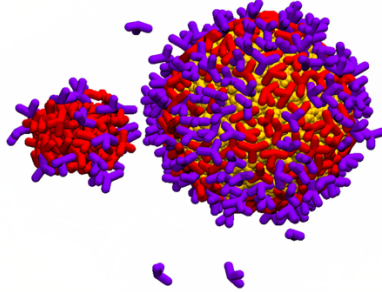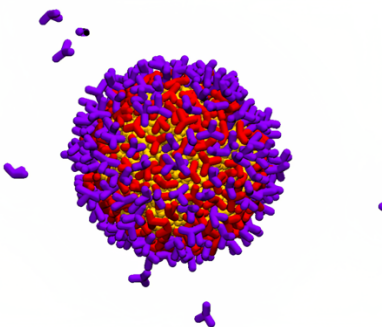
Before proceeding, let us start enunciating the assumptions needed to deduce the SRP values:

1) The CG applied was the one formed by 4 CG beads (Y-like shape from **Figure 4.7**).

2) The SRP values were deduced by the third approach: <u>"(A32-3G8)₄-(SRP)₂-QM BS"</u>**.** It is important to remember that QM calculations were used to derive the parameters related to the metallic nature, while BS considered the hydrophilic and hydrophobic properties of the other compounds.

3) The AAs were classified as ØP, P or E, as shown in **Table 4.4**.

4.4.1 Changing the percentages of AAs for F_{ab}-3G8: mod-F_{ab}-3G8

To get started, we only altered the composition of the F_{ab}-3G8. From clarity, we henceforth to it as mod-F_{ab}-3G8. Both the F_c or the F_{ab}-A32 remained constant in all cases. We assumed that mod-F_{ab}-3G8 was formed entirely of either ØP, P or E. The final SRP valued for mod-F_{ab}-3G8 and snapshots for each simulation are shown in **Table 4.8**

Table 4.8: mod-F_{ab}-3G8 composition, SRP values and snapshot from the three simulations. For sake of clarity, water beads have been removed.

mod-F_{ab}-3G8 composition	SRP for mod-F_{ab}-3G8		Snapshot
100% ØP	**SRP**	**mod-F_{ab}-3G8**	
	W	120	
	Au	9	
	F_c	57	
	F_{ab}-A32	56	
	mod-F_{ab}-3G8	25	
100% P	**SRP**	**mod-F_{ab}-3G8**	
	W	15	
	Au	29	
	F_c	54	
	F_{ab}-A32	55	
	mod-F_{ab}-3G8	35	
100% E	**SRP**	**mod-F_{ab}-3G8**	
	W	5	
	Au	49	
	F_c	58	
	F_{ab}-A32	57	
	mod-F_{ab}-3G8	50	

Although Janus distributions were not observed in any case, several insights into the behavior of mod-F_{ab}-3G8 IgG can be derived:

- All mod-F_{ab}-3G8 IgG are adsorbed onto the Au NP surface when they have poor interactions with W (Snapshot for 100% ØP). This suggest that mod-F_{ab}-3G8 has a strong affinity for the Au NP (Au/mod-F_{ab}-3G8 =9), causing them to bind to it rather than remaining freely dispersed in solution. In contrast, when they have a stronger interaction with W (W/mod-F_{ab}-3G8 =15 or 5) they appear to be freely dispersed in solution or oriented towards to W (snapshots for 100% P and E).

- The orientation that they adopt onto Au NP surface also depends on their interaction with W and Au. When mod-F_{ab}-3G8 is composed entirely of ØP, they prefer to stretch out towards the surface of the Au NP to maximize their contact on Au NP, as **Au**/**mod-F_{ab}-3G8** =9. By adopting this position, they also minimize their interaction with W (**W**/**mod-F_{ab}-3G8** =120). However, when they are entirely composed of P or E, they orient perpendicular to the surface to maximize their interaction with W, which is more attractive than for Au.

- Small differences but significant, can be seen regarding to **mod-F_{ab}-3G8**/**mod-F_{ab}-3G8** SRP values. We evaluated the g(r) and the integral among the mod-F_{ab}-3G8 immunoglobulins in order to assess how the SRP values for **mod-F_{ab}-3G8**/**mod-F_{ab}-3G8** influences their aggregation (**Figure 4.10**).
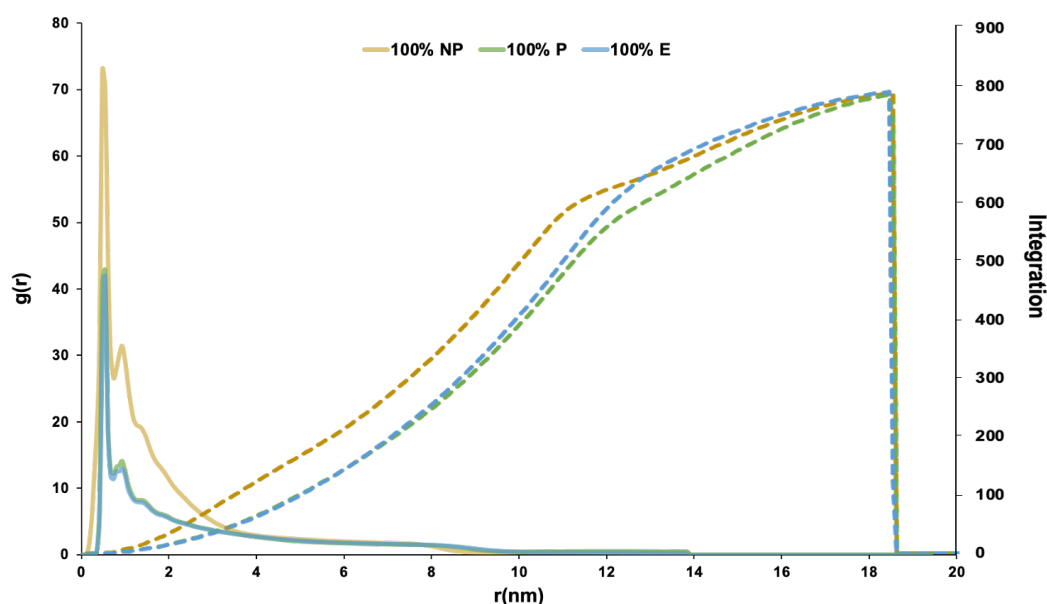
Figure 4.10: Graphic of g(r) and integral for mod-3G8/mod-3G8 when mod-F_{ab}-3G8 is entirely composed by ØP, P or E.

As outlined, the relationship between lower SRP and molecular proximity is inherently interconnected. As the level of attraction increases, molecular are drawn closer together and *vice versa.* Accordingly, when the SRP is 25 (**mod-F_{ab}-3G8** /**mod-F_{ab}-3G8** for entirely ØP) mod-F_{ab}-3G8 tend to be into closer proximity. That is why, the probability to find other mod-F_{ab}-3G8 molecules at any distance is higher at distances lower than 13 nm. Conversely, when the attraction decreases (**mod-F_{ab}-3G8** /**mod-F_{ab}-3G8** for entirely P or E), molecules tend to move further apart, resulting in a lower number of molecules closer at short distances.

It is important to emphasize that the considering all values, whether if they are repulsive or attractive, is crucial in the simulation. By acknowledging the contribution of all values within a system, comprehensive understanding can be achieved. This emphasizes the importance of a holistic perspective in simulations, which enables a more nuanced analysis and a better grasp of the underlying mechanisms governing the system.

4.4.2 Changing the percentages of AAs for both IgG

The last attempt involved altering the properties of both F_{ab}, with a specific focus on changing their polarities. This decision stemmed from the recognition of the fact that the formation of spherical Janus distributions often occurs when compounds possess distinct properties. Therefore, the aim was to induce the desired outcome of obtaining spherical Janus distributions.

All the tested combinations are summarized in **Table 4.9**. A simple nomenclature was defined to identify each simulation: **mod-A32_X-mod-3G8_Y** where "*X*" stands for the composition of **mod-F_{ab}-A32** and "*Y*" for **mod-F_{ab}-3G8**.

Table 4.9: Number of simulations, composition for the mod-F_{ab}-A32 (X) and mod-F_{ab}-3G8 (Y). and the name for each simulation.

Simulation number	X	Y	Simulation name
1	E	ØP	mod-A32_E-mod-3G8_ØP
2	ØP	E	mod-A32_ØP-mod-3G8_E
3	P	ØP	mod-A32_P-mod-3G8_ØP

The SRP matrices for all simulations were calculated (**Appendix C4-C**: SRP values for 4.4.2 simulations) and the most representative matrix was obtained for simulation 3 (**Table 4.10**).

Table 4.10: SRP matrix for simulation 3.

SRP	W	Au	F_c	mod-F_{ab}-A32	mod-F_{ab}-3G8
W	25	120	57	15	120
Au		1	21	29	9
F_c			50	54	57
mod-F_{ab}-**A32**				35	80
mod-F_{ab}-**3G8**					25

Table 4.10 revealed intriguing trends in our SRP values. Notably, SRP values for **mod-F_{ab}-A32**/**mod-F_{ab}-A32** and **mod-F_{ab}-3G8** /**mod-F_{ab}-3G8** demonstrated to be more favorable than **mod-F_{ab}-A32** /**mod-F_{ab}-3G8**. However, simulations did not show Janus distributions (**Figure 4.11**).
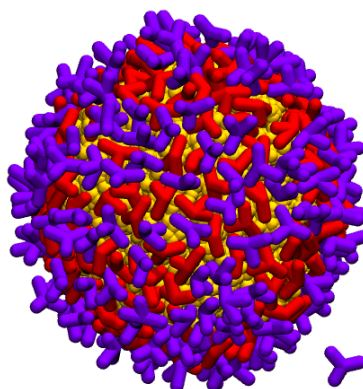

Figure 4.11: Snapshot from Simulation 3.

Based on our results we can draw several conclusions:

1) Introducing additional SRP values to the matrix amplifies the complexity of the interactions among the beads involved.

2) While interactions between identical IgGs, such as **mod-F_{ab}-A32**/**mod-F_{ab}-A32**, generally display greater interactions than **mod-F_{ab}-A32** /**mod-F_{ab}-3G8**, it is crucial not to overlook the other interactions. An illustration of this is the **W**/**mod-F_{ab}-A32** which is more attractive than **mod-F_{ab}-A32**/**mod-F_{ab}-**A32. And therefore, **mod-F_{ab}-A32** would prefer to interact with W rather than with itself.

3) Despite that, we believe that extending the simulation time, the IgGs would end up reorganizing to form Janus distributions.

4.5. Effect of the change in the classification of AAs

As previously mentioned, AAs can be classified in several ways[41]. The aim of the current section was to investigate the alleged dependency of the AAs classification on SRP values. In this case, AAs were classified according to their hydropathy indexes (HI), as defined by Kyte & Doolittle[42]. For clarity, the HI is a numerical value assigned to each AA, reflecting the relative hydrophilicity or hydrophobicity of its R.

Table 4.11: Hydropathy indexes for the R of AAs. Values are listed from the most hydrophobic tendency (Isoleucine) to the less one (Arginine).

R	Hydropathy Index
Isoleucine	4.5
Valine	4.2
Leucine	3.8
Phenylalanine	2.8
Cysteine	2.5
Methionine	1.9
Alanine	1.8
Glycine	-0.4
Threonine	-0.7
Serine	-0.8
Tryptophan	-0.9
Tyrosine	-1.3
Proline	-1.6
Histidine	-3.2
Glutamate	-3.5
Glutamine	
Aspartate	
Asparagine	
Lysine	-3.9
Arginine	-4.5

According to the tendency of the values collected in **Table 4.11** we divided the AAs into three groups, from the most **hydrophobic** (depicted in cantaloupe) to the most **hydrophilic** (depicted in sky blue). Given the redistribution of AAs into different groups, we expected some changes in the SRP matrix between W/F_c, W/F_{ab}-**A32** and W/F_{ab}-**3G8** and F_c/F_c, F_c/F_{ab}-**A32** and F_c/F_{ab}-**3G8**, F_{ab}-**A32**/F_{ab}-**A32**, F_{ab}-**A32**/F_{ab}-**3G8** and F_{ab}-**3G8**/F_{ab}-**3G8**.

The procedure followed for determining the final SRP matrix (**Table 4.12**) combined three methods: **HI** to examine the interactions involving W, QM to investigates the ones involving Au, and BS to assess the interactions between IgGs. Detailed information regarding all the calculations performed in this section can be found in **Appendix C4-D**: Detailed calculations for 4.5 simulations.

Table 4.12: SRP values according to hydropathy indexes.

SRP	W	Au	F_c	F_{ab}-A32	F_{ab}-3G8
W	25	120	13	14	13
Au		1	21	29	21
F_c			50	54	55
F_{ab}-A32				49	54
F_{ab}-3G8					50

Referring to the SRP values in **Table 4.12**, one cannot deny that IgGs interact more favorably with W than with other compounds. Even though some IgGs were attached onto Au NP surface, Janus distributions were not achieved. Please, find the final image of the simulation in **Appendix C4-E**: Final structure obtained using the HI.

4.6. Conclusions

To the best of our knowledge, this is the first study that explores the formation of spherical Janus distributions onto Au NPs using A32 and 3G8 immunoglobulins employing DPD.

Implementing a complex model (4 beads instead of 1 bead) adds a layer of complexity to calculations, as more SRP needs to be defined and considered. Nonetheless, this model offers a more intricate understanding of the ongoing interactions.

Despite our rigorous approaches and various classification of AAs, we were unable to obtain spherical Janus distributions with the compounds involved, in agreement with the experimental results obtained from Prof. Víctor F. Puntes' group.

In summary, this chapter mapped out the differences between simple and complex CG models as well as the use of different approaches to define the SRP values. The general conclusion that can be drawn from the theoretical calculations is that immunoglobulins should be adsorbed to Au NPs surface and present different properties to be Janus distributed.

4.7. Highlights of the chapter

This section contains the most important highlights described in this chapter:

- Presented simple and complex CG models to study only the F_{ab} or the full structure (F_{ab} and F_c) for IgG.

- Defined the proper SRP values to consider the metallic core and proteins behaviors.

- Change the properties of initial IgG to see if the polarities can affect to the obtention of Janus distributions.

- Derived the SRP values for W and IgG according to hydropathy indexes.

4.8. References

(1)   Astorga-Gamaza, A.; Vitali, M.; Borrajo, M. L.; Suárez-López, R.; Jaime, C.; Bastus, N.; Serra-Peinado, C.; Luque-Ballesteros, L.; Blanch-Lombarte, O.; Prado, J. G.; Lorente, J.; Pumarola, F.; Pellicer, M.; Falcó, V.; Genescà, M.; Puntes, V.; Buzon, M. J. Antibody Cooperative Adsorption onto AuNPs and Its Exploitation to Force Natural Killer Cells to Kill HIV-Infected T Cells. *Nano Today* **2021**, *36,* 101056.

(2)   de Gennes P.-G. Soft Matter *Ang. Chem.* **1992**, *31* (7), 842-845.

(3)   Casagrande, C.; Fabre, P.; Raphael, E.; Veyssie, M. "Janus Beads": Realization and Behaviour at Water/Oil Interfaces. *Europhys. Lett.* **1989**, *9* (3), 251-255.

(4)   Safaie, N.; Ferrier, R. C. Janus Nanoparticle Synthesis: Overview, Recent Developments, and Applications. *J. Appl. Phys.* **2020**, *127,* 170902.

(5)   Yang, T.; Wei, L.; Jing, L.; Liang, J.; Zhang, X.; Tang, M.; Monteiro, M. J.; Chen, Y. (Ian); Wang, Y.; Gu, S.; Zhao, D.; Yang, H.; Liu, J.; Lu, G. Q. M. Dumbbell-Shaped Bi-component Mesoporous Janus Solid Nanoparticles for Biphasic Interface Catalysis. *Angewandte Chemie International Edition* **2017**, *56* (29), 8459–8463.

(6)   Yoshida, M.; Lahann, J. Smart Nanomaterials. *ACS Nano* **2008**, *2* (6), 1101–1107.

(7)   Iqbal, M. Z.; Ren, W.; Saeed, M.; Chen, T.; Ma, X.; Yu, X.; Zhang, J.; Zhang, L.; Li, A.; Wu, A. A Facile Fabrication Route for Binary Transition Metal Oxide-Based Janus Nanoparticles for Cancer Theranostic Applications. *Nano Res.* **2018**, *11* (10), 5735–5750.

(8)   Li, X.; Zhou, L.; Wei, Y.; El-Toni, A. M.; Zhang, F.; Zhao, D. Anisotropic Growth-Induced Synthesis of Dual-Compartment Janus Mesoporous Silica Nanoparticles for Bimodal Triggered Drugs Delivery. *J. Am. Chem. Soc.* **2014**, *136* (42), 15086–15092.

(9)   Pradhan, S.; Ghosh, D.; Chen, S. Janus Nanostructures Based on Au−TiO $_2$ Heterodimers and Their Photocatalytic Activity in the Oxidation of Methanol. *ACS Appl. Mater. Interfaces* **2009**, *1* (9), 2060–2065.

(10) Yan, J.; Chaudhary, K.; Chul Bae, S.; Lewis, J. A.; Granick, S. Colloidal Ribbons and Rings from Janus Magnetic Rods. *Nat. Commun.* **2013**, *4* (1), 1516.

(11) Chen, Y.; Liang, F.; Yang, H.; Zhang, C.; Wang, Q.; Qu, X.; Li, J.; Cai, Y.; Qiu, D.; Yang, Z. Janus Nanosheets of Polymer–Inorganic Layered Composites. *Macromolec.* **2012**, *45* (3), 1460–1467.

(12) Poggi, E.; Gohy, J.-F. Janus Particles: From Synthesis to Application. *Colloid Polym. Sci.* **2017**, *295* (11), 2083–2108.

(13) Walther, A.; Müller, A. H. E. Janus Particles: Synthesis, Self-Assembly, Physical Properties, and Applications. *Chem.Rev*. **2013**, *113* (7),5194–5261.

(14) Buttress, J. P.; Day, D. P.; Courtney, J. M.; Lawrence, E. J.; Hughes, D. L.; Blagg, R. J.; Crossley, A.; Matthews, S. E.; Redshaw, C.; Bulman Page, P. C.; Wildgoose, G. G. "Janus" Calixarenes: Double-Sided Molecular Linkers for Facile, Multianchor Point, Multifunctional, Surface Modification. *Langmuir* **2016**, *32* (31), 7806–7813.

(15) Canepa, E.; Salassi, S.; de Marco, A. L.; Lambruschini, C.; Odino, D.; Bochicchio, D.; Canepa, F.; Canale, C.; Dante, S.; Brescia, R.; Stellacci, F.; Rossi, G.; Relini, A. Amphiphilic Gold Nanoparticles Perturb Phase Separation in Multidomain Lipid Membranes. *Nanoscale* **2020**, *12* (38), 19746–19759.

(16) Rasch, M. R.; Rossinyol, E.; Hueso, J. L.; Goodfellow, B. W.; Arbiol, J.; Korgel, B. A. Hydrophobic Gold Nanoparticle Self-Assembly with Phosphatidylcholine Lipid: Membrane-Loaded and Janus Vesicles. *Nano Lett.* **2010**, *10* (9), 3733–3739.

(17) Su, H.; Hurd Price, C. A.; Jing, L.; Tian, Q.; Liu, J.; Qian, K. Janus Particles: Design, Preparation, and Biomedical Applications. *Mater. Today Bio*. **2019**, *4,* 100033.

(18) Rosenthal, G.; Gubbins, K. E.; Klapp, S. H. L. Self-Assembly of Model Amphiphilic Janus Particles. *J. Chem. Phys.* **2012**, *136* (17), 174901.

(19) Zhang, X.; Fu, Q.; Duan, H.; Song, J.; Yang, H. Janus Nanoparticles: From Fabrication to (Bio)Applications. *ACS Nano* **2021**, *15* (4), 6147–6191.

(20) Kirillova, A.; Marschelke, C.; Synytska, A. Hybrid Janus Particles: Challenges and Opportunities for the Design of Active Functional Interfaces and Surfaces. *ACS Appl. Mater. Interfaces* **2019**, *11* (10), 9643–9671.

(21) Schick, I.; Lorenz, S.; Gehrig, D.; Tenzer, S.; Storck, W.; Fischer, K.; Strand, D.; Laquai, F.; Tremel, W. Inorganic Janus Particles for Biomedical Applications. *Beilstein J. Nanotech.* **2014**, *5*, 2346–2362.

(22) Pengo, P.; Şologan, M.; Pasquato, L.; Guida, F.; Pacor, S.; Tossi, A.; Stellacci, F.; Marson, D.; Boccardo, S.; Pricl, S.; Posocco, P. Gold Nanoparticles with Patterned Surface Monolayers for Nanomedicine: Current Perspectives. *European Biophys. J.* **2017**, *46* (8), 749–771.

(23)   Singh, C.; Ghorai, P. K.; Horsch, M. A.; Jackson, A. M.; Larson, R. G.; Stellacci, F.; Glotzer, S. C. Entropy-Mediated Patterning of Surfactant-Coated Nanoparticles and Surfaces. *Phys. Rev. Lett.* **2007**, *99* (22), 226106.

(24)   Ghorai, P. Kr.; Glotzer, S. C. Atomistic Simulation Study of Striped Phase Separation in Mixed-Ligand Self-Assembled Monolayer Coated Nanoparticles. *J. Phys. Chem. C* **2010**, *114* (45), 19182–19187.

(25)   Ge, X.; Ke, P. C.; Davis, T. P.; Ding, F. A Thermodynamics Model for the Emergence of a Stripe-like Binary SAM on a Nanoparticle Surface. *Small.* **2015**, *11* (37), 4894–4899.

(26)   Velachi, V.; Bhandary, D.; Singh, J. K.; Cordeiro, M. N. D. S. Striped Gold Nanoparticles: New Insights from Molecular Dynamics Simulations. *J. Chem. Phys.* **2016**, *144* (24), 244710.

(27)   Groot, R. D.; Warren, P. B. Dissipative Particle Dynamics: Bridging the Gap between Atomistic and Mesoscopic Simulation. *J. Chem. Phys.* **1997**, *107* (11), 4423–4435.

(28)   Li, X.; Chen, L.; Cui, D.; Jiang, W.; Han, L.; Niu, N. Preparation and Application of Janus Nanoparticles: Recent Development and Prospects. *Coordination Chem. Rev.* **2022**, *454,* 214318.

(29)   Kang, C.; Honciuc, A. Influence of Geometries on the Assembly of Snowman-Shaped Janus Nanoparticles. *ACS Nano* **2018**, *12* (4), 3741–3750.

(30)   Sayers, E. W.; Bolton, E. E.; Brister, J. R.; Canese, K.; Chan, J.; Comeau, D. C.; Connor, R.; Funk, K.; Kelly, C.; Kim, S.; Madej, T.; Marchler-Bauer, A.; Lanczycki, C.; Lathrop, S.; Lu, Z.; Thibaud-Nissen, F.; Murphy, T.; Phan, L.; Skripchenko, Y.; Tse, T.; Wang, J.; Williams, R.; Trawick, B. W.; Pruitt, K. D.; Sherry, S. T. Database Resources of the National Center for Biotechnology Information. *Nucleic Acids Res.* **2022**, *50* (D1), D20–D26.

(31)   Berman H. M.; Westbrook J.; Feng, Z.; Gilliland G.; Bhat T. N.; Weissig H.; Shindyalov I. N.; Bourne P. E. The Protein Data Bank. *Nucleic Acids Res.* **2000**, *28* (1), 235–242.

(32)   Kipriyanov, S.; Hoffmann, K.; le Gall, F.; Knackmuss, S. Anti-CD16 Binding Molecules. US009035026B2, May 19, 2015.

(33)   Frisch, M. J.; et al. Gaussian 16, Revision C.01. Gaussian Inc 2016.

(34)   Zhao, Y.; Truhlar, D. G. Applications and Validations of the Minnesota Density Functionals. *Chem. Phys. Lett.* **2011**, *502* (1–3), 1–13.

(35)   Dunning Jr, T. H.; Hay, P. J. Modern Theoretical Chemsitry. Ed. H. F. Schaefer III: Plenum, New York 1977, pp 1–28.

(36)   Hay, P. J.; Wadt, W. R. *Ab Initio* Effective Core Potentials for Molecular Calculations. Potentials for K to Au Including the Outermost Core Orbitals. *J. Chem. Phys.* **1985**, *82* (1), 299–310.

(37) Wadt, W. R.; Hay, P. J. *Ab Initio* Effective Core Potentials for Molecular Calculations. Potentials for Main Group Elements Na to Bi. *J. Chem. Phys.* **1985**, *82* (1), 284–298.

(38) Hay, P. J.; Wadt, W. R. *Ab Initio* Effective Core Potentials for Molecular Calculations. Potentials for K to Au Including the Outermost Core Orbitals. *J. Chem. Phys.* **1985**, *82* (1), 299–310.

(39) Marenich, A. v.; Cramer, C. J.; Truhlar, D. G. Universal Solvation Model Based on Solute Electron Density and on a Continuum Model of the Solvent Defined by the Bulk Dielectric Constant and Atomic Surface Tensions. *J. Phys. Chem. B* **2009**, *113* (18), 6378–6396.

(40) de Meyer, F. J. M.; Rodgers, J. M.; Willems, T. F.; Smit, B. Molecular Simulation of the Effect of Cholesterol on Lipid-Mediated Protein-Protein Interactions. *Biophys. J.* **2010**, *99* (11), 3629–3638.

(41) Ramsay Taylor, W. The Classification of Amino Acid Conservation. *J. Theor. Biol.* **1986**, *119,* 205-218.

(42) Kyte, J.; Doolittle, R. F. A Simple Method for Displaying the Hydropathic Character of a Protein. *J. Mol. Bio.* **1982**, *157* (1), 105-132.

(43) Kolny, J.; Kornowski, A.; Weller, H. Self-Organization of Cadmium Sulfide and Gold Nanoparticles by Electrostatic Interaction. *Nano Lett.* **2002**, *2* (4), 361–364.

(44) Tripathi, K.; Driskell, J. D. Quantifying Bound and Active Antibodies Conjugated to Gold Nanoparticles: A Comprehensive and Robust Approach To Evaluate Immobilization Chemistry. *ACS Omega* **2018**, *3* (7), 8253–8259.

(45) Kumar, S.; Aaron, J.; Sokolov, K. Directional Conjugation of Antibodies to Nanoparticles for Synthesis of Multiplexed Optical Contrast Agents with Both Delivery and Targeting Moieties. *Nat. Protoc.* **2008**, *3* (2), 314–320.

(46) Jazayeri, M. H.; Amani, H.; Pourfatollah, A. A.; Pazoki-Toroudi, H.; Sedighimoghaddam, B. Various Methods of Gold Nanoparticles (GNPs) Conjugation to Antibodies. *Sens. Biosensing Res* **2016**, *9*, 17–22.

(47) Rayavarapu, R. G.; Petersen, W.; Ungureanu, C.; Post, J. N.; van Leeuwen, T. G.; Manohar, S. Synthesis and Bioconjugation of Gold Nanoparticles as Potential Molecular Probes for Light-Based Imaging Techniques. *Int J. Biomed. Imaging.* **2007**, *2007*, 1–10.

(48) Chen, Z.; Peng, Z.; Zhang, P.; Jin, X.; Jiang, J.; Zhang, X.; Shen, G.; Yu, R. A Sensitive Immunosensor Using Colloidal Gold as Electrochemical Label. *Talanta* **2007**, *72* (5), 1800–1804.

(49)   Zhang, Z.; Wang, S.; Xu, H.; Wang, B.; Yao, C. Role of 5-Aminolevulinic Acid-Conjugated Gold Nanoparticles for Photodynamic Therapy of Cancer. *J. Biomed. Opt.* **2015**, *20* (5), 051043.

Chapter 5:

Effect of pH on the SRPs

This chapter is the continuation and final part of the research developed in **Chapter 4**. Both can be considered as a single entity for studying the obtention of spherical Janus distributions onto Au NP surface. However, for an easier approach, it was decided to split the information into two parts: the first part addresses the derivation of SRP considering the structure of R at approximately pH 7, while the second part examines how the SRP values are influenced in response to the structure that AAs side chain (R) adopt under varying pH conditions.

Unlike in **Chapter 4**, the structure of the AAs will be subjected to changes based on pH values. Please note that in previous chapter, the structure of each AA's side chain (R) was kept constant. However, due to the pH changes addressed in this chapter, these structures will change. For this reason, we find necessary to provide a brief introduction to introduce the basis properties of AAs.

5.1. pH effect on IgGs

As the building blocks that make up IgG, AAs are pH-sensitive due to their ionizable functional groups[1]. Each AA is structured by a tetrahedral carbon bound to a hydrogen, an amino group, a carboxyl group and a R which defines their specific structure, charge and polarity. The general formula is: NH_2-CHR-COOH[2].

It is well known that at a certain pH (isoelectric point *a.k.a.* pI) the overall charges of AAs are zero. Indeed, AAs are close to the pI under physiological conditions. However, when the pH is lower than the pI, the ionizable groups are prone to accepting protons (H^{+}), which results in a net positive charge for the AA. Conversely, if the pH is higher than the pI, the ionizable groups lose H^{+} and the overall charge of the AAs becomes negative[3]. As said in **Chapter 4**, our focus was primarily on the R groups, thereby neglecting the pH effect for the amino or the carboxyl groups.

Depending on the pH values, the polarity of R will vary in their hydrophilic and hydrophobic character, and consequently, in their solubility in water[4]. Hsieng-Cheng *et al.*[5] investigated the solubility of AAs in water at various pH levels. They concluded that the solubility of serine is greater than alanine, leucine, isoleucine and phenylalanine due to the hydroxyl group of the R that can be dissolved better in aqueous solutions. The impact of pH on the solubility of divalent and trivalent AAs was explored by Ching-Yi and co-workers[6]. Their findings revealed that tyrosine, glutamine and asparagine remained neutral at pH 7, while the dominant structure for aspartic and glutamic acids was anionic.

Moreover, pH values not only influence the polarity of AAs, but they also impact the stability of IgG. The AAs sequence can shed light on whether a protein will be susceptible to aggregation or not. The presence of protein aggregates is considered undesirable in biotherapeutics because they may cause adverse effects or immunogenic reactions on administration[7].

This phenomenon is typically described based on the balance between the attractive and repulsive interactions within and among proteins. By changing the pH, the potential to form hydrogen bonds, the hydrophobic effect and, the protein charge of the protein can be altered[8–10]. Generally, if the net charge of a protein increases, aggregation is decelerated. Per contra, if proteins have a lower net charge, their propensity to aggregate is elevated[11].

Cromwell *et al.*[12] explored the challenges associated with proteins aggregation during the manufacturing process. They emphasized that aggregates could form depending on the hydrophobicity, charged, and size of the monomers involved. More recently, Lan and co-workers[9] characterized the surface properties of Bovine Serum Albumin. They demonstrated that a decrease in pH led to a positive surface charge of the protein, while higher pH values gave rise to negative surfaces. Regarding immunoglobulins, Sahin *et al.*[13] centered their research on investigating the effects of pH and aggregation pathways for human IgG1 proteins. They deduced that at higher pH, attractive electrostatic interactions were promoted.

Still further, several studies have demonstrated that pH also affects the conformational state of proteins. Although we have not centered our focus on this challenge, it is worth noting that pH can also induce conformational changes in IgG. In 1991, Calmettes and co-workers[14] employed scattering methods to determine the conformational changes in IgG. By means of changes in the radius of gyration, they assumed that the conformational change appeared either in the hinge region of the immunoglobulins or in the interdomain areas within the F_{ab}. They also concluded that, at lower pH, the antigen-antibody interactions could be disrupted since the AAs' structure could be affected by pH, thereby losing the intermolecular interactions between the compounds.

Indeed, pH plays an important role in the immunoglobulins function due to its ability to alter the ionization of AAs, which in turn can transform the protein structure or shape[15]. As commented, computational predictions are advantageous when material availability is limited. CG models have been applied to study the essential properties of immunoglobulins that are otherwise challenging to elucidate using classical MD.

An example of the use of CG models to study the effect of pH and salt concentration on the stability for Protein G was done by Martins de Oliveira *et al*[16]. They succeeded in quantifying the importance of charged residues in the protein stability.

Chaudhri and co-workers[17] explored the role of electrostatic charges at the self-association of two antibodies by developing two types of CG models based on different antibody regions (12 and 26 CG beads, respectively), although no substantial differences were observed. Their results suggested that electrostatic charges are crucial in determining the interactions between the F_c and the F_{ab} due to the net charge of these domains. Following the same line, they published an article a year later[18] where they explored the behavior of the same antibodies by altering their AAs structure. Notable shifts in the equilibrium of these systems in solution were observed with minor changes in the AAs sequences. Recently, Izadi *et al.*[19] aimed to improve the CG of antibodies by incorporating their hydrophobic character. They demonstrated that both the electrostatic and the hydrophobic interactions of antibodies are necessary to predict their properties in solution.

In order to elucidate the pH effect on obtaining Janus distributions using DPD, we chose to perform calculations in which the structure of R was altered in response to environmental pH. To this aim, the following key features were considered:

- Which R changed with respect to pH.

- Which is the structure that R adopted.

- How the new structure influence on the definition of SRP values.

It is important to mention that the present chapter focuses solely on exploring the possibility of obtaining spherical Janus distributions by varying the pH, using both A32 and 3G8. This approach will allow researchers to gain insights into the specific influence of pH on the structural properties of such IgG. **Nonetheless, it is noteworthy that this specific investigation does not focus on the potential denaturation or changes in the inherent properties of these systems as we worked with CG models.**

5.1.1. Which is the structure of R at different pH?

In this chapter **we only dealt with the structure that AAs R adopt as a function of the environmental pH**. As previously said, it is well known that the R of certain AAs are capable of releasing or binding protons (H^+). Since protons are charged, it follows that the loss or gain of protons is accompanied by a change in charge. The main R altered by pH are those from Asp, Glu, His, Cys, Tyr, Lys and Arg (**Figure 5.1**)[20].
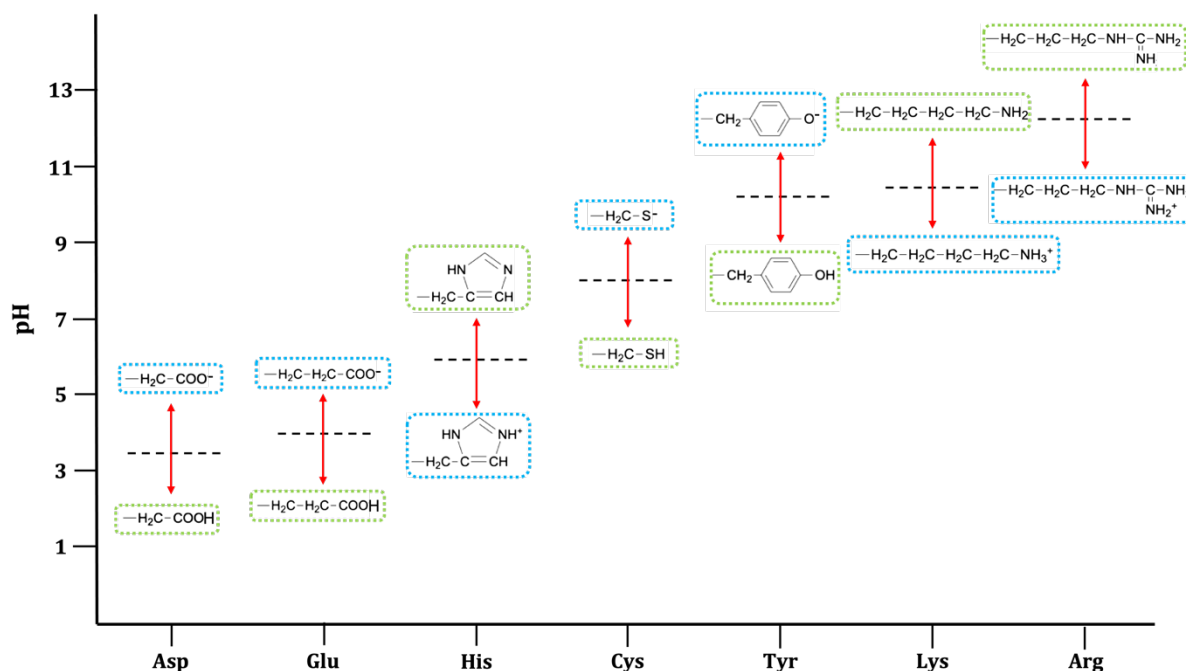
Figure 5.1: Structure of R at different pH. Neutral species appear in pear green dashed squares, while charged species are depicted in sky blue.

Figure 5.1 draws a suitable picture of the changes in the structure for the R mentioned previously at different pH levels. Dashed lines indicate the pI values specific to each AA. In this sense, the pI values of acidic Asp and Glu AAs are found at lower pH levels as their carboxylate groups accept H$^+$. On the contrary, the pI values of basic AAs occur at higher pH due to their amine groups, which can donate H$^+$. Also noteworthy is the fact that cysteine (Cys) and tyrosine (Tyr) can be deprotonated at higher pH values, approximately 8 and 10, respectively.

5.2. How the changes in pH affects the SRP values?

The study was conducted at five different pH values: 0, 4, 9, 11 and 14. Other values were omitted since no significant structural changes were appreciated. This helped us saving a considerable amount of computational time.

Before going to the point, it is important to state the assumptions that guided our work:

1) As in **section 4.3,** the CG applied was the one based on the Y-shape like form of IgG (4 CG beads).

2) AAs were also classified into ØP, P and E, like in **section** 4.2.1.2.

3) As said, the structure of R change from neutral to charged (and *vice versa*) with increases in pH (**Table 5.1**).

4) The SRP values were obtained applying "(IgGa-IgGb)4-(SRP)2-QM BS)" approach. For that, two considerations were considered. First, new structures were utilized to calculate the $\Delta E_{binding}$: Asp, Glu, His, Lys and Arg were considered neutral, while Cys and Tyr were considered negatively charged. Second, the SRP values not only considered the specific structure adopted by R within each IgG but also accounted for the total number of AAs present in each IgG. This assessment acknowledges the significance of both the structure and the overall composition of IgG, providing a more holistic understanding of their interacting properties. The resultant values can be found in: **Appendix C5-A**: Detailed calculations for 5.2 simulations.

Table 5.1: Structure of R for Asp, Glu, His, Cys, Tyr, Lys and Arg at five different pH.

R \ pH	Asp	Glu	His	Cys	Tyr	Lys	Arg
0	Neutral	Neutral	Charged	Neutral	Neutral	Charged	Charged
4	Charged	Neutral	Charged	Neutral	Neutral	Charged	Charged
9	Charged	Charged	Neutral	Charged	Neutral	Charged	Charged
11	Charged	Charged	Neutral	Charged	Charged	Neutral	Charged
14	Charged	Charged	Neutral	Charged	Charged	Neutral	Neutral

Accordingly, some AAs were moved throughout P and E groups whether if they were neutral or charged. As aforementioned, at the lowest pH (pH 0), all the species are protonated due to the high [H⁺] in solution. Thus, His, Lys and Arg fall into to E group, while the others four belong to P. Therefore, the percentage of E was decreased compared to pH 7. The first changed in the R structure occurs at about pH 4 when Asp loses its H⁺ to become charged, thereby moving from P to E group. On the other hand, at basic pH, Cys and Tyr can be also deprotonated at about pH 9 and 11, respectively. Cys loses its H⁺ to form the corresponding thiolate group, while Tyr forms the corresponding alkoxide. Thus, at the highest pH (i.e. 14) Asp, Glu, Cys and Tyr belong to E group, while His, Lys and Arg belong to P group.

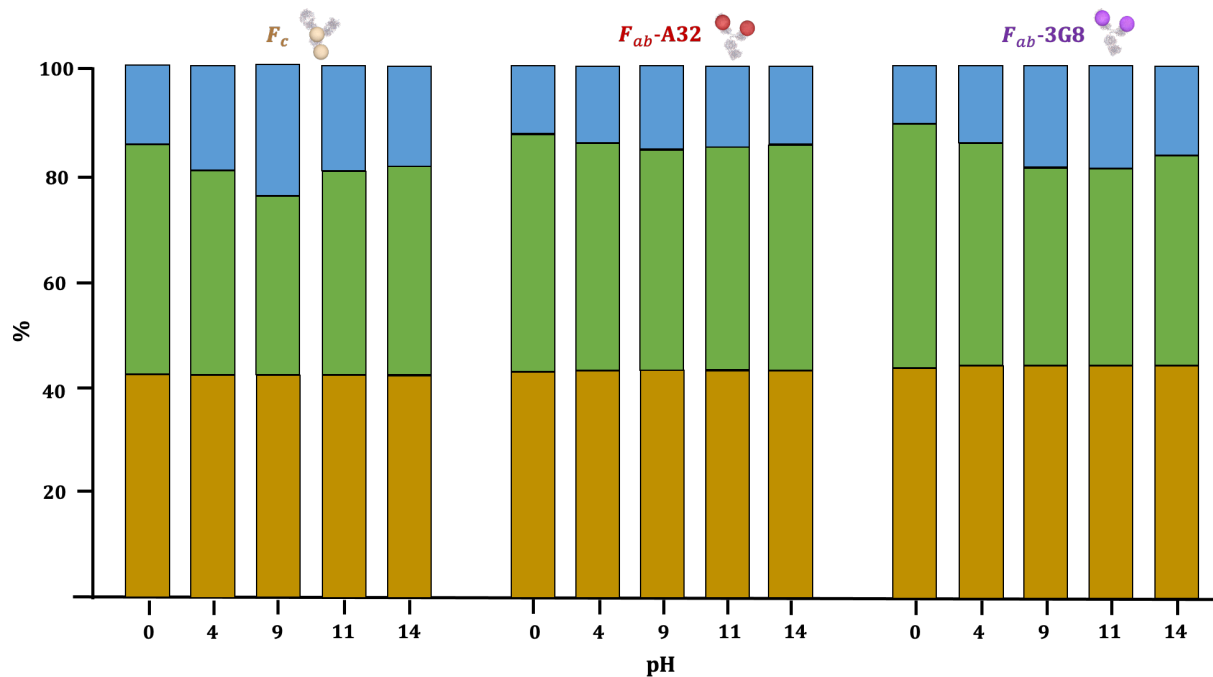The results of the percentages of each AA group for F_c and F_{ab} at different pH are shown in **Figure 5.2.**

Figure 5.2: Percentages of ØP, P and E at different pH for each bead. ØP are depicted in marigold, P in pear green and E in sky blue.

Notice in **Figure 5.2**, that ØP are not pH-dependent since the number of AAs in this group remains constant across all pH values, whereas the quantity of **P and E in each fragment (F_c and F_{ab}) changes as the pH increases.**

The observed trend is intriguing. Broadly speaking, the increase in E AAs up to pH 9 implies that at lower pH levels, AAs such His, Tyr and Lys are protonated and carry a positive charged. As the pH increases, making the environment more alkaline, these charged AAs deprotonate until pH 9 and lose their positive charges. Conversely, the proportion of P decreases beyond pH 9 and then starts to rise again. The subsequent decrease in E until pH 9 indicates that at higher pH levels, AAs like Asp, Glu, Cys and Tyr are deprotonated and acquire a negative charge. It is worth nothing that such tendency is less pronounced for F_{ab}-A32. This reaffirms how the specific AA sequences within the F_{ab} can greatly differ among IgGs, allowing immunoglobulins to identify and attach to a broad variety of antigens. On the other hand, the conservation in the F_c provides stability and imparts specific functions to the IgGs[21].

Overall, these findings highlight the crucial role of pH in influencing the charge state of AAs and demonstrate how variations in pH can significantly affect the charge distribution in proteins and peptides[22–25]. As mentioned earlier, the calculated SRPs took into account both the structure and the total number of AAs in each IgG. **Table 5.2** presents the resultant matrices obtained at pH values of 0, 4, 11 and 14.

Table 5.2: Resultant matrices for pH 0, 4, 9 and 14. The crucial parameters to obtain Janus distributions are depicted in crimson red, bright purple and magenta for F_{ab}-A32/F_{ab}-A32, F_{ab}-3G8/F_{ab}-3G8 and F_{ab}-A32/F_{ab}-3G8, respectively.

pH	SRP	W	Au	F_c	F_{ab}-A32	F_{ab}-3G8
	W	25	120	58	60	63
	Au		1	21	29	21
0	F_c			49	55	55
	F_{ab}-A32				48	55
	F_{ab}-3G8					48

pH	SRP	W	Au	F_c	F_{ab}-A32	F_{ab}-3G8
	W	25	120	57	60	62
	Au		1	21	28	21
4	F_c			49	56	56
	F_{ab}-A32				48	56
	F_{ab}-3G8					48

pH	SRP	W	Au	F_c	F_{ab}-A32	F_{ab}-3G8
	W	25	120	57	59	62
	Au		1	5	5	5
9	F_c			50	56	56
	F_{ab}-A32				49	56
	F_{ab}-3G8					49

pH	SRP	W	Au	F_c	F_{ab}-A32	F_{ab}-3G8
	W	25	120	58	60	62
	Au		1	5	5	5
14	F_c			49	56	56
	F_{ab}-A32				48	56
	F_{ab}-3G8					48

When examining the values in **Table 5.2**, it is evident that changing the pH from 0 to 14 does not significantly affect the interactions between IgGs: F_{ab}**-A32**/F_{ab}**-A32**, F_{ab}**-3G8**/F_{ab}**-3G8** and F_{ab}**-A32**/F_{ab}**-3G8**. Although the SRP values are more attractive within same IgG than for the different ones, the differences are not substantial. This indicates that the variations in the SRP values are not significant enough to achieve Janus distributions onto Au NPs (as shown in **Chapter 4**).

Interestingly, at higher pH values, the deprotonation of Cys results in the formation of negatively charged thiolate groups (RS⁻). **It is important to note that we have considered Cys to be free in solution in these calculations, without taking into account the fact that they often form disulfide bridges**[26]. Said in **Chapter 3**, this change in charge significantly enhances the affinity towards to Au. Bearing in mind that SRP values for Au accounted for the effect of Boltzmann distributions, it becomes evident that the contribution of Cys plays a crucial role in the overall interaction. As a result, the final values for **Au**/F_c, **Au**/F_{ab}**-A32** and **Au**/F_{ab}**-3G8** became more attractive. This suggests that the adsorption of IgG onto the Au NP was facilitated.

From all the results stated above, the main differences between acidic and basic conditions lie in the favorability of the interaction between IgG and Au, as well as the speed of IgG adsorption. The lower is the SRP value, the easier it is for the compounds to approach each other. This is especially true at basic pH when free Cys adopted a negative charge. This observation is in line with experimental procedures in which antibodies are specifically modified to facilitate their adsorption onto Au NPs[27]. This ability is crucial for various applications in nanotechnology, as it enables efficient functionalization and the use of Au NPs as platforms for targeted drug delivery[28], biosensing[29], and others[30,31]. Understanding the pH-dependent variations in antibody-gold interactions provides valuable insights for designing and optimizing such systems for a practical use[29,32].

5.3. Conclusions

The approach used to define the SRP values has not shown to be sensible at changes in pH. However, interesting results were observed at basic pH in which Cys is deprotonated to form the corresponding thiolate groups. In such conditions, **Au**/F_c, **Au**/F_{ab}**-A32** and **Au**/F_{ab}**-3G8** become more attractive giving an easily adsorption of IgG onto Au NP surface.

Summarizing, our findings highlight the critical role of pH in the classification of R groups and the subsequent implications for the derivation of the SRP values. Furthermore, our study suggests that further investigations could explore how SRP values might change when employing an alternative classification of R.

5.4. Highlights of the chapter

The most relevant highlights of this chapter are listed below:

- Presented the R groups that are pH-dependent.

- Changed the Asp, Glu, His, Cys, Tyr, Lys and Arg throughout P or E groups depending on whether if they are neutral or charged at different pH.

- Shown the SRP matrices obtained at both acid and basic pH.

5.5. References

(1)   Bonvin, P.; Venet, S.; Fontaine, G.; Ravn, U.; Gueneau, F.; Kosco-Vilbois, M.; Proudfoot, A. el; Fischer, N. *De Novo* Isolation of Antibodies with PH-Dependent Binding Properties. *MAbs* **2015**, *7* (2), 294–302.

(2)   Wu, G. Amino Acids: Metabolism, Functions, and Nutrition. *Amino Acids* **2009**, *37* (1), 1–17.

(3)   Arosio, P.; Rima, S.; Morbidelli, M. Aggregation Mechanism of an IgG2 and Two IgG1 Monoclonal Antibodies at Low PH: From Oligomers to Larger Aggregates. *Pharm. Res.* **2013**, *30* (3), 641–654.

(4)   Borsook, H.; Macfadyen, D. A. the effect of isoelectric amino acids on the ph of a phosphate buffer solution a contribution in support of the "zwltter ion" hypothesis. *J. Gen. Physiol.* **1930**, *13* (5), 509–527.

(5)   Tseng, H.-C.; Lee, C.-Y.; Weng, W.-L.; Shiah, I.-M. Solubilities of Amino Acids in Water at Various PH Values under 298.15K. *Fluid Phase Equilib.* **2009**, *285* (1–2), 90–95.

(6)   Lee, C.-Y.; Chen, J.-T.; Chang, W.-T.; Shiah, I.-M. Effect of PH on the Solubilities of Divalent and Trivalent Amino Acids in Water at 298.15K. *Fluid Phase Equilib.* **2013**, *343*, 30–35.

(7)   Rosenberg, A. S. Effects of Protein Aggregates: An Immunologic Perspective. *AAPS J.* **2006**, *8* (3), E501–E507.

(8)   Zapadka, K. L.; Becher, F. J.; Gomes dos Santos, A. L.; Jackson, S. E. Factors Affecting the Physical Stability (Aggregation) of Peptide Therapeutics. *Interface Focus* **2017**, *7* (6), 20170030.

(9)   Lan, H.; Liu, H.; Ye, Y.; Yin, Z. The Role of Surface Properties on Protein Aggregation Behavior in Aqueous Solution of Different PH Values. *AAPS Pharm. Sci. Tech.* **2020**, *21* (4), 122-135.

(10)   le Basle, Y.; Chennell, P.; Tokhadze, N.; Astier, A.; Sautou, V. Physicochemical Stability of Monoclonal Antibodies: A Review. *J. Pharm. Sci.* **2020**, *109* (1), 169–190.

(11)   Radzicka, A.; Wolfenden, R. Comparing the Polarities of Amino Acids: Side-Chain Distribution Coefficients between the Vapor Phase, Cyclohexane, 1-Octanol, and Neutral Aqueous Solution. *Biochemistry* **1988**, *27* (5), 1670–1677.

(12)   Cromwell, M. E. M.; Hilario, E.; Jacobson, F. Protein Aggregation and Bioprocessing. *AAPS J.* **2006**, *8* (3), E572–E579.

(13)   Sahin, E.; Grillo, A. O.; Perkins, M. D.; Roberts, C. J. Comparative Effects of PH and Ionic Strength on Protein–Protein Interactions, Unfolding, and Aggregation for IgG1 Antibodies. *J. Pharm. Sci.* **2010**, *99* (12), 4830–4848.

(14)   Calmettes, P.; Cser, L.; Rajnavölgyi, É. Temperature and PH Dependence of Immunoglobulin G Conformation. *Arch. Biochem. Biophys.* **1991**, *291* (2), 277–283.

(15)   Dumetz, A. C.; Chockla, A. M.; Kaler, E. W.; Lenhoff, A. M. Effects of PH on Protein–Protein Interactions and Implications for Protein Phase Behavior. *Biochimica et Biophysica Acta (BBA) - Proteins and Proteomics* **2008**, *1784* (4), 600–610.

(16)   Martins de Oliveira, V.; Godoi Contessoto, V. de; Bruno da Silva, F.; Zago Caetano, D. L.; Jurado de Carvalho, S.; Pereira Leite, V. B. Effects of PH and Salt Concentration on Stability of a Protein G Variant Using Coarse-Grained Models. *Biophys. J.* **2018**, *114* (1), 65–75.

(17)   Chaudhri, A.; Zarraga, I. E.; Kamerzell, T. J.; Brandt, J. P.; Patapoff, T. W.; Shire, S. J.; Voth, G. A. Coarse-Grained Modeling of the Self-Association of Therapeutic Monoclonal Antibodies. *J. Phys. Chem. B* **2012**, *116* (28), 8045–8057.

(18)   Chaudhri, A.; Zarraga, I. E.; Yadav, S.; Patapoff, T. W.; Shire, S. J.; Voth, G. A. The Role of Amino Acid Sequence in the Self-Association of Therapeutic Monoclonal Antibodies: Insights from Coarse-Grained Modeling. *J. Phys. Chem. B* **2013**, *117* (5), 1269–1279.

(19)   Izadi, S.; Patapoff, T. W.; Walters, B. T. Multiscale Coarse-Grained Approach to Investigate Self-Association of Antibodies. *Biophys. J.* **2020**, *118* (11), 2741–2754.

(20)   Lide, D. R. *Handbook of Chemistry and Physics*, 72nd Edition.; CRC Press: Boca Raton, FL, 1991.

(21) Schroeder, H. W.; Cavacini, L. Structure and Function of Immunoglobulins. *J. Aller. Clinic. Immuno.* **2010**, *125* (2), S41–S52.

(22) Wada, A.; Nakamura, H. Nature of the Charge Distribution in Proteins. *Nature* **1981**, *293* (5835), 757–758.

(23) Lošdorfer Božič, A.; Podgornik, R. PH Dependence of Charge Multipole Moments in Proteins. *Biophys. J.* **2017**, *113* (7), 1454–1465.

(24) Di Savino, A.; Foerster, J. M.; Ullmann, G. M.; Ubbink, M. The Charge Distribution on a Protein Surface Determines Whether Productive or Futile Encounter Complexes Are Formed. *Biochemistry* **2021**, *60* (10), 747–755.

(25) Mapiour, M.; Abdelrasoul, A. Critical Influences of Plasma PH on Human Protein Properties for Modeling Considerations: Size, Charge, Conformation, Hydrophobicity, and Denaturation. *J. Comp. Sci.* **2023**, *7* (1), 28.

(26) Di Pasqua, A. J.; Mishler, R. E.; Ship, Y.-L.; Dabrowiak, J. C.; Asefa, T. Preparation of Antibody-Conjugated Gold Nanoparticles. *Mater. Lett.* **2009**, *63* (21), 1876–1879.

(27) Kim, C.; Agasti, S. S.; Zhu, Z.; Isaacs, L.; Rotello, V. M. Recognition-Mediated Activation of Therapeutic Gold Nanoparticles inside Living Cells. *Nat. Chem.* **2010**, *2* (11), 962–966.

(28) Eck, W.; Craig, G.; Sigdel, A.; Ritter, G.; Old, L. J.; Tang, L.; Brennan, M. F.; Allen, P. J.; Mason, M. D. PEGylated Gold Nanoparticles Conjugated to Monoclonal F19 Antibodies as Targeted Labeling Agents for Human Pancreatic Carcinoma Tissue. *ACS Nano* **2008**, *2* (11), 2263–2272.

(29) Huang, Y.-F.; Liu, H.; Xiong, X.; Chen, Y.; Tan, W. Nanoparticle-Mediated IgE−Receptor Aggregation and Signaling in RBL Mast Cells. *J. Am. Chem. Soc.* **2009**, *131* (47), 17328–17334.

(30) Kumar, S.; Aaron, J.; Sokolov, K. Directional Conjugation of Antibodies to Nanoparticles for Synthesis of Multiplexed Optical Contrast Agents with Both Delivery and Targeting Moieties. *Nat. Protoc.* **2008**, *3* (2), 314–320.

(31) Sokolov, K.; Follen, M.; Aaron, J.; Pavlova, I.; Malpica, A.; Lotan, R.; Richards-Kortum, R. Real-Time Vital Optical Imaging of Precancer Using Anti-Epidermal Growth Factor Receptor Antibodies Conjugated to Gold Nanoparticles. *Cancer. Res.* **2003**, *63* (9), 1999–2004.

Chapter 6:

Applying Martini force field

to study the dynamics of G4

This Chapter was done in collaboration with Prof. Isabel Rozas at the Trinity College Dublin (TCD) during a stay of three months. Prof. Rozas specializes in the investigation of modeling, preparation, and examination of the biophysical properties of various agents with potential applications as antidepressants or antipsychotic agents. In this context, this chapter focuses on the procedures undertaken to simulate a G-quadruplex (G4) using the Martini force field. Additionally, the chapter explores the interactions between the G4 and two diaromatic guanidium-porphyrin conjugates.

6.1. A survey of G-quadruplexes

As quoted by Prof. Chaires:

"G-quadruplexes (G4) have evolved from being a biophysical oddity to being structures of functional significance in biology."

G-quadruplexes, also known as G4s, are diverse structures made from one, two or even four unconnected deoxyribonucleic acid (DNA) strands. In this case, DNA is formed by four guanine units (**Figure 6.1.a**) assembling themselves to form planar G-tetrads (**Figure 6.1.b**). These tetrads can then stack helically upon each other, creating a central channel which can be filled with cations, which help to stabilize the G4 structure[1]. These structures can be either parallel or antiparallel, depending on the orientation of the DNA strands. In a parallel G4 (**Figure 6.1.c**), all of the strands are oriented in the same direction, while in an antiparallel, the strands alternate direction.
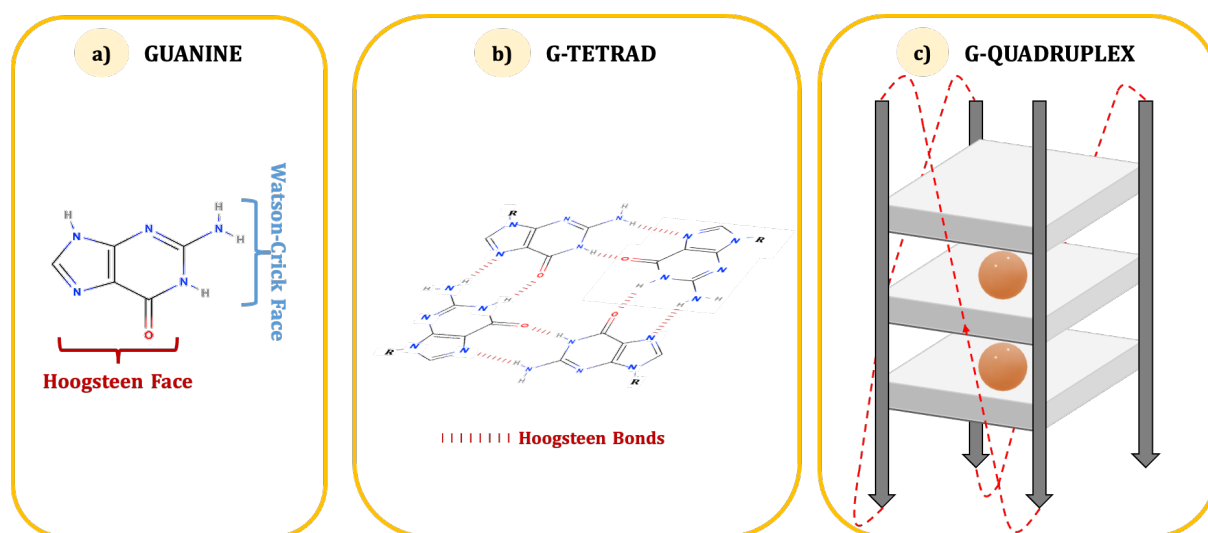
Figure 6.1: Components of a G4 structure. **a)** Guanine base (1D). Two different faces to form hydrogen bonding: **Watson-Crick** face and **Hoogsteen** face. **b)** G-tetrad (2D). Guanines are aligned in square conformation to form **Hongsteen** hydrogen bonds (depicted in dark red dashed lines). **c)** Scheme for the 3D structure of **c-kit2**[2], a G4 which plays an important role in cell growth, proliferation, migration, and survival. This structure is formed by: G-tetrads (in light gray), G-columns (dark gray narrows) and the loops (depicted in dashed color red). The central channel is occupied by metal ions (depicted in orange).

Figure 6.1 illustrates that guanine is absolutely essential for the formation of G4s. Unlike other bases, guanine can form hydrogen bonds with two adjacent surfaces known as the **Watson-Crick** and the **Hoogsteen** faces (**Figure 6.1.a**). The fact of having hydrogen bond acceptors and donors allow them to participate in Hoogsteen bonding[3]. These pairings establish eight hydrogen bonds among four guanines, leading to a high propensity for self-associate into G-tetrads. These G-tetrads can stack on each other for further stability due to the vertical-vertical base interaction via π-stacking[4]. A stable G4 arises from the stacking of at least two of these G-tetrads, which are held together by loops created by the nucleotides not involved in the G-tetrads. These loop regions act as the connectors of any two G-columns. Their existence is not mandatory, and the number of loops can vary depending on whether the G4 is intramolecular or intermolecular. On the other hand, G-columns form the four pillar-like structures consisting of the sugar-phosphate backbone of the four strands of nucleic acids. Finally, the central channel of G4 is occupied by metal ions.

Despite the early breakthrough of G4s in 1963, it has not been until the last two decades when much of the current knowledge has been obtained. Evidence of G4s predates the discovery of the Watson Crick duplex, and the first report on G4 came from the observation made by Prof. Ivar Bang[5] in 1910, where he found that guanylic acid forms gel at higher concentration. At that time, scientists regarded this phenomenon to be a mere *in vitro* artifact because of the artificial conditions in the test tubes. It was only in 1962, when Gellert's and co-workers[6] worked with X-ray diffraction data on guanylic acid (**Figure 6.2**), that the gelling property of guanylic acid (**Figure 6.2**) was explained. Shortly thereafter, DNA and ribonucleic acid (RNA) were confirmed to be able to adopt this structure. However, due to the attention garnered by the discovery of duplexes by Watson and Crick, the G4s search was relatively slow over that period. Interest in G4 was revived in the late 80s and early 90s with the discovery of G4s in DNA sequences of biological significance. Several groups found that G-rich telomeric sequences were able to form a four-strand structured known as the G4[7,8].
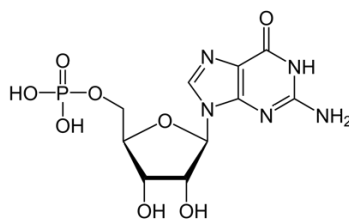

Figure 6.2: Chemical structure of guanylic acid (also known as guanosine monophosphate).

In this chapter, the dynamics of the **c-kit2**, was investigated using Martini force field. To perform a comprehensive analysis of the intricate system, it was essential to elucidate the key concepts underlying the physicochemical interactions that facilitate the formation of such structures. Understanding these fundamental principles is crucial for gaining insights into the behavior and characteristics of the **c-kit2**.

6.1.1. The building blocks of nucleic acids

DNA, which embodies the genetic code by which all organisms are specified, is made up of nucleotides which are constructed from phosphate groups, pentose sugars (deoxyribose) and heterocyclic bases. There are four different bases: adenine, guanine, cytosine and thymine. The first pair has a two-ring system (purines) whereas the second pair contains one-ring system (pyrimidines). The individual DNA strands are composed of heterocyclic bases connected to a deoxyribose sugar via a 1' carbon, which is connected to phosphate groups via a phosphodiester bond at both the 3' and 5' hydroxyl groups. Therefore, the covalent chains of nucleic acids are described as a backbone of alternating phosphate and pentose residues with different nitrogenous bases attached, giving rise to a particular sequence in which genetic information is encoded.

The association of strands results in a thermodynamically stable structure, as a result of noncovalent interactions. As said, heterocyclic bases not only can interact by Watson-Crick base-pairing process[10] but also, they can assemble independently via **Hoogsten** hydrogen bonding[3]. The last assembly was discovered by Prof. Karst Hoogsteen, who found a disorder in 1-methylthymine:9-methyladenine crystal structure in which 10-13% of the first one was rotated 180° about its axis in order to act as a hydrogen bond acceptor. By doing so, the number of possible structures that DNA can also adopt was expanded by allowing for a more twisted non-linear arrangement. The best-known examples are guanine-guanine and cytosine-cytosine base pairs. G-rich DNA strands can form G4s while C-rich DNA strands form i-motif structures. I-motifs are built of two parallel-stranded DNA duplexes held together in an antiparallel orientation by intercalated, cytosine-cytosine+ base pairs[11–13].

On top of horizontal base-base interactions, there are also vertical base-base interactions which are analogous to a roll of coins stacked up. The base stacking is due to the partial double-bond properties of the bases' aromatic rings in which the π orbital overlaps forming π conjugation (π-stacking). A slightly tilt between the bases can maximize the overlapping and overcoming steric hindrance. Other than π-stacking, hydrophobic and Van der Waals interactions are also key contributors to such interactions. On one hand, hydrophobic interaction promotes nonpolar groups interactions, which contributes to the stability of secondary and tertiary DNA structures. On the other hand, the weakest intermolecular forces but nonetheless a contributor are the Van der Waals forces. Temporary dipoles that polarize neighbors' molecules are created by the asymmetric electronic charge distribution within atomic groups.

Furthermore, G4s contain a central channel which is electrostatically stabilized by cations that can occupy the vacant cavities. The key consideration for a good G4-stabilizing cation is the ionic radius. It cannot be too large, which would destabilize the G4, or too small, which is insufficient to coordinate with negative charges of guanines. Of the large list of cations, Na^+ and K^+ are considered the most important due to their high concentrations in biologically relevant environments. Na^+ has a relatively smaller ionic radius and can situate within the plane of G-tetrad while K^+ has a larger ionic radius and thus situates between the planes of two G-tetrads[14–16]. In the present chapter, the influence of stabilizing ions was portrayed using dummy beads as a simpler representation. By employing dummy beads, the computational resources were reduced due to their fewer interaction sites.

The development of chemical compounds interacting with G4 has become popular research since the discovery that sequences of biological importance such as telomere or oncogene promoters can fold into G4s. About 1000 different chemical compounds to date have been studied. Generally, G4 ligands have a central core of aromatic scaffold to interact with G4s primarily through external π-stacking with the top G-tetrad. The planarity of these ligands may also, albeit to a lesser degree, intercalate between G-tetrads. If the ligands contain positive side chain groups, they can improve the binding by interacting with negatively charged regions such as phosphate backbone or the highly electronegative central channels of G4s. Since several of these ligands are lipophilic, some added side chains can enhance the water solubility. Although a plethora of ligands have been used for interacting with G4s, we focused our attention on diaromatic guanidium-porphyrin conjugates.

As mentioned, this study was done during my short stay at Trinity College Dublin (TCD) with Prof. Isabel Rozas. Her group have shown that these ligands can be used as selective architectures for G4 binders. However, it is necessary to gain more insights about the interaction of these kind of ligands with G4s. In this sense, the present chapter was devoted to study the dynamics of monomeric human **ckit-2** and its interaction with two porphyrin diphenyl guanidium conjugates (find their structure in the following section). Given the limited time available, we focused our attention on:

1) Investigating the stability, fluctuation, and compactness of such G4.

2) Exploring the effect of using the *meta-meta* or *para-para* substituted ligands (**Figure 6.3**) when interacting with the G4.
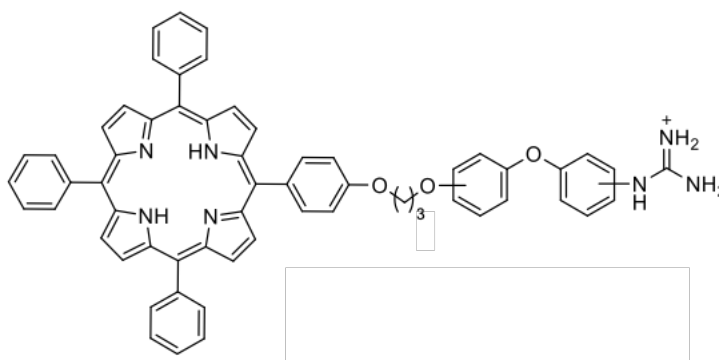
Figure 6.3: General structure for diphenyl guanidinium conjugates.

6.2. Simplifying the systems

6.2.1. CG Model for G4

As a reference system for G4 we chose the monomeric human **c-kit2**[2] from Protein Data Base (PDB). CG models for G4 were based on Martini force field developed for DNA[17] in which each nucleotide was mapped to six or seven CG beads. The phosphate-sugar backbone was modeled with one and two beads, respectively. Cytosine and thymine were modeled as three-bead rings whereas adenine and guanine as four CG beads. Thus, the structure was reduced from 677 atoms into 140 CG beads (**Figure 6.4**).
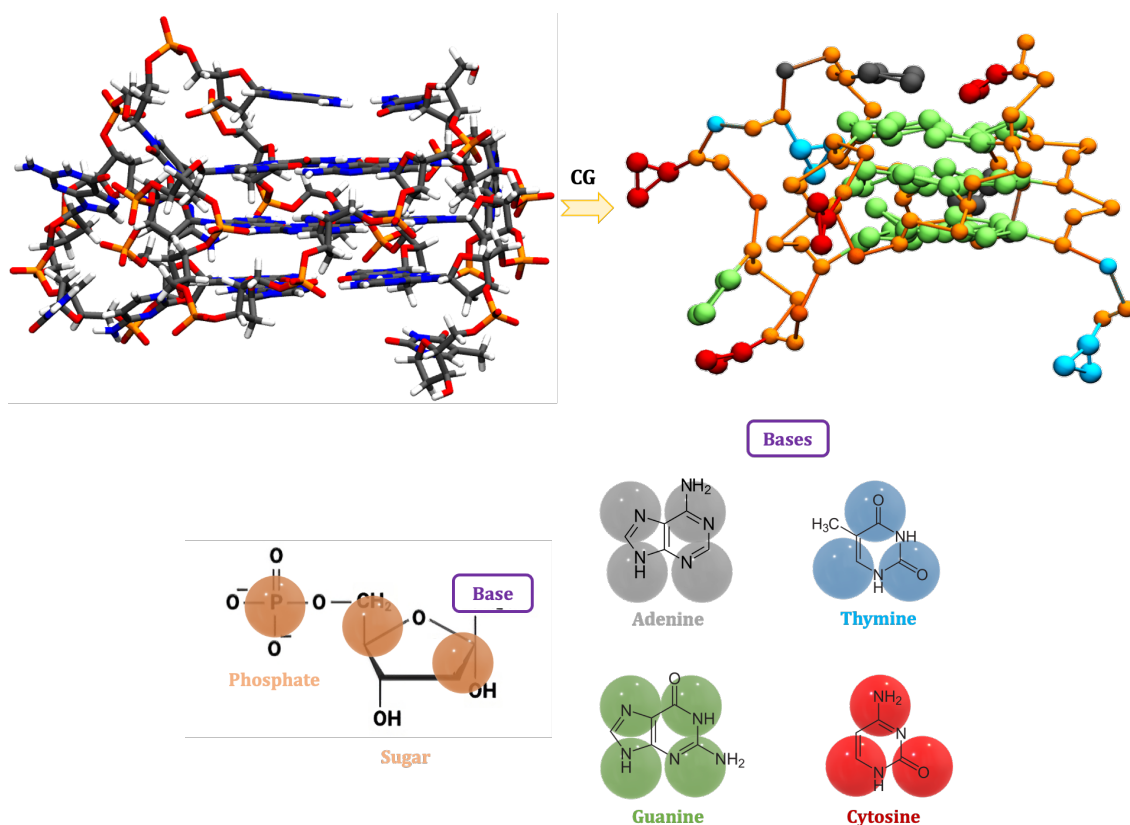
Figure 6.4: Mapping scheme for Martini CG model. Starting from the atomistic resolution model (on the left) to the CG model (on the right). The entire backbone (phosphate-sugar) is depicted in cantaloupe whereas nitrogenated bases are depicted as follows: adenine in light gray, **thymine** in light blue, **guanine** in light green and **cytosine** in red.

As aforementioned, we introduced two CG beads strategically placed between the G-tetrads to mimic the ions placed inside the G4 channel. To ensure that these beads did not interfere with the other compounds of the system, we employed two dummy beads. This approach serves several purposes:

1) To replicate the stabilizing effects induced by the ions in the stacking of G-tetrads.

2) To maintain the structural integrity of G4s. Without the presence of these beads, there might be a disruption in the arrangement of G-tetrads, potentially leading to an unstable or distorted structure.

3) To prevent unwanted interactions or interferences -caused by ions- that could influence the behavior of the G4s or the other components present in the simulation.

To do so, we strategically bound them to eight guanines, with four located above and four below them. This arrangement allowed the dummy beads to mimic the positioning of ions and reproduce their stabilizing effect on the G4. Furthermore, to further reinforce the structural stability, we also connected the dummies to each other, effectively forming bridges between them (**Figure 6.5**).
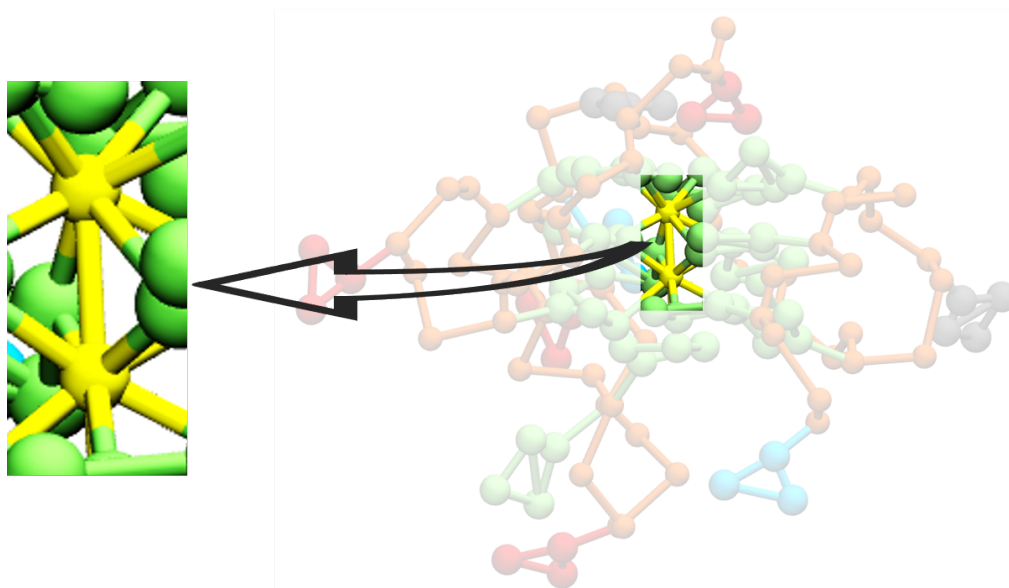

Figure 6.5: CG model for dummies (depicted in yellow). Each CG dummy is bonded to eight guanines (bonds depicted in yellow-green) and with the other dummy (yellow bond).

6.2.2. CG Model for porphyrin diphenyl guanidinium conjugates

As aforementioned, we performed the second part of the study with two different ligands diaromatic guanidium-porphyrin conjugates. Despite the scarce literature about these ligands coarse-graining, one can carry on the mentioned mapping for molecules that are not available in the repository by following the building block principle[18].

We firstly stabilized the all-atom structures with Gaussian software package[19] with the aim of obtaining an optimized and stable arrangement of the ligands. The structures were optimized by means of Density Functional Theory (DFT) method, B3LYP with the 6-31* basis set following Stipaničev *et al.* studies[20]. Next, we created the CG based on Martini philosophy reducing the atomistic compounds from 117 atoms to 34 CG beads (**Figure 6.6**).
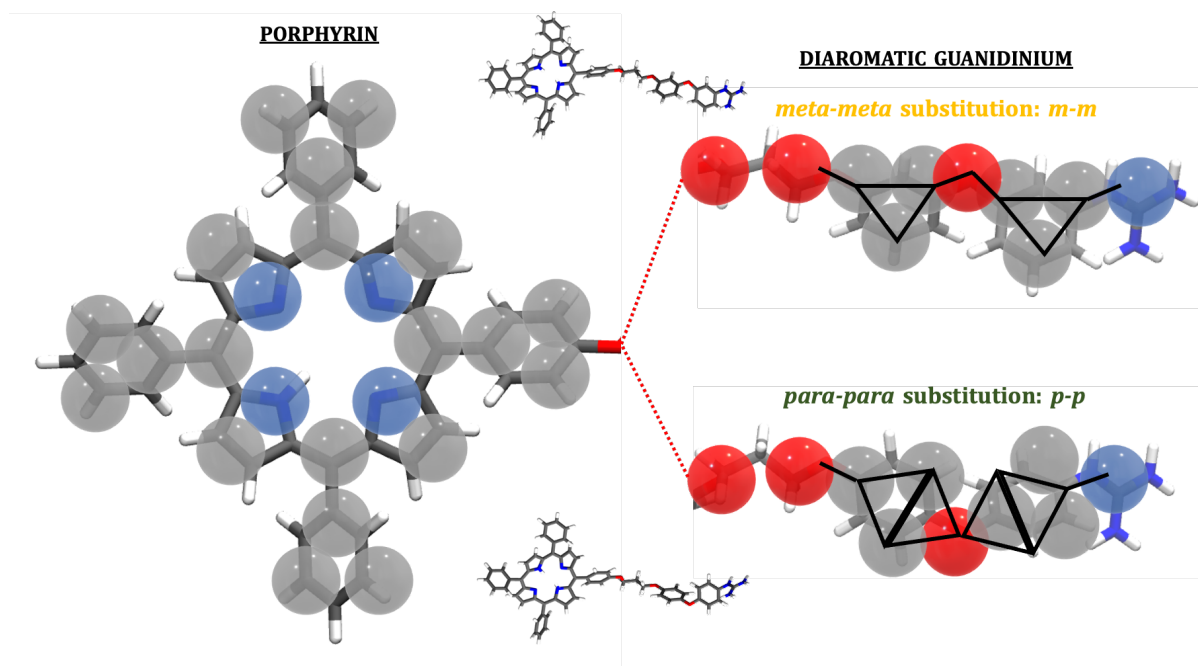
Figure 6.6: CG model for porphyrin diphenyl guanidium conjugates. Black lines represent the bonds set to mimic the *m-m* and *p-p* substitutions. The full atomistic structure for both ligands is shown at the top and the bottom for porphyrin *m-m*- and *p-p*-diphenyl guanidinium conjugates, respectively.

To make it clearly, the structures of **Figure 6.6** were divided in two pieces: the "head" which represents the porphyrin group (on the left) and the "tail" (on the right) for each conjugate (*m-m* (top) and *p-p* (bottom)). To keep the tail substitution, we defined the bonds depicted in black lines. A detailed information about the CG is listed below:

- Starting with the "head". Porphyrin was composed by 24 beads. We mapped each benzene to three CG beads and each pyrrole with 2 CG beads. This approach helped mitigate the steric effects that could arise from closely packed nature of these groups within the porphyrin. In addition, four CG beads were introduced to serve as connectors between the benzene groups and the pyrrole groups. Thus, to preserve the overall central core of the porphyrin.

- Considering the "tail", either *m-m* or *p-p* substitutions were composed by 10 CG beads. In this case, benzene groups were also mapped to three CG beads while O-contain groups were mapped to one CG bead. It is important to mention that the -O- bridge between the diphenyl moiety was chosen to be represented as an individual CG bead to depict the appropriate substitutions in the structure. Finally, the terminal guanidium group was represented by one CG bead. In this case, we were inspired in the terminal group of arginine[21].

When it comes to the bounds for "tail" substitutions, their specific arrangement varies depending on the type of substitution. In the case of *m-m* substitution, the bonds were straightforwardly derived from the atomistic structure itself. On the contrary, the *p-p* substitution posed a greater challenge, as it necessitated a more intricate definition of the bond connections in order to maintain the desired conformation. As shown in **Figure 6.**5, additional bonds were added to retain its intended arrangement and properties. This highlights the nuanced and careful considerations required when establishing the bonding pattern used for different substitutions within a molecule. Although CG mapping involves simplifications, fixing the proper bonds helps maintain the essential structural features of the ligands.

As our simulations were conducted in an aqueous environment, the essential features to consider the CG applied for solvent molecules and counterions within the system are explained in the following section.

6.2.3. CG Model for solvent and counterions

In a cellular environment, G4s are often present within the context of water and ions, which play vital roles in stabilizing the structure and modulating its function. By including solvate and ions in Martini simulations, we are mimicking their dynamics in a biological medium. This is especially important as water provides structural support and can participate in hydrogen bonding with the compounds of the system, while ions can electrostatically interact with charged residues, affecting their stability.

For Martini, one CG bead of water (W) represents four water molecules. Despite the huge success of the model, certain problems have emerged, such as the occurrence of water freezing. This issue arises due to the nature of CG representations, where the interaction potentials tend to be softer compared to the 12-6 functions for the non-bonded potentials in Martini. To address this, shifted and truncated potentials are utilized reducing the long-range attractive part. Consequently, water beads are more fluid compared to the standard LJ potential. To mitigate freezing, a practical solution involves replacing 10% of the water beads with antifreeze waters (WF)[22]. These WF beads disrupt the lattice packing of water, thereby preventing freezing, and ensuring the smooth progression simulations (**Figure 6.7**).
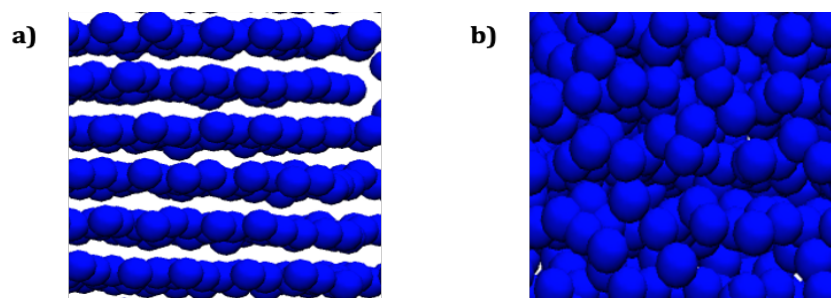
Figure 6.7: Screenshots from Martini water box after MD run: **a)** in the absence of WF beads and **b)** with the presence of WF beads.

However, it is important to mention that a more recent version of Martini have introduced a new polarizable water bead[23], consisting of a central particle interacting via LJ potential, and two additional oppositely charged beads which give the model orientational polarizability; this model have improved many of the properties of Martini water, including the poor representation of the melting point.

On the other hand, considering that G4s are highly charged biomolecules, it is advisable to add at least counter ions in the system. This will ensure that the electrostatic and solvation effects are properly captured, leading to more realistic and reliable results. Furthermore, the addition of ions can influence the condensation of counter ions in DNA affecting the compaction and the overall structure of DNA to represent this phenomenon. According to Marrink *et al*[22], ions are represented using a simplified approach that aims to capture their essential electrostatic interactions while reducing computational complexity. In Martini, ions are typically represented by a single CG bead with a net charge that reflects their overall charge in the system. The charge value assigned to the ion bead is determined based on the ion's formal charge. In the present chapter, we used sodium ions (Na^+) and chloride ions (Cl^-) as a single positive and negative charged CG bead, respectively.

6.3. Martini simulations for G4

This section comprises MD simulations of isolated **c-kit2**. To assess the structural stability and the conformational dynamics of G4 over the simulation, the Root Mean Square Deviation (RMSD) and the Root Mean Square Fluctuation (RMSF) for the bases and the G4 backbone were calculated (**Figure 6.8**).
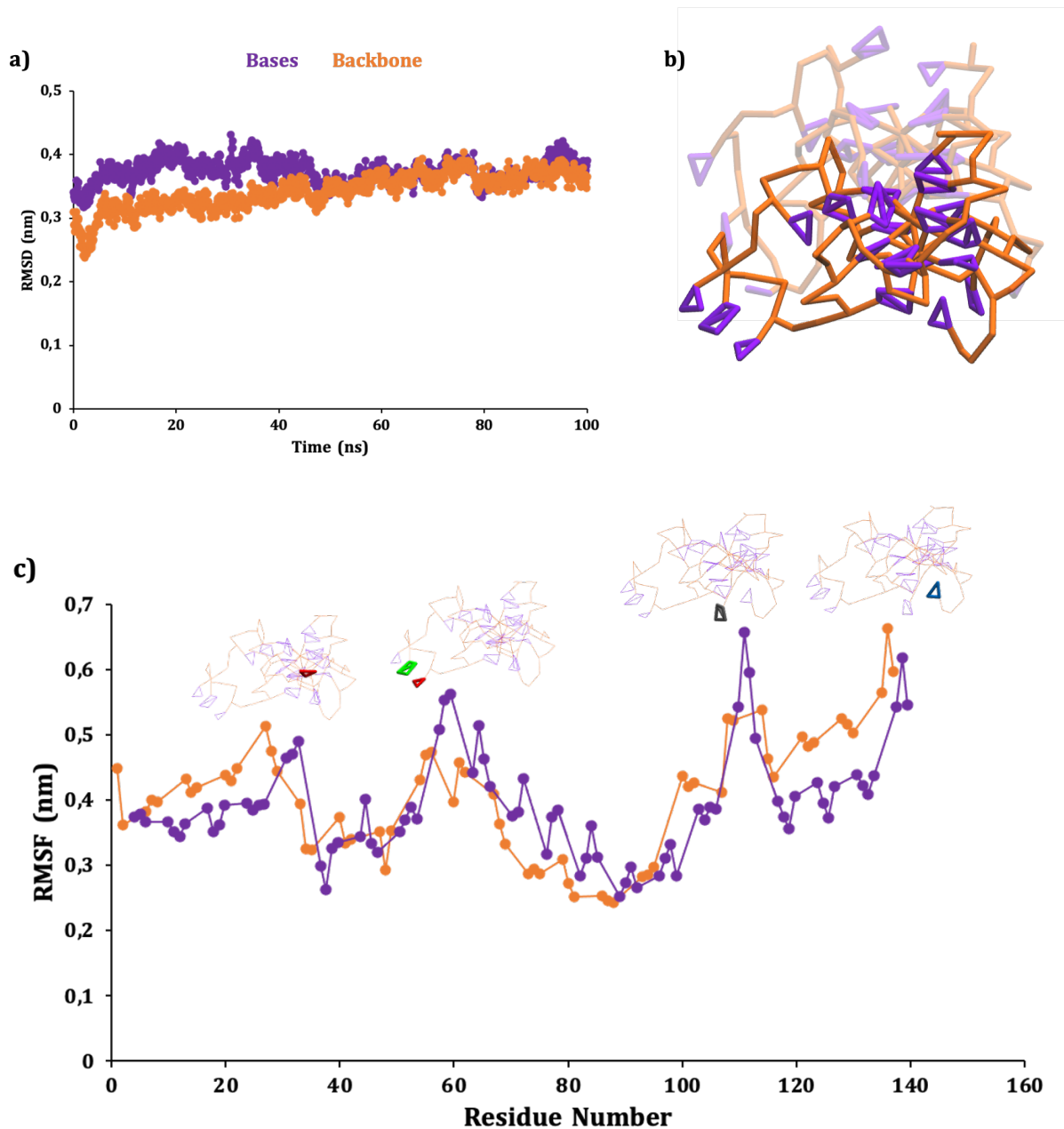
Figure 6.8: Time dependence of RMSDs (**a**) and RMSF (**b**) for the **bases** (purple) and **backbone** (orange) in G4. **c**) Initial (transparent) and final structure for the G4.

The RMSD plot from **Figure 6.8** illustrates that at the beginning of the simulation the RMSD values for the bases are higher than for the backbone until around 60 ns. This could indicate that the bases experienced more pronounced fluctuations or structural rearrangements attributed to their inherent flexibility. As the simulation progresses, the RMSD values become similar for both until 100 ns indicating that both the bases and the backbone have settled into a dynamic equilibrium.

We examined the RMSF (**Figure 6.8.c**) to better analyze the distortion of G4 individual CG beads. The bases often show higher degrees of variation than the backbone indicating that they are more adaptable to structural changes within the G4. Notably, there are four areas with increased peak values which are associated with the bases that do not participate in the formation of G-tetrads. **Table 6.2** compiles the RMSF values for the bases belonging to these specific areas.

Table 6.2: RMSF values for the **bases** that corresponds to each region.

Region	Bases	Bead Index	RMSF (nm)
1st peak	Cytosine	30	0,477
		31	0,484
		32	0,507
2nd peak	Cytosine	57	0,527
		58	0,576
		59	0,585
	Guanine	63	0,452
		64	0,533
		65	0,476
		66	0,429
3rd peak	Adenine	110	0,565
		111	0,692
		112	0,624
		113	0,511
4th peak	Thymine	138	0,565
		139	0,648
		140	0,568

It is important to mention that the guanine that corresponds to the 2nd peak does not participate in the formation of G-tetrads (highlighted in green in **Figure 6.7**). This observation aligns with the expected behavior, where bases involved in the G-tetrads formation exhibit lower fluctuation due to their participation in stable hydrogen bonding. Overall, these findings shed light on the dynamic behavior of G4 highlighting the critical role of specific bases and their contributions to the stability and flexibility of G4s.

Afterwards, we measured the compactness of the G4 structure by the radius of gyration (Rg) at each time point of the trajectory (**Figure 6.9**).
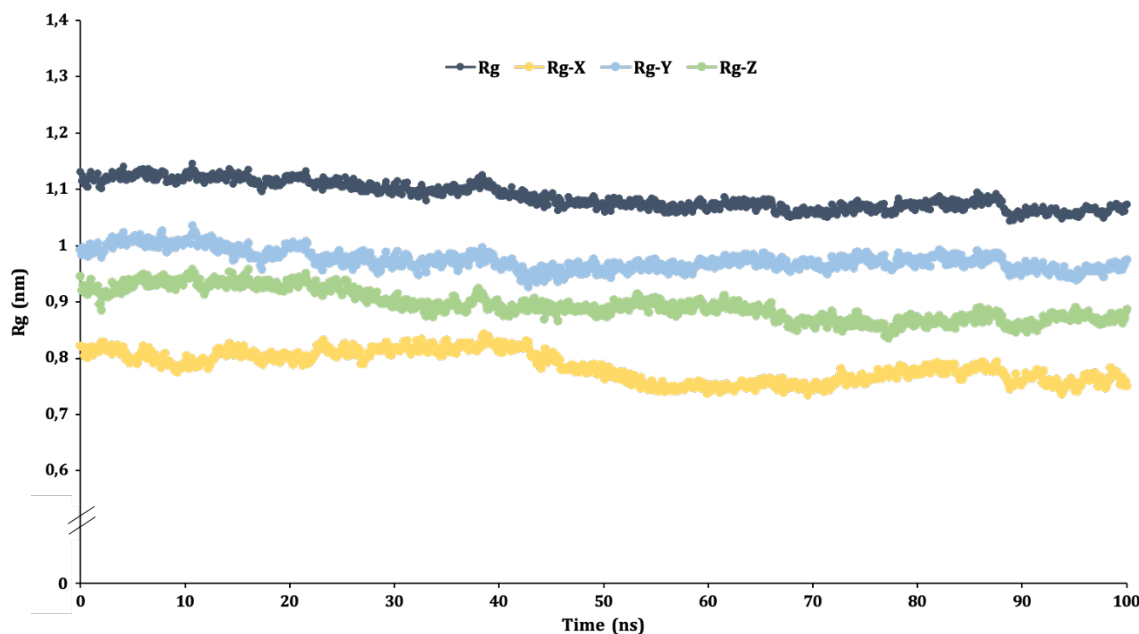

Figure 6.9: Rg as a function of simulation time (in stone blue). The Rg within X (Rg-X), Y (Rg-Y) and Z (Rg-Z) axes are depicted in yellow, light blue and light green, respectively.

The Rg values fall over time, as seen in **Figure 6.9**, with a significant point decline occurring at 90 ns. This suggests that G4 is becoming more compact as the simulation goes on. This could be due to the various factors, such as the system adopting a more energetically favorable conformation, or perhaps responding to its interactions with the environment. The fact that the Rg values are higher than the individual Rg-X, Rg-Y and Rg-Z values is expected since the overall Rg is calculated from all three dimensions (X, Y and Z), so it generally tends to be larger. On the other hand, Rg-Y present higher values than Rg-Z and Rg-X indicating that G4 is not symmetric, and its spreads is anisotropic.

In a way, both RMSD and Rg provide complementary insights into the dynamics' behavior of G4 in terms of its structural stability and conformational changes. While the RMSD focuses on deviation from a reference state, Rg is more about changes in the size and shape of the G4 itself. Concurrently, the RMSF data indicates the residue numbers of the CG beads that exhibit higher fluctuations.

Finally we analyzed the interactions between the G4 and its surrounding solvent. To do so, we firstly calculated the RDF values from the *c.o.m.* of the G4 to the other G4 beads to know the extension of the G4. Simultaneously, we also measured the probability to find water beads from the *c.o.m.* of the G4 at different distances (g(r)) (**Figure 6.10**).
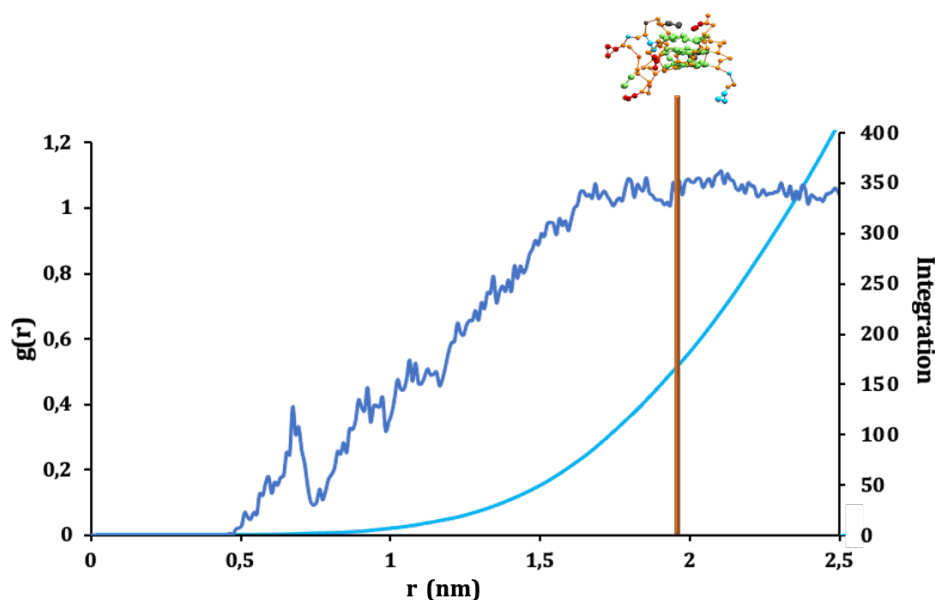

Figure 6.10: Graphic of g(r) (dark blue) and integration (light blue) for W beads respect to the G4 *c.o.m.* at different distances. The orange line depicts the distance from the G4 *c.o.m.* to its outer rim.

Figure 6.10 gives us information about the spatial arrangement of W beads from the *c.o.m.* of the G4. As one can see, the g(r) values for W increases as the distance from the G4 *c.o.m.* increases, suggesting that the probability of finding W beads until 1.6 nm is lower than 1. Notably, at distance of 1.6 nm, the probability reaches unity suggesting a strong likelihood of locating W beads at this specific distance. However, this does not directly determine wheter the W beads are inside or outside the G4.

Although the largest distance to the *c.o.m.* of the G4 is located at 1.9 nm, it is crucial to note that the anisotropic nature of the G4 introduces directional variations in its properties. Therefore, an increasing probability of W beads from 0 to 1.9 nm does not imply their presence inside the G4. Additional investigation is required to pinpoint the position of W beads in relation to the G4. To determine if the W beads were positioned close to the G4, we secondly looked at the density distribution along the box for both the W beads and the G4 (**Figure 6.11**).
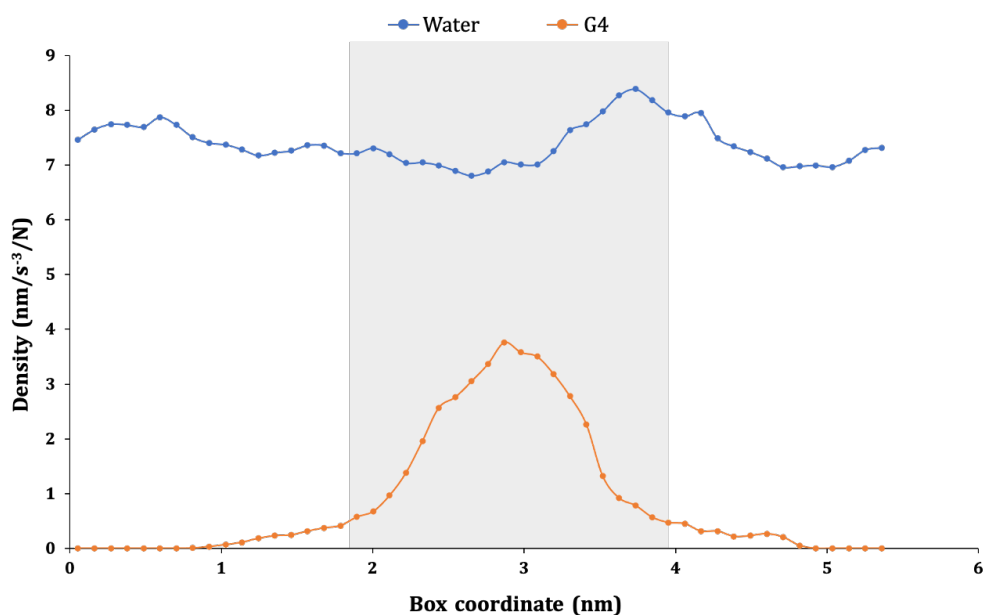
Figure 6.11: Density distribution for the W beads (in blue) and the G4 (in orange) along the box.

The density number provides us valuable insights into the distribution and packing of the G4 as well as the W beads within the simulation box. Addressing to the results of **Figure 6.11**, we can see that:

- The density values for W beads are higher than for G4. This is explained by the greater proportion of W beads compared to G4.

- While the overall density of the G4 is centered within the middle of the box, W beads are distributed evenly throughout the entire volume. Consequently, the G4 exhibits a prominent density peak, indicating a localized concentration in the middle of the box.

- Conversely, in the case of W, although its distribution is more uniform, it is noticeable that there is a distinct intensity peak (from 3.2 to 4.2 nm) observed in proximity to G4 side implying that there are more W beads in that region.

It is also important to mention that, even though this analysis provided valuable insights into the structural dynamics of the G4 and its behavior in the solvent environment, additional properties such the hydrogen bonding patters, or the influence of temperature or pH could be further explored. However, these findings are necessary to a more comprehensive understanding of the G4 biology.

6.5. MD for G4-ligands

It is clear that these ligands with a planar aromatic core and cationic terminal guanidinium not only provide π-π stacking interactions with the aromatic surface of G-tetrads, but also the side chain can interact with the phosphate groups of G4 loops. To understand the nature of the interactions between both ligands with the G4, the MD simulation results were analyzed as follows:

1) Ligands were positioned individually around the G4 molecule in various orientations, including top (**T**), bottom (**B**), left (**L**) and right (**R**) sides, while also altering the position of the chain, mimicking a docking scenario. A total of 8 simulations were performed for each ligand.

2) The RDF between the G4 *c.o.m.* with both the guanidinium and the porphyrin bead were conducted (**Figure 6.12**). This analysis provides insights into the proximity of the ligands to G4, allowing us to understand their spatial relationship.

To facilitate comprehension and ease of tracking of the results, we defined the following nomenclature: "*ligandsusbtitution-ligandposition-guanidiniumorientation*".

- *Ligandsubstitution:* whether if the ligand used for those simulations was the *m-m* substituted (*mm*) or the *p-p* (*pp*).

- *Ligandposition:* the nomenclature utilizes specific letters to represent different orientations, relative to the G4: "**T**" signifies that the ligand is positioned above the G4 (**top**), "**B**" denotes below the G4 (**bottom**), "**L**" represents to the **left** side, and "**R**" to the **right**.

- *Guanidiniumorientation:* this indicates whether the guanidium group is oriented to the **left, right, up** or **down**.

It should be noted that the peaks labeled with letters in **Figure 6.12** correspond to the jobs specified in the figure's legend.
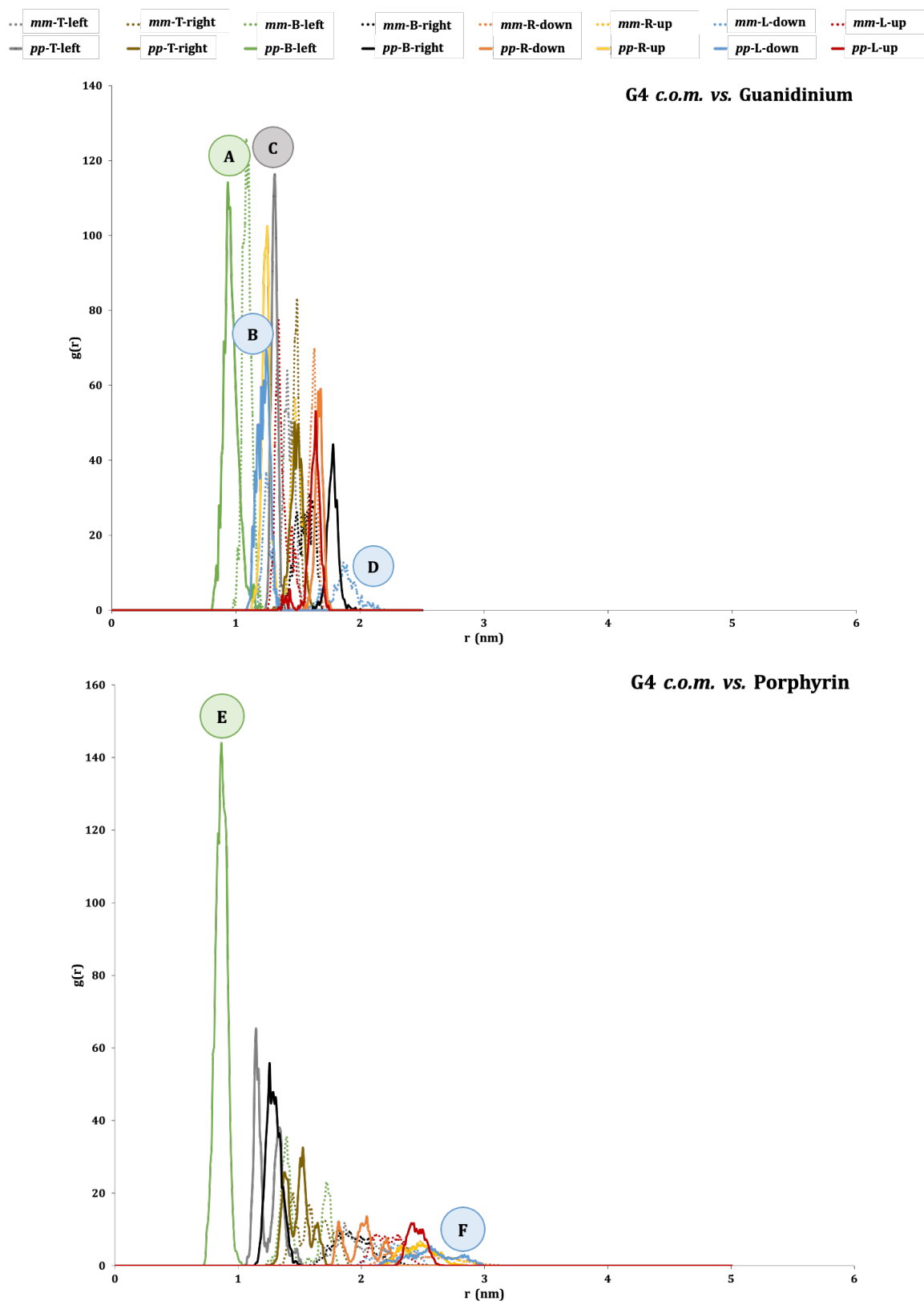
Figure 6.12: g(r) from the *c.o.m.* of the G4 to the guanidinium group of the ligands (top) and the porphyrin group (bottom). Dashed lines represent the resultant values for *m-m* conjugates.

The analysis of the RDF from **Figure 6.12** provides us information about the nature of the interactions between the G4 *c.o.m.* with either the guanidinium (in the top) or the porphyrin (in the bottom) groups for the ligands. Broadly speaking, the distances between the G4 *c.o.m.* with the porphyrin are bigger than for the guanidinium due to the bulky nature of the porphyrin. Moreover, the positive charge of guanidinium group can also a play role in the formation of electrostatic interactions between the negatively charge residues of the G4.

The distinct peak shapes and their weights offer insights into the strength, and heterogeneity of the interactions at different distances. Thus, we focused on studying the differences between them:

- **Peaks A and E** indicate that both the guanidinium and the porphyrin groups of *pp*-**B-left** are near the G4 suggesting an attraction between both entities.

- **Peak B** corresponds to the *pp*-**L-down**. The broader nature of this peak with the presence of small peaks implies a relatively weaker interaction between the G4 and the guanidinium. It suggests that there may be multiple conformations contributing to this interaction, thus, resulting in a less-defined peak shape.

- **Peak C** is the narrowest and most well-defined peak. It suggests a specific and well-defined interaction between the G4 and the guanidinium group. Although the *pp*-**T-left** is at greater distance from the G4 *c.o.m.,* their interaction with the G4 is stable.

- **Peaks D and F** indicate the presence of more distorted and broader forms, suggesting that both the *mm*-**L-down** and the *pp*-**L-down** conformations experience fluctuations, resulting in weaker interactions with the G4.

Furthermore, it is worth noting that in case of *p-p* ligand, when the porphyrin is oriented in parallel with the G-tetrads, it displays closeness to the G4, which may reproduce the presence of π-stacking interactions as seen in the following snapshot (**Figure 6.13**). On the other hand, the guanidium bead tends towards the phosphate-sugar backbone, seeking electrostatic stabilization. Such dual behavior emphasizes the intricate relationship between structural orientation and molecular interactions between the G4 and these ligands.
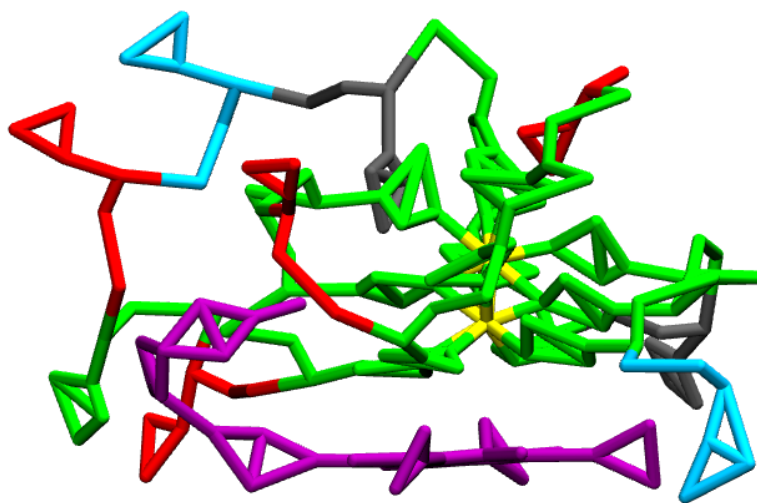
Figure 6.13: MD snapshot for *pp*-**B-left**. Ligand depicted in light purple. W, WF and counterions are removed for sake of clarity.

6.4. Conclusions

We found that the bases within the G4 present more distortion than the backbone. Further to this, the bases outside the G-tetrad region present higher degrees of deviation, indicating that they are more flexible and prone to fluctuations. Furthermore, the decreasing trend in Rg values suggested that G4 structure is compacting throughout the simulation.

The analysis of the interactions between G4 and the ligands indicate: a) that *pp*-**B-left** is wrapping the G4; b) *mm*-**L-down** and *pp*-**L-down** present a wider range of conformations implying a less stable binding; c) the guanidinium of *pp*-**T-left** presents stable interactions with the G4 as deduce from the well-defined peak in the RDF.

In conclusion, this study provides insights into the conformational changes, structural stability, solvent interactions, and ligand interactions with G4. It is important to emphasize that there is still significant research to be conducted; however, due to time limitations, we were unable to address all the aspects thoroughly.

6.5. Highlights of this chapter

The important highlights of this chapter are listed below:

- Presented CG models for G4 and two diaromatic guanidium-porphyrin conjugates.

- Studied the conformational dynamics and the structural stability of G4.

- Studied the interactions between **m-m** and **p-p** substituted ligands with the G4.

6.6. References

(1)   Williamson, J. R.; Raghuraman, M. K.; Cech, T. R. Monovalent Cation-Induced Structure of Telomeric DNA: The G-Quartet Model. *Cell.* **1989**, *59* (5), 871–880.

(2)   Kuryavyi, V.; Phan, A. T.; Patel, D. J. Solution Structures of All Parallel-Stranded Monomeric and Dimeric G-Quadruplex Scaffolds of the Human c-Kit2 Promoter. *Nucleic Acids Res.* **2010**, *38* (19), 6757–6773.

(3)   Hoogsteen, K. The Crystal and Molecular Structure of a Hydrogen-Bonded Complex between 1-Methylthymine and 9-Methyladenine. *Acta Crystallogr.* **1963**, *16* (9), 907–916.

(4)   Haider, S. M.; Parkinson, G. N.; Neidle, S. Structure of a G-Quadruplex–Ligand Complex. *J. Mol. Biol.* **2003**, *326* (1), 117–125.

(5)   Lagnado, J. The Story of Quadruplex DNA. *Biochem.* **2013**, *35* (2), 44–46.

(6)   Gellert, M.; Lipsett, M. N.; Davies, D. R. Helix formation by guanylic acid. *Proc. Nat. Acad. Sci.* **1962**, *48* (12), 2013–2018.

(7)   Sen, D.; Gilbert, W. Formation of Parallel Four-Stranded Complexes by Guanine-Rich Motifs in DNA and Its Implications for Meiosis. *Nature* **1988**, *334* (6180), 364–366.

(8)   Sundquist, W. I.; Klug, A. Telomeric DNA Dimerizes by Formation of Guanine Tetrads between Hairpin Loops. *Nature* **1989**, *342* (6251), 825–829.

(9)   Wei, D.; Husby, J.; Neidle, S. Flexibility and Structural Conservation in a C-KIT G-Quadruplex. *Nucleic Acids Res.* **2015**, *43* (1), 629–644.

(10)   Takahashi, S.; Sugimoto, N. Watson–Crick versus Hoogsteen Base Pairs: Chemical Strategy to Encode and Express Genetic Information in Life. *Acc. Chem. Res.* **2021**, *54* (9), 2110–2120.

(11)   Petersen, M. Nucleic Acids Studied by NMR Spectroscopy. In *Encyclopedia of Spectroscopy and Spectrometry*; Lindon, J.; Tranter, G. E.; Koppenaal, D., Eds; Elsevier, 2017; 463–472.

(12)   Chalikian, T. V.; Liu, L.; Macgregor, Jr. , R. B. Duplex-Tetraplex Equilibria in Guanine- and Cytosine-Rich DNA. *Biophys. Chem.* **2020**, *267*, 106473.

(13) Day, H. A.; Pavlou, P.; Waller, Z. A. E. I-Motif DNA: Structure, Stability and Targeting with Ligands. *Bioorg. Med. Chem.* **2014**, *22* (16), 4407–4418.

(14) Salsbury, A. M.; Dean, T. J.; Lemkul, J. A. Polarizable Molecular Dynamics Simulations of Two *c-Kit* Oncogene Promoter G-Quadruplexes: Effect of Primary and Secondary Structure on Loop and Ion Sampling. *J. Chem. Theory Comput.* **2020**, *16* (5), 3430–3444.

(15) Hsu, S.-T. D.; Varnai, P.; Bugaut, A.; Reszka, A. P.; Neidle, S.; Balasubramanian, S. A G-Rich Sequence within the *c-Kit* Oncogene Promoter Forms a Parallel G-Quadruplex Having Asymmetric G-Tetrad Dynamics. *J. Am. Chem. Soc.* **2009**, *131* (37), 13399–13409.

(16) Peterková, K.; Durník, I.; Marek, R.; Plavec, J.; Podbevšek, P. C-Kit2 G-Quadruplex Stabilized via a Covalent Probe: Exploring G-Quartet Asymmetry. *Nucleic Acids Res.* **2021**, *49* (15), 8947–8960.

(17) Uusitalo, J. J.; Ingólfsson, H. I.; Akhshi, P.; Tieleman, D. P.; Marrink, S. J. Martini Coarse-Grained Force Field: Extension to DNA. *J. Chem. Theory. Comput.* **2015**, *11* (8), 3932–3945.

(18) Jin, J.; Pak, A. J.; Durumeric, A. E. P.; Loose, T. D.; Voth, G. A. Bottom-up Coarse-Graining: Principles and Perspectives. *J. Chem. Theory. Comput.* **2022**, *18* (10), 5759–5791.

(19) Frisch, M. J.; et al. Gaussian 16, Revision C.01. Gaussian Inc 2016.

(20) Stipaničev, N.; Raabe, K.; Rozas, I. Aiming to Improve Binding of Porphyrin Diphenyl Guanidinium Conjugates to Guanine-Quadruplexes: When Size Matters. *Bioorg. Med. Chem Lett* **2022**, *75*, 128954.

(21) Periole, X.; Marrink, S.-J. The Martini Coarse-Grained Force Field; Monticelli, L.; Salonen, E., Eds; Humana Press: Totowa, 2013, 533–565.

(22) Marrink, S. J.; Risselada, H. J.; Yefimov, S.; Tieleman, D. P.; de Vries, A. H. The MARTINI Force Field: Coarse Grained Model for Biomolecular Simulations. *J. Phys. Chem. B* **2007**, *111* (27), 7812–7824.

(23) Yesylevskyy, S. O.; Schäfer, L. V.; Sengupta, D.; Marrink, S. J. Polarizable Water Model for the Coarse-Grained MARTINI Force Field. *PLoS Comput. Biol.* **2010**, *6* (6), e1000810.

"The road to success is always
under construction."
Lily Tomlin

Chapter 7

Conclusions and outlook

This Chapter presents a summary of contributions that have been accomplish in this thesis and a note on the future direction of research in this field.

7.1. General conclusions

In this PhD thesis, we have employed CG models via DPD and Martini force field, with the aim of getting a detailed insight about complex systems and its interactions with different molecules. Along this research, we have designed specific CG models to study each system, as well as to derive the proper SRP values between CG beads.

Having presented the results of all the work, we are able to give the best responses to the objectives set out in **Chapter 1**.

- <u>CONCLUSION 1</u>: we have successfully implemented a novel derivation of SRP matrix, that correlates SRP values from our program with the $\Delta E_{binding}$ obtained from QM calculations. Moreover, a purely hydrocarbon chain was used in our investigations, a pioneering approach as there are no reviews for that surfactant. The results from our studies align well with existing experimental studies, such as the CTAB-Gold nanorod mechanisms of growth, thereby validating our approach.

- <u>CONCLUSION 2</u>: we have used three different approaches to determine the SRP values and none of them revealed spherical Janus distributions with the real IgG. However, upon modification of the F$_{ab}$ regions of both IgG, it appeared that IgG produced patches, approaching Janus distribution patterns. This suggests that altering the F$_{ab}$ regions could potentially impact the spatial distribution of IgG.

- <u>CONCLUSION 3</u>: we have successfully designed a CG model for both G4 and ligands using the Martini force field. Preliminary observations suggest that the *para-para* substituted ligand (diaromatic porphyrin conjugate) interacts more favorably with the G4 compared to the *meta-meta* substituted ligand. However, a more comprehensive study is required to validate these initial findings, but we are currently constrained by time.

Overall, the results presented in this thesis highlights the substantial effect of mapping schemes on CG, and how they influence simulation outcomes and bead interactions. The list of applications of the CG methodology presented in this thesis is far from being exhaustive but gives a flavor of the great potential of the approach.

7.2. Perspectives and ongoing work

The insights gained from this study can potentially guide for future research and development in various topics:

1) The methodology used for determining the SRP values for Au beads can be applied to other systems involving metals. For instance, in the study of silver nanoparticles (Ag NPs), which could broaden our understanding of the behavior and properties of these particles.

2) Our study on the obtention of spherical Janus distribution onto Au NPs surface prompts us to contemplate that there are other ways in which AAs can be classified, which could alter SRP values. On the other hand, a comparative study of using different immunoglobulins such as IgG and IgE is another perspective that can be considered. Their AAs diversity could potentially affect on their distribution onto Au NPs surface.

3) For the interactions between G4 and ligands, there exist numerous ligands that can be used. However, a challenge for future work is to ensure that the CG applied maintains the original conformation of these ligands. Further research will help in improving the efficiency of our simulations.

In closing, our research presents merely the initial foray into these intricate systems. Thus, further exploration and development is substantial and holds great promise.

"Life is not a plot;

It's in the details."

Jodi Picoult

Chapter 8:

Simulation details

This chapter summarizes the computational details to carried out the whole simulations including the simulation setup, the quantity of compounds used and the duration of the simulation period.

8.1. Simulation Flowchart

The process employed to generate our CG simulations is outline in **Figure 8.1**.
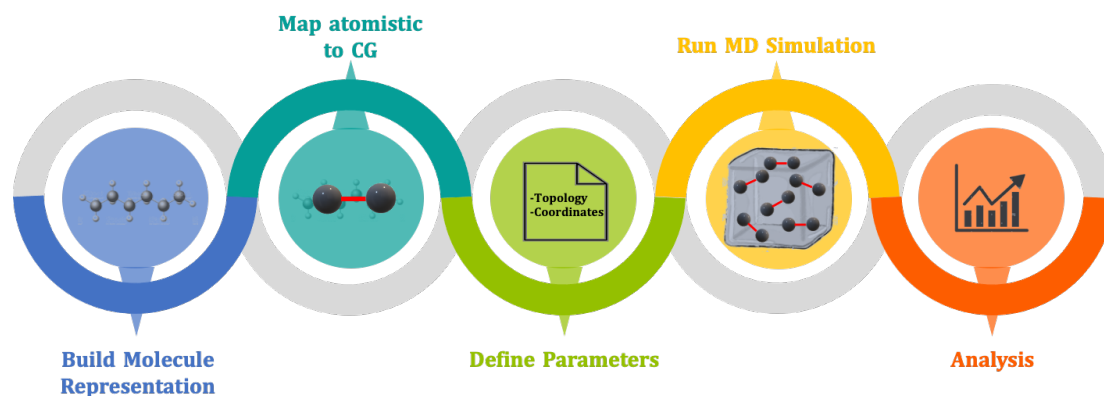

Figure 8.1: Steps followed to create a CG simulation.

The main steps are:

1) To construct an atomistic representation of the molecule which specifies the arrangement, connectivity, and composition of atoms in the molecule.

2) To select an atom-to-bead mapping. This is the heart of CG processes since it requires expertise, chemical knowledge, and a degree of trial-and-error. The goal is to capture the essential features and interactions of the molecule while reducing the computational complexity.

3) To establish the simulation parameters. This involves two main aspects. First, to describe the CG representation of the molecule, which includes specifying bead types, masses, charges, and connectivity patterns for both bonded and non-bonded interactions. Second, to define the parameters for the MD simulation needed to execute and control the simulation conditions such as, the time step, the temperature, and other relevant factors necessary for the accurate execution of the simulation.

4) To execute a computational simulation that models the behavior and dynamics of a molecular system over time. Running a MD simulation involves three main steps: minimization, equilibration, and production of MD.

5) To compare and analyze the obtained results with experimental data, seeking agreement or discrepancies that provide insight into the system under investigation.

8.2. DPD set up

Simulations for **Chapters 3, 4** and **5** were conducted using a DPD-MC hybrid algorithm. The number of particles (N), the pressure (P) and the temperature (T) were kept constant (*NPT* ensemble). The systems consisted of a cubic box with PBC invoked.

As said in **Chapter 2**, all parameters were given with a single unit scale. λ and σ from eq. 2.3 and 2.4 (**section 2.2**) were set to $0.65d_0$ and $3.0d_0$, respectively. The time step used to integrate the equations of motion was Δt = 0.03 and the temperature was set to 0.42. According to Groot and Rabone[1] it was assumed that the reduced mass and length of one bead is 1. To relate them with a physical mass (eq. 2.7) and length (eq. 2.8), we used the CG model for water. If N_m=3 and m_{H_2O}=18, then m =54. On the other hand, a unit volume r_c^3 holds an average of three beads, and therefore approximately nine water molecules. If the volume of the water molecule was taken to be approximately 30Å^3, then r_c=6.46Å.

8.2.1. Simulation details for Chapter 3

According to Venturoli *et al.*[2] the parameters for elastic contribution to **Eq. 2.17** have the values r_{eq}=1.0 and K_r=100.0 for the surfactants, and the parameters for the bending-force (**Eq. 2.18**) are K_θ=6.0 and θ_{eq}=109° for the angle formed between **Cit.** beads, K_θ=3.0 and θ_{eq}=180° for the angle formed by consecutive bonds in the lineal chains and K_θ=10.0 and θ_{eq}=180° for the bead representing the double bond of **Ole**. The units of K_r and K_θ are $\in_0/r_c^2$ and $\in_0/rad^2$ respectively, where $\in_0$ was the reduced energy unit.

All compounds were randomly distributed in a cubic box of $30\text{x}30\text{x}30d_3^0$ composed by 80000 **W** beads. The main differences between the nucleation and the growth steps were related to **Au**/Surfactant molar ratios and the simulation time. The specific conditions for each step are found in the following sections.

8.2.1.1 Nucleation Step

The total number of Au beads depend on Au/Surfactant molar ratios (**Table 8.1**).

Table 8.1: Number of Au beads and Surfactant molecules depending on the Au/Surfactant ratios.

Au/Surfactant Molar ratios	Au beads	Surfactant molecules
0.5	250	500
1	500	500
2	1000	500

Since the nucleation occurs at the first stage of the synthesis of Au NPs, simulations were run for 82 ps.

8.2.1.2 Growth Step

The number of Au beads and surfactant molecules for each synthesis are collected in the following table (**Table 8.2**).

Table 8.2: Number of Au beads and Surfactant molecules depending on the Surfactant/Au ratios.

Synthesis	Surfactant/Au Molar ratios	Surfactant molecules	Au beads
Turkevich-Frens*[3]	0.60	300	500
	1.60	800	500
	2.70	1350	500
Yonezawa & Kunitake[4]	0.10	50	500
	0.50	250	500
	1.30	650	500
	2.50	1250	500
Aslam *et al.*[5]	0.02	10	500
	0.10	50	500
	0.50	250	500
	1.00	500	500
	2.00	1000	500

*Note that the molar ratios for Turkevich-Frens synthesis were taken from Dr. Marc Padilla PhD thesis. However, to further support the findings, we also added an intermediary molar ratio (Surfactant/Au=1.6). In this case, simulations were run for 25 ns.

8.2.1.3 Experimental Section

The experimental synthesis was performed by Prof. Víctor Puntes and co-workers at ICN2.

8.2.1.3.1 Reagents

All reagents were purchased from Sigma-Aldrich and used as received. All solutions were prepared in Milli-Q water.

- Tetrachloroauric(III) acid trihydrate ($HauCl_4 \cdot 3H_2O$, 99.9%).

- Sodium citrate dihydrate ($HOC(COONa)(CH_2COONa)_2 \cdot 2H_2O$, $\geq$ 99%).

- Cerium (III) nitrate hexahydrate ($Ce(NO_3)_3 \cdot 6H_2O$, 99%).

- Sodium hydroxide ($NaOH$, $\geq$ 99%).

- 11-Mercaptoundecanoic acid (MUA, $HS(CH_2)_{10}CO_2H$, 98%).

8.2.1.3.2 Synthesis of Au@CeO$_2$ NPs

Citrate-stabilized Au NCs of 50 nm in diameter were synthesized from gold chloride and sodium citrate according to methods previously developed by Prof. Víctor Puntes group[6]. The Au NCs were further functionalized with MUA and used without further purification as seeds for the CeO$_2$ coating following a well-defined protocol developed by them. Ligand exchange was performed by adding known amounts of MUA molecules to Au NPs solutions under vigorous stirring. In detail, the ratio of MUA molecules to Au surface atoms was varied from 0, 25, 100 and 5000 which corresponds to the addition of 0, 0.025 mL, 0.25 mL, 2.5 mL, and 25 ml of MUA 1 mM to a volume of 12.5 ml Au NPs. The Au surface was calculated according to the size (50 nm) and concentration of Au NPs (6.04 10^{10} NP/mL, which corresponds to 7.6 10^{14} nm^2/mL). The mixture was allowed to react for 12 h, when no further peak evolution was detected by UV–vis spectroscopy. MUA-functionalized Au NCs were purified and further used as a seeds for the growth of a CeO2 shell following a synthetic approach previously developed by their group[7].

8.2.1.3.3 Characterization techniques

Microscope analyses were carried out on an FEI Magellan 400L XHR SEM operating at 20 kV. Samples were centrifuged and dispersed in water previous to their deposition (10 µL) on an ultrathin formvar-coated 200-mesh copper grid (Ted-pella, Inc.). Average size and size distribution of the samples were measured using ImageJ software by counting at least 500 particles.

8.3. Simulation details for Chapter 4 and Chapter 5

The elastic contributions for IgG were set to r_{eq}=1.0 and K_r=100.0 and the bending contributions to K_θ=20.0 and θ_{eq}=104° and θ_{eq}=134°, according to the original structure.

The simulations conducted in **Chapters 4** and **5** utilized a water box measuring 30x30x30d_0^3. The number of Au beads comprising the Au NP varied depending on whether the simple or complex CG approach was applied to the IgG. In the first scenario, a preformed Au NP consisting of 5000 Au beads was positioned at the center of the box, along with a mixture of 750 IgG molecules for each type. Conversely, in the second scenario, the Au NP was formed by 11000 Au beads accompanied by 200 IgG molecules of each type. The final sizes for both NPs were determined by analyzing the RDF values (**Figure 8.2**).
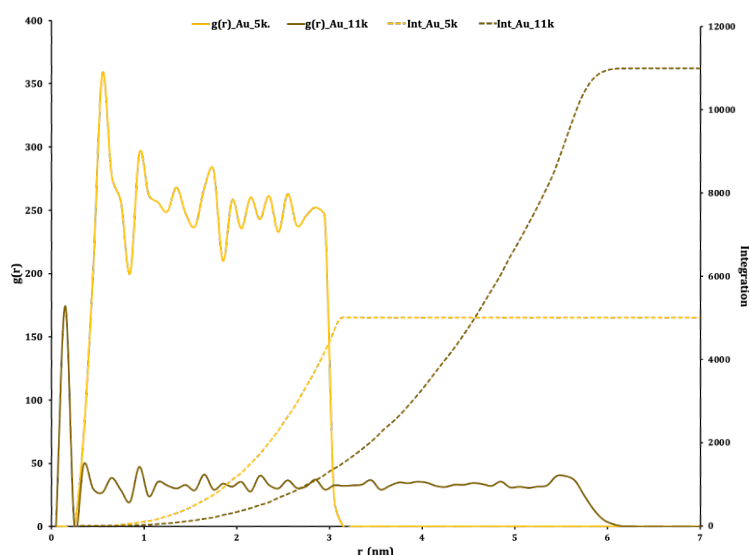

Figure 8.2: g(r) and integration for Au NP of 5000 beads (Au_5k) and 11000 beads (Au_11k).

As one can see in **Figure 8.2**, when the Au NP is composed by 5000 beads, the distance from the *c.o.m.* to the surface beads measures about 3 nm. To deduce the overall diameter, or size, of the Au NP, we simply double this value, resulting in a size of approximately 6 nm. This distance significantly increases when the assembly is comprised of 11000 beads, yielding a distance of approximately 6.25 nm from the *c.o.m.* to the surface, thereby giving an Au NP with a diameter of approximately 12.5 nm. These observations illustrate a direct correlation between the number of beads within the Au NPs and the distance to their *c.o.m.,* implying potential ramifications for the overall structural parameters of the system.

8.4. Martini set up: simulation details for Chapter 6

All simulations were carried out using the GROMACS package[8] with Martini force field[9]. The topologies were built by hand and can be obtained by request. To preserve the G4 conformation, two dummy beads were located manually between G-tetrads, and a network of elastic bonds were established. As mentioned in **Chapter 6**, the ligand topologies were defined according to our specific criteria.

All systems were solvated in a cubic box (50.0 Å × 50.0 Å × 50.0 Å) with about 1300 W and WF beads. PBC were applied in all dimensions. Na^+ counterions were added randomly to neutralize the total charge of the systems. The Particle Mesh Ewald (PME) method was applied to calculate long-range electrostatic interactions[10] and the LINCS algorithm[11] was used to constrain all bonds. A cutoff of 1.0 nm was used for non-bonded van der Waals and electrostatic interactions. The solvated structures were subjected to 50000 steps of energy minimization using the steepest descent algorithm[12]. Then, the minimized structures were equilibrated under two steps: 1) an NVT ensemble (300 K) with a time step of 2 fs for 100 ps, and 2) an NPT ensemble (300K) with a time step of 2 fs for 100 ps. The last step was the MD productions in which the runs were performed in the NPT ensemble for 10 ns at 1 bar and 300 K with a time step of 2 fs. Finally, the results were visualized and analyzed by means of VMD[13] and GROMACS tools[8].

8.5. References

(1)   Groot, R. D.; Rabone, K. L. Mesoscopic Simulation of Cell Membrane Damage, Morphology Change and Rupture by Nonionic Surfactants. *Biophys. J.* **2001**, *81* (2), 725–736.

(2)   Venturoli, M.; Smit, B. Simulating the Self-Assembly of Model Membranes. *Phys. Chem. Comm.* **1999**, *2* (10), 45-49.

(3)   Turkevich, J.; Stevenson, P. C.; Hillier, J. A Study of the Nucleation and Growth Processes in the Synthesis of Colloidal Gold. *Discuss. Faraday Soc.* **1951**, *11*, 55–75.

(4)   Yonezawa, T.; Kunitake, T. Practical Preparation of Anionic Mercapto Ligand-Stabilized Gold Nanoparticles and Their Immobilization. *Colloids Surf. A Physicochem Eng. Asp.* **1999**, *149* (1–3), 193–199.

(5)   Aslam, M.; Fu, L.; Su, M.; Vijayamohanan, K.; Dravid, V. P. Novel One-Step Synthesis of Amine-Stabilized Aqueous Colloidal Gold Nanoparticles. *J. Mater. Chem.* **2004**, *14* (12), 1795-1797.

(6)   Bastús, N. G.; Comenge, J.; Puntes, V. Kinetically Controlled Seeded Growth Synthesis of Citrate-Stabilized Gold Nanoparticles of up to 200 Nm: Size Focusing versus Ostwald Ripening. *Langmuir* **2011**, *27* (17), 11098–11105.

(7)   Piella, J.; Gónzalez-Febles, A.; Patarroyo, J.; Arbiol, J.; Bastús, N. G.; Puntes, V. Seeded-Growth Aqueous Synthesis of Colloidal-Stable Citrate-Stabilized Au/CeO$_2$ Hybrid Nanocrystals: Heterodimers, Core@Shell, and Clover- and Star-Like Structures. *Chem. Mater.* **2019**, *31* (19), 7922–7932.

(8)   Van Der Spoel, D.; Lindahl, E.; Hess, B.; Groenhof, G.; Mark, A. E.; Berendsen, H. J. C. GROMACS: Fast, Flexible, and Free. *J. Comput. Chem.* **2005**, *26* (16), 1701–1718.

(9)   Periole, X.; Marrink, S.-J. The Martini Coarse-Grained Force Field; Monticelli, L.; Salonen, E., Eds; Humana Press: Totowa, 2013, 533–565.

(10)   Darden, T.; York, D.; Pedersen, L. Particle Mesh Ewald: An $N \cdot \log(N)$ Method for Ewald Sums in Large Systems. *J. Chem. Phys.* **1993**, *98* (12), 10089–10092.

(11)   Hess, B.; Bekker, H.; Berendsen, H. J. C.; Fraaije, J. G. E. M. LINCS: A Linear Constraint Solver for Molecular Simulations. *J. Comput. Chem.* **1997**, *18* (12), 1463–1472.

(12)   Haug, E. J.; Arora, J. S.; Matsui, K. A Steepest-Descent Method for Optimization of Mechanical Systems. *J. Optim. Theory Appl.* **1976**, *19* (3), 401–424.

(13)   Humphrey, W.; Dalke, A.; Schulten, K. VMD - Visual Molecular Dynamics. *J. Molec. Graphics* **1996**, *14*, 33–38.

Appendix:

Please, scan the provided QR code to access the associated Appendix:

"If I have seen further than others,

it is by standing upon the shoulders of giants."

Isaac Newton